

Numerical study of the nonequilibrium dynamics of 1-D electron-phonon systems using a local basis optimization

Von der Fakultät für Mathematik und Physik
der Gottfried Wilhelm Leibniz Universität Hannover

zur Erlangung des akademischen Grades
Doktor der Naturwissenschaften
Dr. rer. nat

genehmigte Dissertation von

M. SC. CHRISTOPH BROCKT

Referent: Prof. Dr. Eric Jeckelmann
Korreferent: Priv.-Doz. Dr. Fabian Heidrich-Meisner

Tag der Promotion: 19.01.2018

Abstract

In this dissertation a newly developed numerical method is presented, which is optimized for the time evolution of one-dimensional lattice systems with large local Hilbert spaces. This method extends the *time-evolving block-decimation* (TEBD) to include a local basis optimization (LBO), which has already been successfully combined with ground state methods. The algorithm is based on matrix product states (MPS), which can represent the quantum state of a one-dimensional chain in most cases with a number of parameters, that is not exponentially increasing with the chain length. The LBO causes a reduction of the simulation times that is linear in the bond dimension of the MPS. To demonstrate the advantages of this method, we apply the TEBD-LBO to electron-phonon (e-p) systems. In this thesis these are described by the Holstein model, which goes beyond semi-classical approximations and covers the full quantum statistics of the phonons. The understanding of the nonequilibrium dynamics of charge carriers coupled to lattice vibrations is of great importance for research areas like transport through quasi one-dimensional conductors, photo-generated phase transitions and time-resolved spectroscopy.

First, the energy transfer from a highly excited electron to the phononic degrees of freedom on a small chain is studied. In the various parameter regimes different types of relaxation occur. In any case, after a certain time the system reaches a state, where on average no energy is exchanged between the electron and phonons. This can either mean a constant kinetic energy or oscillations with a constant amplitude and frequency.

Next, long perfectly conducting leads without coupling to phonons were attached on both sides of the small chain. In the left lead an electron with density distribution in the shape of a Gaussian wave packet is injected with momentum towards the e-p coupled structure in the middle. This structure acts as an impurity in an otherwise perfectly conducting chain. The investigation shows resonance effects in the transmission and reflection at this impurity. Further, the electron can transfer a part of its energy permanently to the phonons, which results in a reduction of the velocity. Finally, two mechanisms are presented that lead to self-trapping of the electron on the e-p coupled structure.

Keywords: time-evolving block-decimation, one-dimensional systems, electron-phonon systems, Holstein model, scattering

Zusammenfassung

In dieser Dissertation wird eine neu entwickelte numerische Methode vorgestellt, die für die Zeitentwicklung von eindimensionalen Gittersystemen mit großen lokalen Hilberträumen optimiert wurde. Die *time-evolving block-decimation* (TEBD) wird dabei mit einer lokalen Basisoptimierung (LBO) erweitert, welche bereits erfolgreich für Grundzustandsberechnungen verwendet werden konnte. Der Algorithmus nutzt die Darstellung von Quantenzuständen durch Matrixproduktzustände (MPS), welche eine eindimensionale Kette in den meisten Fällen ohne eine exponentiell mit der Kettenlänge anwachsende Anzahl an Parametern beschreiben können. Durch die LBO skaliert die Laufzeit der Simulationen nun mit einer um eins reduzierten Potenz der Dimension der Matrizen des MPS. Um die Vorteile der Methode zu demonstrieren, wird die TEBD-LBO auf Elektron-Phonon (e-p) Systeme angewendet. Diese werden in der vorliegenden Arbeit durch das Holstein Modell beschrieben, welches über semi-klassische Näherungen hinaus geht und die volle Quantenstatistik der Phononen berücksichtigt. Forschungsgebiete wie der Transport durch quasi-eindimensionale Leiter, Photo-induzierte Phasenübergänge und zeitaufgelöste Spektroskopie würden sehr von einem größeren Verständnis der Nichtgleichgewichtsdynamik von Ladungsträgern, die an Gitterschwingungen gekoppelt sind, profitieren.

Zunächst wurde der Energietransfer von einem hoch angeregten Elektron zu den phononischen Freiheitsgraden auf einer kurzen Kette untersucht. Dabei zeigen sich in den unterschiedlichen Parameterbereichen verschiedene Formen von Relaxation. In jedem Fall wird nach einer gewissen Zeit ein Zustand angenommen, in dem es im Mittel keinen Energieaustausch zwischen Elektron und Phononen mehr gibt. Dies kann sowohl eine konstante kinetische Energie, als auch Oszillationen mit konstanter Amplitude und Frequenz bedeuten.

Als Nächstes wurden jeweils eine lange Zu- und Ableitung, in denen es keine Kopplung an Phononen gibt, an die kurze Holstein-Kette angefügt. In die Zuleitung wird dabei ein Elektron mit Dichteverteilung in Form eines Gaußschen Wellenpackets und Impuls in Richtung der Elektron-Phonon-gekoppelten Struktur in der Mitte eingefügt. Diese wirkt als eine Störstelle in einem ansonsten perfekten Leiter. Die Untersuchung zeigt, dass es Resonanz-Effekte bei der Transmission und Reflexion an dieser Störstelle gibt und dass das Elektron einen Teil seiner kinetischen Energie dauerhaft an die Phononen abgeben kann, was zu einer Reduktion der Geschwindigkeit führt. Außerdem werden zwei verschiedene Mechanismen vorgestellt, die ein Self-Trapping des Elektrons auf der gekoppelten Struktur bewirken.

Schlagerworte: time-evolving block-decimation, eindimensionale Systeme, Elektron-Phonon Systeme, Holstein Modell, Streuung

Contents

1. Introduction	9
1.1. Condensed matter	9
1.2. Numerical methods	10
1.3. Outline	11
2. Time-evolving block-decimation with local basis optimization	13
2.1. Matrix product states	13
2.2. Time-evolving block-decimation	18
2.3. The optimal basis	24
3. Relaxation of a highly excited electron in the Holstein model	29
3.1. Single-site system	31
3.2. Short-time dynamics	33
3.3. Perturbation theory	35
3.4. Relaxation dynamics	38
3.5. Optimal modes	40
4. Scattering of an electronic wave packet by a one-dimensional electron-phonon-coupled structure	43
4.1. Scattering theory	45
4.2. Wave packet averaging	48
4.3. Transmission	49
4.4. Dissipation	55
4.5. Transient self-trapping	61
5. Summary, conclusion and outlook	67
5.1. Physical results	67
5.2. TEBD-LBO performance	69
5.3. Outlook	71
Appendices	73
A. Orthonormalization of the initial state	75
B. Diagonalization of the tight-binding Hamiltonian for open boundary conditions	77
Bibliography	79

1. Introduction

In quantum mechanics a system composed of several particles is more than the mere sum of these. The existence of entanglement between those particles causes the Hilbert space of the composite system to be the product of the individual Hilbert spaces, rather than their sum. While this property is interesting, in the sense that it yields new physics that are not present in classical theories, it can also become an obstacle, especially when considering many particles. Although the complete dynamics of non-dissipative systems are determined by the Schrödinger equation, which can easily be solved for time-independent Hamiltonians, the computational complexity of the arising algebraic problem of applying a matrix exponential to a vector is so high that even modern-day supercomputers can only handle a few dozens of particles. On the other hand, people are nowadays quite confident that in the near future it will be possible to use this entanglement and the consequential exponential increase of the Hilbert space dimension with the number of particles to build a quantum computer that outperforms any classical machine.

1.1. Condensed matter

To get analytical and numerical results for solids, that are composed of many particles, one has to make some assumptions and approximations. In some cases it is justified to neglect one or even two spatial dimensions and just focus on the constrained lower-dimensional system. In fact some effects only emerge in theories that are formulated in one spatial dimension, e.g. the Peierls transition [1], where the interaction of electrons and lattice vibrations can lead to the formation of a charge density wave leading to an insulating phase. This effect has been observed in experiments [2], thereby verifying that the investigated system effectively behaves like a one-dimensional system. Among the most prominent examples of low-dimensional systems is graphene [3, 4], a layer of carbon atoms with an atomic-scale thickness. Systems that are referred to as quasi-one-dimensional are carbon nanotubes, metallic nanowires, molecular junctions and crystals where the electrons can only move in one direction. As the technology of producing such structures with an extent of only a few atomic diameters progresses, the need for theories describing low-dimensional solids increases.

One of the main assumptions made for any conductor, regardless of the dimension, is that only the electrons in the conduction band are mobile, while the ions are bound by inter-atomic forces, which is what constitutes a solid. This is usually modeled by a lattice, where the lattice sites correspond to the ions and the conduction electrons can move from one site to the next. The distance between the sites is called the lattice constant, but the ions are not completely immobile. The inter-atomic forces result from the electromagnetic interaction and build an elastic lattice, where the sites can oscillate around their equilibrium position. These vibrations are also

1. Introduction

quantized and exhibit particle-like behavior. They are called phonons and they can interact with other particles like electrons and photons. In low-dimensional correlated materials the emergence of phonons has a major effect on the nonequilibrium dynamics. Therefore, the investigation of interacting electron-phonon systems is important for the understanding of transport through low-dimensional and molecular junctions [5, 6, 7], time-resolved spectroscopy [8, 9] and also for relaxation dynamics of photoinduced charge carriers [10, 11, 12].

In this thesis we study the Holstein model with one electron on the lattice. Without electron-electron interaction, only the phonons can influence the electron dynamics and provide a relaxation channel. For some limiting cases it is convenient to describe the phonon system as a bath, but the numerical method that we use also covers the full dynamics of the phonons. This can become an obstacle because they belong to the (particle-) class of bosons, meaning they follow Bose-Einstein statistics. Therefore, it is possible to have an arbitrary number of phonon excitations occupying the same quantum state, which corresponds to a Hilbert space of arbitrary dimension if the particle number is not conserved, which is the case in our studies. According to the usual practice for many-particle systems we use second quantization to describe our quantum states. This also implies the use of creation and annihilation operators, rather than position and momentum operators.

1.2. Numerical methods

Using the second quantization the eigenvalue problem and time evolution get reduced from differential equations to combinatorial problems. This is why theorists often turn to numerical methods to study many-body problems. The development of algorithms that can efficiently simulate quantum mechanical systems has become an independent research area that not only physicists are interested in. Also chemists and biologists use and develop or refine some of these methods, e.g. mean field theory [13, 14]. In present-day many-body physics there is a large number of numerical methods that are geared to the needs of their specific studies. Some of the major branches are quantum Monte Carlo methods, cluster approximations and matrix product state (MPS) based algorithms. The latter one is chosen for the studies presented in this thesis.

The matrix product states have been mentioned under different names for the last three decades. In 1992 Fannes *et al.* [15] reported on finitely correlated states for spin systems with periodic boundary conditions. Three years later Östlund and Rommer [16] showed that in the thermodynamic limit ground states obtained with the density matrix renormalization group (DMRG) can also be obtained by a variational ansatz using “matrix product ground states”. The DMRG was introduced by White [17] in 1992 and quickly became the standard for ground state studies of one-dimensional many-body systems. Originally formulated in terms of a bipartite lattice it can naturally be written in the MPS language [18]. With this knowledge the ideas behind the DMRG were generalized to cover a wider range of systems. Additional work for developing a systematic understanding of the properties and pos-

sible applications of MPS has been done by Vidal [19, 20]. Since then new classes of states, related to MPS, have emerged, collectively referred to as tensor network states. Examples include the projected entangled-pair states (PEPS) [21], the multiscale entanglement renormalization group ansatz (MERA) [22] and generalizations to continuous systems [23, 24] describing quantum field theories.

1.3. Outline

In this thesis a modified time-evolving block-decimation (TEBD) algorithm is presented. The TEBD [20] is an MPS based scheme for the time evolution of one-dimensional lattice systems and the modification is the use of a specific basis that was found to represent ground states of systems with bosonic degrees of freedom very efficiently [25, 26]. In the next chapter we introduce the MPS in Sec. 2.1 and give their explicit form for a certain type of states. The subject of Sec. 2.2 is the TEBD with detailed instructions how to implement particle number conservation. Finally, the local basis optimization (LBO) is explained in Sec. 2.3, which completes Ch. 2. The content of the third chapter is the study of a highly excited electron that is coupled to phonons [27]. In Sec. 3.1 to Sec. 3.3 different limiting cases are discussed with analytical results to compare with numerical results of the TEBD-LBO method introduced in Ch. 2. In the crossover regime a smooth transition from one limit the next, e.g. from adiabatic to anti-adiabatic, is found. The dynamics of this regime are studied in Sec. 3.4 and the role of the optimal basis is investigated in Sec. 3.5. Presented in Ch. 4 are the results of the study of an electronic wave packet that is scattered by an electron-phonon (e-p) coupled structure [28]. The theory is explained in Sec. 4.1 and Sec. 4.2, where a connection with scattering theory for plane waves on a lattice is made. Three interesting phenomena are investigated thereafter. The transmission and reflection coefficients show non-linear behavior as a function the e-p coupling constant. A resonance mechanism related to the system of Sec. 3.1 is found for this problem and the optimal basis states used in our method give valuable insight into the physics of this system. All results regarding the transmission are presented in Sec. 4.3. The electron can transfer a part of its excess energy to the phonons, where some of this transferred energy might be reabsorbed by the electron, but a finite amount of phonon energy may persist permanently. In Sec. 4.4 we study this dissipated energy, but stress that, despite the name, the phonon system is not treated as a bath, but the full dynamics are captured by the TEBD-LBO. The time of transient self-trapping of the electron on the e-p coupled structure is investigated in Sec. 4.5, where different mechanisms that can bind the electron are found. Finally, all results and the performance of the TEBD-LBO method are summarized in Ch. 5. This work was supported by the *Deutsche Forschungsgemeinschaft* and is part of the *Forschergruppe 1807: Advanced Computational Methods for Strongly Correlated Quantum Systems*.

2. Time-evolving block-decimation with local basis optimization

One of the main goals in modern solid states physics is the development of numerical algorithms for large lattice systems of strongly correlated materials. Usually the Hilbert space dimension increases exponentially with the system size, but for bosonic excitations also the local Hilbert space dimension can be a limiting factor for numerical simulations. In principle a bosonic site is infinite dimensional, but a convenient cutoff for the number of states can usually be chosen. Among the most common numerical methods in this area are quantum Monte Carlo methods [29] and matrix product state (MPS) based algorithms, including the density matrix renormalization group method [17]. We are studying the time evolution of one-dimensional lattice systems with a specific number of fermions and a fluctuating number of bosons and, hence, turn to the time-evolving block-decimation (TEBD), which is a wave function based method suitable to address long chains. This algorithm is especially easy to parallelize because of its use of the Trotter-Suzuki decomposition as will be shown in Sec. 2.2. Another, mathematically equivalent, method for real-time evolution is the time-dependent DMRG (tDMRG) [30, 31, 18], that uses a different representation of the MPS. The problem of large local Hilbert spaces has already been addressed in ground state methods, where a local basis optimization [25, 26] and a splitting of one big site into several pseudo-sites [32] were combined with DMRG methods. The local basis optimization seems more promising for a combination with TEBD as it does not introduce long range interactions.

The algorithm we describe in this chapter has recently been introduced in Ref. [33]. It combines the advantages of matrix product state based methods, such as TEBD, and a local basis optimization. First, we give an introduction to matrix product states in Sec. 2.1 and then show how to implement time evolution using these states in Sec. 2.2, including a detailed description of a scheme to conserve the particle number. Finally, the local basis optimization and its implementation in the TEBD is explained in Sec. 2.3.

2.1. Matrix product states

In this subsection we give a short introduction to matrix product states. The possibility to represent a quantum state with a number of coefficients that is much smaller than the dimension of the full Hilbert space is crucial when dealing with strongly correlated lattice systems. The class of MPS provides such a representation and its versatility makes it applicable to a wide range of one-dimensional physical systems. The density matrix renormalization group method [17] was one of the major breakthroughs in one-dimensional solid state physics and, although not known at the time it was invented, the success of this algorithm relies on the properties of MPS. Nowa-

2. Time-evolving block-decimation with local basis optimization

days there are generalizations of this class to also cover two-dimensional lattices [21] and continuous systems [23].

For the derivation of the matrix product state representation we follow the formulations of Vidal [19]. For a one-dimensional lattice of L sites a generic pure quantum state is given by

$$|\psi\rangle = \sum_{k_1, \dots, k_L} c_{k_1, \dots, k_L} |k_1, k_2, \dots, k_L\rangle, \quad (2.1)$$

where the k_j label the states of site j in some standard basis, e.g. $k_j = \{\uparrow, \downarrow\}$ for spin- $\frac{1}{2}$ systems or $k_j = \{0, 1, \dots\}$ for bosons. The local Hilbert space dimensions d_j for each site j can be different and also arbitrarily large. This means the total Hilbert space has dimension $\dim(\mathcal{H}) = \prod_{j=1}^L d_j$ or simply $\dim(\mathcal{H}) = d^L$ for a homogeneous chain with $d_1 = d_2 = \dots = d_L = d$. The exponential growth in the system size is a real limiting factor, even for spin chains. Any change of the state leads to $\mathcal{O}(d^L)$ basic operations for updating the rank L tensor c that contains all coefficients of the state $|\psi\rangle$. The idea is now to find a representation that can approximate the state with less coefficients and may be updated efficiently in the case of local changes.

With a Schmidt decomposition the state (2.1) can be written as

$$|\psi\rangle = \sum_{\alpha_1=1}^{D_1} \lambda_{\alpha_1}^1 |\phi_{\alpha_1}^{[1]}\rangle |\phi_{\alpha_1}^{[2, \dots, L]}\rangle, \quad (2.2)$$

where the non-negative scalars $\lambda_{\alpha_1}^1$ are the Schmidt coefficients and $|\phi_{\alpha_1}^{[1]}\rangle$ and $|\phi_{\alpha_1}^{[2, \dots, L]}\rangle$ are the Schmidt vectors for the first site and the rest of the lattice, respectively.¹ With the Schmidt vector $|\phi_{\alpha_1}^{[1]}\rangle$ represented in the standard basis the state (2.2) becomes

$$|\psi\rangle = \sum_{\alpha_1=1}^{D_1} \sum_{k_1=1}^{d_1} \Gamma_{\alpha_1}^{1, k_1} \lambda_{\alpha_1}^1 |k_1\rangle |\phi_{\alpha_1}^{[2, \dots, L]}\rangle, \quad (2.3)$$

which, in the usual pictorial language of tensor network states [18], corresponds to

$$c_{k_1, \dots, k_L} = \begin{array}{c} |k_1 \quad |k_2 \quad |k_3 \quad \dots \quad |k_L \\ \boxed{\Gamma^1} \text{---} \boxed{\lambda^1} \text{---} \boxed{\tilde{c}^{L-1}} \end{array}. \quad (2.4)$$

The right Schmidt vector can also be rewritten as

$$|\phi_{\alpha_1}^{[2, \dots, L]}\rangle = \sum_{k_2=1}^{d_2} |k_2\rangle |\phi_{\alpha_1, k_2}^{[3, \dots, L]}\rangle = \sum_{k_2=1}^{d_2} |k_2\rangle \sum_{\alpha_2=1}^{D_2} \Gamma_{\alpha_1, \alpha_2}^{2, k_2} \lambda_{\alpha_2}^2 |\phi_{\alpha_2}^{[3, \dots, L]}\rangle, \quad (2.5)$$

where $\lambda_{\alpha_2}^2$ and $|\phi_{\alpha_2}^{[3, \dots, L]}\rangle$ are the coefficients and vectors of the Schmidt decomposition

¹The range of the index α_1 is in general the smaller of the Hilbert space dimensions $\dim(\mathcal{H}^{[1]})$ and $\dim(\mathcal{H}^{[2, \dots, L]})$.

2.1. Matrix product states

corresponding to the split $[1, 2] : [3, \dots, L]$, that need to be known for this step. Inserting (2.5) into (2.3) leads to

$$|\psi\rangle = \sum_{k_1=1}^{d_1} \sum_{k_2=1}^{d_2} \sum_{\alpha_1=1}^{D_1} \sum_{\alpha_2=1}^{D_2} \Gamma_{\alpha_1}^{1,k_1} \lambda_{\alpha_1}^1 \Gamma_{\alpha_1, \alpha_2}^{2,k_2} \lambda_{\alpha_2}^2 |k_1, k_2\rangle \left| \phi_{\alpha_2}^{[3, \dots, L]} \right\rangle, \quad (2.6)$$

or alternatively

$$c_{k_1, \dots, k_L} = \begin{array}{c} |k_1 \quad |k_2 \quad |k_3 \quad |k_4 \quad \dots \quad |k_L \\ \boxed{\Gamma^1} - \boxed{\lambda^1} - \boxed{\Gamma^2} - \boxed{\lambda^2} - \boxed{\tilde{C}^{L-2}} \end{array} . \quad (2.7)$$

The procedure of rewriting $|\phi^{[j, \dots, L]}\rangle$ in terms of $|\phi^{[j+1, \dots, L]}\rangle$ can now be iterated to get

$$|\psi\rangle = \sum_{k_1, \dots, k_L} \sum_{\alpha_1, \dots, \alpha_{L-1}} \Gamma_{\alpha_1}^{1,k_1} \lambda_{\alpha_1}^1 \Gamma_{\alpha_1, \alpha_2}^{2,k_2} \lambda_{\alpha_2}^2 \dots \lambda_{\alpha_{L-1}}^{L-1} \Gamma_{\alpha_{L-1}}^{L,k_L} |k_1, k_2, \dots, k_L\rangle \quad (2.8)$$

for a system with open boundary conditions and

$$|\psi\rangle = \sum_{k_1, \dots, k_L} \sum_{\alpha_1, \dots, \alpha_L} \Gamma_{\alpha_L \alpha_1}^{1,k_1} \lambda_{\alpha_1}^1 \Gamma_{\alpha_1 \alpha_2}^{2,k_2} \lambda_{\alpha_2}^2 \dots \lambda_{\alpha_{L-1}}^{L-1} \Gamma_{\alpha_{L-1} \alpha_L}^{L,k_L} |k_1, k_2, \dots, k_L\rangle \quad (2.9)$$

for periodic boundary conditions, respectively. If we imply standard matrix multiplication, we can omit the matrix indices α_j and take

$$|\psi\rangle = \sum_{k_1, \dots, k_L} \text{tr} \left[\Gamma^{1,k_1} \lambda^1 \Gamma^{2,k_2} \lambda^2 \dots \lambda^{L-1} \Gamma^{L,k_L} \right] |k_1, k_2, \dots, k_L\rangle \quad (2.10)$$

as the general form of an MPS, which is now represented by the tensor network

$$c_{k_1, \dots, k_L} = \begin{array}{c} |k_1 \quad |k_2 \quad \dots \quad |k_L \\ \boxed{\Gamma^1} - \boxed{\lambda^1} - \boxed{\Gamma^2} - \boxed{\lambda^2} - \dots - \boxed{\Gamma^L} \end{array} , \quad (2.11)$$

where the line from Γ^L to Γ^1 can be omitted for OBC's.² Every coefficient of this state is given by the trace of a product of matrices, hence the name. The λ^j are diagonal $D_j \times D_j$ -matrices and the Γ^j are $D_{j-1} \times D_j$ -matrices for fixed k_j , where $D_j = \min\{\dim(\mathcal{H}^{[1, \dots, j]}), \dim(\mathcal{H}^{[j+1, \dots, L]})\}$ are called the bond dimensions and we call $D = \max_j \{D_j\}$ the bond dimension of the MPS. To obtain the final representation of

$|\psi\rangle$ all Schmidt decompositions $|\psi\rangle = \sum_{\alpha_j=1}^{D_j} \lambda_{\alpha_j}^j \left| \phi_{\alpha_j}^{[1, \dots, j]} \right\rangle \left| \phi_{\alpha_j}^{[j+1, \dots, L]} \right\rangle$ need to be known

²The picture is also correct for OBC's. In this case the redundant contracted index can only take one value, i.e. $D_L \equiv D_0 = 1$.

2. Time-evolving block-decimation with local basis optimization

and in return all Schmidt decompositions are given by (2.8) or (2.9), respectively.

This is an exact representation of the generic state $|\psi\rangle$, which has the same number of coefficients as (2.1), but in (2.10) it is easy to see how to reduce this number preferably. If we drop the smallest $\lambda_{\alpha_j}^j$ the bond dimensions decrease, while the error remains as small as possible. This is very effective in many physical systems, because the Schmidt coefficients are exponentially decaying for ground states. This is connected to the issue of the entropy area law [34, 35], which states in one dimension that often the entanglement entropy of any region is bounded by a constant. We are more interested in time evolution, rather than ground states, but still the MPS representation provides a good approximation to all states in our simulations with a convenient bond dimension. If D scales at most polynomially in L , the reduction of the total number of parameters from $\prod_j d_j$ to $\sum_j d_j \cdot D_{j-1} \cdot D_j$ can be tremendous.

There are several reasons why the MPS are such a successful class of states. As we have already argued, any pure state of a one-dimensional lattice system can be represented by an MPS with sufficiently large bond dimension and the number of parameters to describe a certain state with finite entanglement entropy can be reduced in a very controlled manner. Furthermore, local updates can be done efficiently in the sense that, for example, an operator $X_{j,j+1}$, that acts only on sites j and $j+1$, will only effect Γ^j , λ^j and Γ^{j+1} . Also the norm $\langle\psi|\psi\rangle$ as well as expectation values of local observables can be obtained with an effort that is linear in L , for a fixed bond dimension, or even independent of it. If one uses the canonical form, the MPS fulfills the orthonormalization conditions

$$\sum_{k_j=1}^{d_j} \Gamma^{j,k_j} (\lambda^j)^2 (\Gamma^{j,k_j})^\dagger = \mathbf{1} \quad (2.12)$$

and

$$\sum_{k_j=1}^{d_j} (\Gamma^{j,k_j})^\dagger (\lambda^{j-1})^2 \Gamma^{j,k_j} = \mathbf{1}, \quad (2.13)$$

which imply the normalization of the state and reduce obtaining expectation values to a contraction³

$$\langle\psi|X_j|\psi\rangle = \begin{array}{c} \begin{array}{ccccc} \boxed{\lambda^{j-1}} & \boxed{\Gamma^j} & \boxed{\lambda^j} & & \\ & | & & & \\ & \boxed{X_j} & & & \\ & | & & & \\ \boxed{\lambda^{j-1}} & \boxed{\Gamma^j} & \boxed{\lambda^j} & & \end{array} \end{array} \quad (2.14)$$

for an operator X_j acting only on site j . The diagonal matrices λ^j carry the information about the entanglement between blocks $[0, \dots, j]$ and $[j+1, \dots, L]$ and fulfill the

³In this pictorial language hermitian conjugation is expressed through the shift of the physical index from outgoing line to the top to outgoing line to the bottom.

condition

$$\text{tr}[(\lambda^j)^2] = 1. \quad (2.15)$$

The Γ 's on the other hand have no physical meaning, so one can make the transformation $\Gamma^j \rightarrow g_{j-1}^{-1} \Gamma^j \lambda^j g_j (\lambda^j)^{-1}$ for any set of invertible matrices g without affecting the state $|\psi\rangle$. This gauge freedom is useful to bring an MPS in a desired form, e.g. the canonical one.

In the next section we introduce an algorithm for time evolution with MPS. To get a suitable initial state for a numerical simulation it is possible to first store the state in the form of (2.1) and then do the Schmidt decompositions as described above. However, for simple states there is an easier way. We focus on a state with one electron on an otherwise empty lattice with OBC's, which is equivalent to a spin system where all but one spin are pointing in the same direction or any other state with one excitation. Therefore, the physical indices can be restricted to $k_j \in \{0, 1\}$, $\forall j \in \{1, \dots, L\}$, where $k_j = 1$ corresponds to the electron occupying the site j . For an electronic wave function $\psi : [1, \dots, L] \rightarrow \mathbb{C}$ we define $P(j) = \sum_{l=1}^j |\psi(l)|^2$ as the probability to find the electron in the left block $[1, \dots, j]$ and, hence, for a normalized state $P(L) = 1$. We impose a block structure on the matrices to ensure that the particle number is correct. In this simple case a bond dimension of $D = 2$ is sufficient, so that the blocks are just numbers. For the outer vectors we choose

$$\Gamma^{1,0} = (1, 0), \quad \Gamma^{1,1} = \left(0, \frac{\psi(1)}{|\psi(1)|}\right) \quad (2.16)$$

and

$$\Gamma^{L,0} = \begin{pmatrix} 0 \\ 1 \end{pmatrix}, \quad \Gamma^{L,1} = \begin{pmatrix} \frac{\psi(L)}{|\psi(L)|} \\ 0 \end{pmatrix} \quad (2.17)$$

and the other Γ 's are given by

$$\Gamma^{j,0} = \begin{pmatrix} \frac{1}{\sqrt{1-P(j-1)}} & 0 \\ 0 & \frac{1}{\sqrt{P(j)}} \end{pmatrix}, \quad \Gamma^{j,1} = \begin{pmatrix} 0 & \frac{\psi(j)}{\sqrt{P(j)(1-P(j-1))}} \\ 0 & 0 \end{pmatrix}. \quad (2.18)$$

Together with

$$\lambda^j = \begin{pmatrix} \sqrt{1-P(j)} & 0 \\ 0 & \sqrt{P(j)} \end{pmatrix} \quad (2.19)$$

these tensors have a non-vanishing contraction only if there is exactly one index $k_j = 1$. It is easy to check that this MPS fulfills the orthonormalization conditions (2.12) and (2.13), as well as (2.15) (see Appendix A). We start all our numerical simulations with an initial state of this form. In the standard representation this

2. Time-evolving block-decimation with local basis optimization

state can be written with

$$c_{k_1, \dots, k_L} = \sum_{j=1}^L \psi(j) \delta_{1k_j} \prod_{l \neq j} \delta_{0k_l}. \quad (2.20)$$

In practice it may be convenient to start simulations with an electronic wave function that is non-zero only on a small part $j_l < j < j_r$ of the lattice (see Ch. 4). In this case we have $P(j) = 0, \forall j < j_l$ and $1 - P(j) = 0, \forall j > j_r$, respectively, which seems to contradict the representation (2.18). If this is considered as a limit $P(j) \rightarrow 0$ one can check that all contractions of the MPS remain finite or vanish due to the finite product of Γ^j and either λ^j or λ^{j-1} . To store this state in its exact form and spare some computational time one can set $\Gamma^{j,0} = \lambda^j = 1$ and $\Gamma^{j,1} = 0, \forall j \notin \{j_l, \dots, j_r\}$ and use the definitions (2.16) to (2.19), with the appropriately shifted first and last lattice index, for $j \in \{j_l, \dots, j_r\}$.⁴ This is the natural representation of an MPS for a piecewise empty lattice and the matrix dimension increases normally in time evolution schemes.

The structure of the tensors (2.16) to (2.19) can be kept in the algorithm presented in the next section. With growing entanglement entropy the numbers will become blocks, such that

$$\Gamma^{j,0} = \begin{pmatrix} A & 0 \\ 0 & B \end{pmatrix}, \quad \Gamma^{j,1} = \begin{pmatrix} 0 & C \\ 0 & 0 \end{pmatrix}, \quad (2.21)$$

where blocks A and C have the same number of rows, while B and C have the same number of columns. The outer vectors are changing accordingly and the λ 's are bipartite in the same way as the columns of the Γ with the same lattice index. The same method also works for more particles if the number of blocks is adjusted appropriately. Alternatively, one can introduce an additional index that undertakes the part of the blocks. The particle number conservation induced by this block structure is an important example of a symmetry that can be used to achieve a higher efficiency in a simulation with MPS.

2.2. Time-evolving block-decimation

The class of MPS is particularly suited for representing ground states, but its properties also allow for efficient simulations of time evolution. The following scheme is called the time-evolving block-decimation algorithm [20] (TEBD). We consider non-dissipative Hamiltonians, that do not depend explicitly on time, which leads to the explicit form $U(t) = e^{-iHt}$ for the time evolution operator in natural units with $\hbar = 1$. Additionally, we restrict ourselves to nearest neighbor interaction. In this case we can split the Hamiltonian into even and odd part

$$H = \sum_{j=0}^{L-1} H_{j,j+1} = H_e + H_o = \sum_{j=0}^{L/2-1} H_{2j,2j+1} + \sum_{j=0}^{L/2-1} H_{2j+1,2j+2}, \quad (2.22)$$

⁴One must also set $\lambda^{j_r} = 1$ due to the fact that Γ^{j_r} is a column vector.

2.2. Time-evolving block-decimation

where all terms in H_e commute, as do all terms in H_o . With this splitting we can apply a second order Trotter-Suzuki decomposition [36, 37] to the time evolution operator

$$U(t) = e^{-iH_e \frac{\tau}{2}} e^{-iH_o \tau} \left(e^{-iH_e \tau} e^{-iH_o \tau} \right)^{\frac{t}{\tau}-1} e^{-iH_e \frac{\tau}{2}} + \mathcal{O}(\tau^2 t), \quad (2.23)$$

introducing an error that is quadratic in the sufficiently small chosen size τ of the time steps if the system evolves for a finite time t . In our simulations we usually have $\tau = 5 \cdot 10^{-4}$ and $10 < t < 100$. The further decomposition $e^{-iH_{e(o)} \tau} = \prod_j e^{-iH_{2j(+1), 2j+1(2)} \tau}$ does not introduce any additional error. All of these local updates can be done simultaneously, which yields a simple and effective way of parallelizing the algorithm. Ideally, the computational time can be reduced by a factor of $2/L$. Even without parallelization, acting with the time evolution operator is reduced to a sequence of local unitary operations, acting only on two adjacent lattice sites. For a state in the MPS representation, as introduced in Sec. 2.1, this means a sequence of updates involving only two Γ 's each. One of these updates consists of the following steps. We build the matrix ϕ with components

$$\phi_{x,y} = \left[\lambda^{j-1} \Gamma^j \lambda^j \Gamma^{j+1} \lambda^{j+1} \right]_{x,y} = \text{Diagram}, \quad (2.24)$$

where $x = \{\alpha_1, k_j\}$ and $y = \{\alpha_2, k_{j+1}\}$ are composite indices. Then the time evolution operator is applied to obtain

$$\tilde{\phi}_{x',y'} = \sum_{k_j, k_{j+1}} U_{k'_j, k'_{j+1}}^{k_j, k_{j+1}} \phi_{x,y} = \text{Diagram}, \quad (2.25)$$

The Hamiltonians that we use are naturally, i.e. in the standard boson number basis, represented by a sparse matrix, so that the above contraction can be done efficiently with a sufficiently precise approximation. By using a Taylor expansion of U up to $\mathcal{O}(\tau^3)$ the computational cost of (2.25) is reduced from $\mathcal{O}(D^2 d^4)$ to $\mathcal{O}(D^2 d^2)$, while the additional error is negligible compared to the Trotter error. One way to proceed would be to make a singular value decomposition (SVD) $\tilde{\phi} = u \lambda v$, where λ is a diagonal matrix and u and v fulfill the orthonormality conditions $u^\dagger u = v v^\dagger = \mathbf{1}$. The components of the updated MPS tensors are then

$$\tilde{\lambda}_{\alpha_3}^j = \lambda_{\alpha_3}, \quad \tilde{\Gamma}_{\alpha_1, \alpha_3}^{j, k'_j} = \frac{1}{\lambda_{\alpha_1}^{j-1}} u_{x', \alpha_3} \quad \text{and} \quad \tilde{\Gamma}_{\alpha_3, \alpha_2}^{j+1, k'_{j+1}} = v_{\alpha_3, y'} \frac{1}{\lambda_{\alpha_2}^{j+1}}. \quad (2.26)$$

2. Time-evolving block-decimation with local basis optimization

This is one of two equivalent approaches, where we chose the one described in the following. Instead of an SVD one can make a diagonalization of the density matrix for the left or right block corresponding to a cut of the system at bond j . We get the reduced density matrix of one block by tracing out the other one. With the matrix $\tilde{\phi}$ this is achieved by

$$\rho^L = \tilde{\phi} \tilde{\phi}^\dagger = \begin{array}{c} \text{---} \lambda^{j-1} \text{---} \Gamma^j \text{---} \lambda^j \text{---} \Gamma^{j+1} \text{---} \lambda^{j+1} \text{---} \\ | \\ \text{---} U \text{---} \\ | \\ \text{---} U \text{---} \\ | \\ \text{---} \lambda^{j-1} \text{---} \Gamma^j \text{---} \lambda^j \text{---} \Gamma^{j+1} \text{---} \lambda^{j+1} \text{---} \end{array} = u \lambda^2 u^\dagger \quad (2.27)$$

and

$$\rho^R = \tilde{\phi}^\dagger \tilde{\phi} = \begin{array}{c} \lambda^{j-1} \text{---} \Gamma^j \text{---} \lambda^j \text{---} \Gamma^{j+1} \text{---} \lambda^{j+1} \text{---} \bullet \\ | \\ \text{---} U \text{---} \\ | \\ \text{---} U \text{---} \\ | \\ \lambda^{j-1} \text{---} \Gamma^j \text{---} \lambda^j \text{---} \Gamma^{j+1} \text{---} \lambda^{j+1} \text{---} \bullet \end{array} = v^\dagger \lambda^2 v. \quad (2.28)$$

Thus the diagonalization yields λ^2 and either u or v . For the density matrix of the left block ρ^L the eigenvectors are the columns of u and we obtain v by the additional step $v_{\alpha_3, y'} = (u_{x', \alpha_3})^\dagger \tilde{\phi}_{x', y'} / \lambda_{\alpha_3}$. Likewise the eigenvectors of ρ^R are the columns of v^\dagger and the components of u are $u_{x', \alpha_3} = \tilde{\phi}_{x', y'} (v_{\alpha_3, y'})^\dagger / \lambda_{\alpha_3}$. The $\tilde{\lambda}$ and $\tilde{\Gamma}$'s are then given by (2.26).

In this formulation one can spare some computational time with the right choice of either using ρ^L or ρ^R . Building the former scales as $\mathcal{O}(D_{j-1}^2 D_{j+1} d_j^2 d_{j+1})$, while building the latter scales as $\mathcal{O}(D_{j-1} D_{j+1}^2 d_j d_{j+1}^2)$. Additionally, the diagonalization scales as $\mathcal{O}(D_{j-1}^3 d_j^3)$ and $\mathcal{O}(D_{j+1}^3 d_{j+1}^3)$, respectively. Finally, obtaining v and u has the same scaling. In unsymmetrical systems, where the bond dimensions and local Hilbert spaces can differ significantly even on neighboring sites, choosing one block density matrix over the other reduces the scaling from cubic to linear in the higher dimensions.

The new MPS already fulfills all orthonormalization conditions. Since $\tilde{\lambda}^j$ is composed of the eigenvalues of a density matrix, (2.15) is naturally fulfilled. Also (2.13)

for Γ^j and (2.12) for Γ^{j+1} follow directly from the properties of u and v , respectively. The remaining two conditions can be checked by inserting (2.24) to (2.27) and applying the orthonormality conditions for the original MPS tensors:

$$\begin{aligned}
\sum_{k_j} \tilde{\Gamma}^{j,k_j} (\lambda^j)^2 (\tilde{\Gamma}^{j,k_j})^\dagger &= \sum_{k_j} \frac{1}{\lambda^{j-1}} u_{k_j} (\lambda^j)^2 u_{k_j}^\dagger \frac{1}{\lambda^{j-1}} = \sum_{k_j} \frac{1}{\lambda^{j-1}} \rho_{k_j,k_j}^L \frac{1}{\lambda^{j-1}} \\
&= \sum_{k_j, k_{j+1}} \sum_{n_j, n_{j+1}} \sum_{m_j, m_{j+1}} \left[\Gamma^{j,n_j} \lambda^j \Gamma^{j+1, n_{j+1}} (\lambda^{j+1})^2 \right. \\
&\quad \left. (\Gamma^{j+1, m_{j+1}})^\dagger \lambda^j (\Gamma^{j, m_j})^\dagger U_{n_j, n_{j+1}}^{k_j, k_{j+1}} (U_{k_j, k_{j+1}}^{m_j, m_{j+1}})^\dagger \right] \quad (2.29) \\
&= \sum_{n_j, n_{j+1}} \Gamma^{j, n_j} \lambda^j \Gamma^{j+1, n_{j+1}} (\lambda^{j+1})^2 (\Gamma^{j+1, n_{j+1}})^\dagger \lambda^j (\Gamma^{j, n_j})^\dagger \\
&= \sum_{n_j} \Gamma^{j, n_j} \lambda^j \mathbb{1} \lambda^j (\Gamma^{j, n_j})^\dagger = \mathbb{1}
\end{aligned}$$

The same can be done for $\sum_{k_{j+1}} (\tilde{\Gamma}^{j+1, k_{j+1}})^\dagger (\lambda^j)^2 \tilde{\Gamma}^{j+1, k_{j+1}}$. Therefore the local update is complete at this point.

For these orthonormality conditions to be exact we would have to use all eigenvalues of the reduced density matrix.⁵ In this case the bond dimension of the MPS would grow exponentially with the number of time steps $\frac{t}{\tau}$. The most effective truncation of the Hilbert space is to keep only those eigenvalues of the block density matrices with the highest weights, which is the same idea as in DMRG. There are two ways of implementing such a truncation. Either one chooses a maximal bond dimension D_{\max} , keeps only the D_{\max} highest weighted eigenstates and, therefore, controls the computational time needed or one discards only those eigenvalues with a weight below a certain cutoff and, thereby, controls the error. Making the right choice for either kind of cutoff is more involved for time evolution than it is for ground state methods. Maybe a certain cutoff for the weights is sufficient to approximate the state at time t to a satisfying precision, but one might discard states, which would have a high weight at later times, during the process. For the same reason the discarded weight is not a good measure for the total error made in a simulation of a system evolving in time. Also choosing a maximal bond dimension requires some knowledge of the physics of the system, especially the entanglement. For open boundary conditions the bond dimensions vary significantly from the edges to the middle of the system, hence a different D_{\max} for each lattice site, or at least for different regions on the lattice, would be convenient, but even more involved.

There is another cutoff one has to choose conditioned by bosonic degrees of freedom. The local Hilbert space dimension is infinite if there is no particle conservation for the bosons. When working in the boson number basis, the common choice is to use only the lowest eigenstates of the number operator up to some well chosen number M .

⁵Also the time evolution operator must not be approximated to a finite order, but this error is again negligible for small enough time steps.

2. Time-evolving block-decimation with local basis optimization

Again some insight into the physics of the system is required to find an appropriate cutoff for the size of the boson basis. In our simulations we do not use a specific size for all local Hilbert space dimensions, but instead dynamically increase each one individually, when needed. Our initial state is always the tensor product of some electronic state and the phonon vacuum, hence $M = 4$ is sufficient to apply the Taylor expanded time evolution operator.⁶ If, after a time step τ , the probability to find an occupation of the highest phonon state is larger than a certain cutoff, the dimension M for this site is increased by one. This dynamical increase is particularly efficient in our implementation as we avoid the costly step of computing $e^{-iH_{j,j+1}\tau}$ exactly, which would now have to be redone for every size of the local Hilbert space dimension. For larger time steps one may have to start with a larger dimension and also enlarge it by more than one at each step. If the cutoff is well chosen, this method provides an accurate simulation without waste of computational time due to unnecessarily large dimensions.

To illustrate the particle number conservation during the TEBD, we focus on the special case of $M = 2$ and $d_j = 4$, $\forall j \in \{1, \dots, L\}$, which corresponds, for the system studied in the next chapter, to a lattice with one electron and a non-conserved number of phonons that can take the values $\{0, 1\}$ at each site. The Γ 's have the same block structure as in (2.21)

$$\Gamma^{j,0(1)} = \begin{pmatrix} A & 0 \\ 0 & B \end{pmatrix}, \quad \Gamma^{j,2(3)} = \begin{pmatrix} 0 & C \\ 0 & 0 \end{pmatrix}, \quad (2.30)$$

where the matrices have the same structure for the first M and last M values of k_j , respectively. We denote blocks with equal dimensions with the same letter, which does not mean that all entries are equal. The matrix ϕ then inherits the form

$$\phi = \begin{pmatrix} a & 0 & a & 0 & 0 & c & 0 & c \\ 0 & b & 0 & b & 0 & 0 & 0 & 0 \\ a & 0 & a & 0 & 0 & c & 0 & c \\ 0 & b & 0 & b & 0 & 0 & 0 & 0 \\ 0 & c & 0 & c & 0 & 0 & 0 & 0 \\ 0 & 0 & 0 & 0 & 0 & 0 & 0 & 0 \\ 0 & c & 0 & c & 0 & 0 & 0 & 0 \\ 0 & 0 & 0 & 0 & 0 & 0 & 0 & 0 \end{pmatrix}. \quad (2.31)$$

The application of the time evolution operator U does not change the shape so that

⁶The Hamiltonians used in this thesis include no higher order terms in the phonon creation operators.

$\tilde{\phi}$ looks just like ϕ .⁷ For the left block density matrix we then obtain

$$\rho^L = \begin{pmatrix} f & 0 & f & 0 & 0 & 0 & 0 & 0 \\ 0 & g & 0 & g & h & 0 & h & 0 \\ f & 0 & f & 0 & 0 & 0 & 0 & 0 \\ 0 & g & 0 & g & h & 0 & h & 0 \\ 0 & h^\dagger & 0 & h^\dagger & i & 0 & i & 0 \\ 0 & 0 & 0 & 0 & 0 & 0 & 0 & 0 \\ 0 & h^\dagger & 0 & h^\dagger & i & 0 & i & 0 \\ 0 & 0 & 0 & 0 & 0 & 0 & 0 & 0 \end{pmatrix} \rightarrow \begin{pmatrix} f & f & 0 & 0 & 0 & 0 & 0 & 0 \\ f & f & 0 & 0 & 0 & 0 & 0 & 0 \\ 0 & 0 & g & g & h & h & 0 & 0 \\ 0 & 0 & g & g & h & h & 0 & 0 \\ 0 & 0 & h^\dagger & h^\dagger & i & i & 0 & 0 \\ 0 & 0 & h^\dagger & h^\dagger & i & i & 0 & 0 \\ 0 & 0 & 0 & 0 & 0 & 0 & 0 & 0 \\ 0 & 0 & 0 & 0 & 0 & 0 & 0 & 0 \end{pmatrix}, \quad (2.32)$$

where we reordered the rows and columns of ρ^L to make it block diagonal. The eigenvalues and entries of the eigenvectors are not affected by this reordering, since there are two proper subspaces present. The blocks can be diagonalized separately, where the big block in the middle has in general dimension $D_{j-1}M_j \times D_{j-1}M_j$ and the small block in the upper left corner has dimension $D_{j-1}^{\text{bl}}M_j \times D_{j-1}^{\text{bl}}M_j$, with D_{j-1}^{bl} being the number of rows of block A in (2.30). Finally, the $\tilde{\Gamma}$'s and λ have to be build with respect to this structure. We rewrite (2.32) as

$$\rho^L = \begin{pmatrix} \rho_1 & 0 & 0 \\ 0 & \rho_2 & 0 \\ 0 & 0 & 0 \end{pmatrix} \quad (2.33)$$

and find

$$\rho_1 = u_1 \lambda_1 u_1^\dagger \quad \text{and} \quad \rho_2 = u_2 \lambda_2 u_2^\dagger. \quad (2.34)$$

Then the eigenvectors, i.e. the columns of u_1 and u_2 , are split into M and $2M$ parts, respectively, where

$$u_1 = \begin{pmatrix} u_1^0 \\ u_1^1 \\ \vdots \\ u_1^{M-1} \end{pmatrix} \quad \text{and} \quad u_2 = \begin{pmatrix} u_2^{0,0} \\ \vdots \\ u_2^{0,M-1} \\ u_2^{1,0} \\ \vdots \\ u_2^{1,M-1} \end{pmatrix}, \quad (2.35)$$

such that the matrices

$$\tilde{\Gamma}^{j,k} = \begin{pmatrix} u_1^k & 0 \\ 0 & u_2^{0,k} \end{pmatrix} \quad \text{and} \quad \tilde{\Gamma}^{j,M+k} = \begin{pmatrix} 0 & u_2^{1,k} \\ 0 & 0 \end{pmatrix}, \quad (2.36)$$

have the proper dimension. The number of columns of each block is given by the

⁷Some of the blocks in (2.30) and (2.31) could also be zero if the probability to find the electron or a phonon, respectively, on a certain site is zero. In this case the application of U may yield new non-zero entries.

2. Time-evolving block-decimation with local basis optimization

amount of kept eigenvalues of either ρ_1 or ρ_2 . Consequently, the diagonal matrix λ^j is bipartite, where the upper entries are the eigenvalues of ρ_1 and the lower entries are the eigenvalues of ρ_2 , each in descending order. To obtain $\tilde{\Gamma}^{j+1}$ we have to multiply u_1 and u_2 with $\tilde{\phi}$ in a proper way. As we have argued $\tilde{\phi}$ has the same structure as ϕ in (2.31), but we can make row and column permutations similar to the ones performed in (2.32) and call the result again $\tilde{\phi}$. Then we may write

$$\tilde{\phi} = \begin{pmatrix} \tilde{\phi}_{00} & 0 & 0 & \tilde{\phi}_{03} \\ 0 & \tilde{\phi}_{11} & 0 & 0 \\ 0 & \tilde{\phi}_{21} & 0 & 0 \\ 0 & 0 & 0 & 0 \end{pmatrix}, \quad (2.37)$$

where all entries are blocks, each composed of four blocks from (2.31). With this we can conclude

$$\tilde{\Gamma}^{j+1,k} = \begin{pmatrix} \frac{1}{\lambda^{j,0}} [(u_1)^\dagger \tilde{\phi}_{00}]^k \frac{1}{\lambda^{j+1,0}} & 0 \\ 0 & \frac{1}{\lambda^{j,1}} [(u_2^0)^\dagger \tilde{\phi}_{11} + (u_2^1)^\dagger \tilde{\phi}_{21}]^k \frac{1}{\lambda^{j+1,1}} \end{pmatrix} \quad (2.38)$$

and

$$\tilde{\Gamma}^{j+1,M+k} = \begin{pmatrix} 0 & \frac{1}{\lambda^{j,0}} [(u_1)^\dagger \tilde{\phi}_{03}]^k \frac{1}{\lambda^{j+1,1}} \\ 0 & 0 \end{pmatrix}, \quad (2.39)$$

where we have adopted the notation from the split of u_1 and u_2 for the λ 's and the products of u and $\tilde{\phi}$. Alternatively, one could also use the density matrix for right block in the same way. This block structure ensures particle number conservation for one particle type throughout the simulation and also reduces the computational effort due to the smaller matrix dimensions $\dim(\rho_1) < \dim(\rho_2) = \frac{1}{4} \dim(\rho^L)$. One has to be careful when choosing the cutoff for the density matrix eigenvalues, or alternatively the maximal bond dimension, because one of the blocks may have eigenvalues orders of magnitude larger than the other, but both need to be taken into account. A possible solution is to use a fixed cutoff multiplied with the trace of the respective density matrix.

2.3. The optimal basis

The TEBD is an efficient algorithm for slightly entangled systems, where the MPS representation with a small bond dimension D is sufficient for a good approximation of the state $|\psi(t)\rangle$. But for bosonic degrees of freedom also the cubic scaling in the local Hilbert space dimension d has to be considered. Therefore, we combine the TEBD with a local basis optimization (LBO), which was already successfully combined with ground state methods [25, 26] and, recently, also with a time-dependent variational principle for MPS to study the spin-boson model [38]. The basic idea is to use the eigenbases of the single-site reduced density matrices instead of the bare bases, which is similar to DMRG, with the difference that we are not looking at bonds, but at

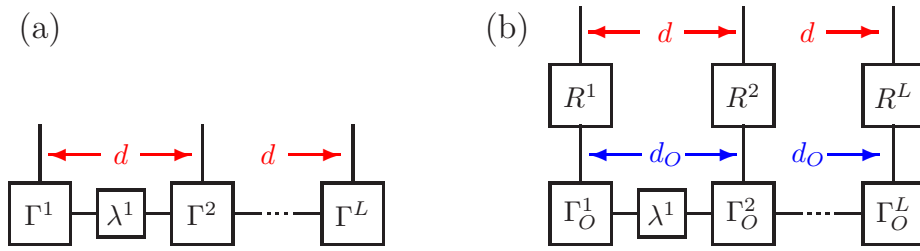


FIG. 2.1.: Graphical representation of the MPS (a) in the original TEBD algorithm and in the TEBD-LBO algorithm. From Ref. [33].

sites. We call this the optimal basis as it allows us to reduce the dimension of a site efficiently by discarding those eigenstates with the lowest weights. To implement the local basis optimization in our TEBD algorithm we have to add a few more steps to the local updates, since the optimal states and their weights can both change significantly during time evolution [27], which makes it necessary to compute them in every time step.

Assume that you know the MPS in the optimal basis⁸ and build the matrix ϕ_O analogously to (2.24) with components

$$(\phi_O)_{r,s} = \left[\lambda^{j-1} \Gamma_O^j \lambda^j \Gamma_O^{j+1} \lambda^{j+1} \right]_{r,s}, \quad (2.40)$$

where $r = \{\alpha_1, f_j\}$ and $s = \{\alpha_2, f_{j+1}\}$ are the composite indices for the optimal basis. In the next step we go back to the bare basis, because applying the time evolution operator in the optimal basis has some disadvantages. The Hamiltonian would have to be recalculated in every time step for every bond and also lose its sparseness, leading to $\mathcal{O}(d^4 d_O)$ basic operations to transform the Hamiltonian into the optimal representation and $\mathcal{O}(D^2 d_O^4)$ operations to act with H on ϕ_O . Furthermore, the occupied and unoccupied site do not have the same optimal basis, which makes a mixing of their phonon states, caused by the hopping term of the Hamiltonian, more involved and doubles the size of the optimal basis during these steps. Therefore, a change of the basis is more efficient at this point.

As can be seen in Fig. 2.1, the relation between optimal and bare basis is

$$\Gamma^{j,k_j} = \sum_{f_j} R_{k_j, f_j}^j \Gamma_O^{j, f_j}, \quad (2.41)$$

where the R matrices contain the optimal modes represented in the bare basis. Hence, ϕ is given by

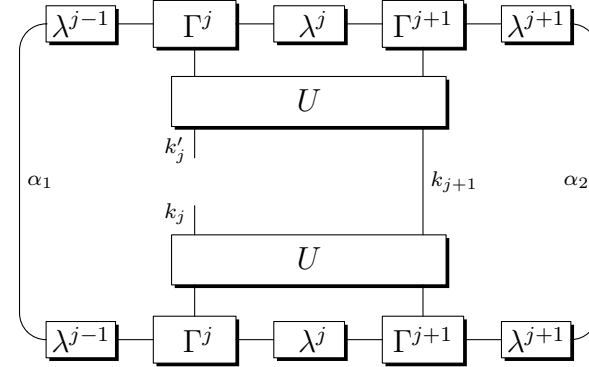
$$\phi_{x,y} = \sum_{f_j, f_{j+1}} R_{k_j, f_j}^j R_{k_{j+1}, f_{j+1}}^{j+1} (\phi_O)_{r,s}, \quad (2.42)$$

where we need $\mathcal{O}(D^3 d_O^2)$ basic operations for ϕ_O and $\mathcal{O}(D^2 d^2 d_O)$ for ϕ . Applying

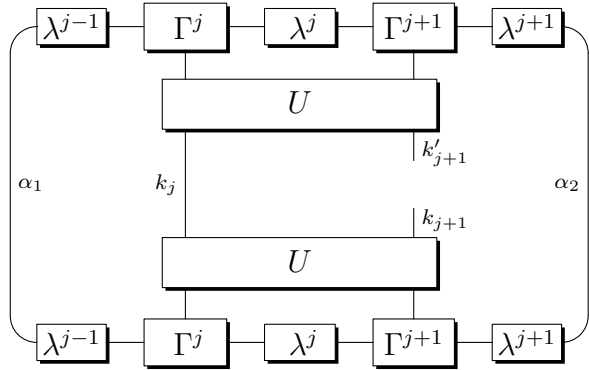
⁸This is usually the case at the start of the simulation when using a simple initial state like the phonon vacuum.

2. Time-evolving block-decimation with local basis optimization

the time evolution operator to obtain $\tilde{\phi}$ can then be done exactly as in the unmodified TEBD algorithm. The new optimal modes are the eigenstates of the single-site reduced density matrices

$$\rho_{k_j, k'_j}^j = \sum_{\alpha_1, y} \tilde{\phi}_{x, y} (\tilde{\phi}_{x', y})^\dagger =$$

(2.43)

and

$$\rho_{k_{j+1}, k'_{j+1}}^{j+1} = \sum_{\alpha_2, x} (\tilde{\phi}_{x, y'})^\dagger \tilde{\phi}_{x, y} =$$

(2.44)

which take $\mathcal{O}(D^2 d^3)$ basic operations to be determined and additional $\mathcal{O}(d^3)$ operations to be diagonalized. The modes are stored in the matrices \tilde{R}^j and \tilde{R}^{j+1} and are then used to transfer to the new optimal basis with

$$(\tilde{\phi}_O)_{r, s} = \sum_{k_j, k_{j+1}} \tilde{\phi}_{x, y} (\tilde{R}^j)_{k_j, f_j}^\dagger (\tilde{R}^{j+1})_{k_{j+1}, f_{j+1}}^\dagger. \quad (2.45)$$

The remaining steps of the local update can be done efficiently in the optimal basis. In particular the calculation and diagonalization of the block density matrix now scale as $\mathcal{O}(D^3 d_0^3)$, which is much faster than in the original algorithm, given that $d_0 < d$. At the end of the update we obtain the Γ 's in the optimal representation. Hence, they can directly be used in the next update.

In addition to the above mentioned extra steps in the local updates we also made a further separation of the Hamiltonian into $H = H_e + H_o + H_{s-s}$, where H_{s-s} contains all the terms that act only on a single site. The second order Trotter-Suzuki

step	\mathcal{O}	
	TEBD	TEBD-LBO
ϕ	$D^3 d^2$	$D^3 d_O^2 + D^2 d^2 d_O$
$\tilde{\phi}$	$D^2 d^2$	$D^2 d^2$
$\rho^{L,R}$	$D^3 d^3$	$D^3 d_O^3$
Γ 's	$D^3 d^2$	$D^3 d_O^2$
$\rho^{j,j+1}$	0	$D^2 d^3$
$\tilde{\phi}_O$	0	$D^2 d^2 d_O$
total	$D^3 d^3$	$D^2 d^3$ or $D^3 d_O^3$

Table 2.1.: A comparison of the TEBD with and without local basis optimization. The scaling for the most important steps for a homogeneous system with $D_j = D$, $d_j = d$, $\forall j \in \{1, \dots, L\}$ is given. For $\rho^{L,R}$ and $\rho^{j,j+1}$ this means the overall scaling of the computation of the matrix and the diagonalization.

decomposition of U then reads

$$\begin{aligned}
 U(t) = & e^{-iH_e \frac{\tau}{2}} e^{-iH_{s-s} \frac{\tau}{2}} e^{-iH_o \tau} e^{-iH_{s-s} \frac{\tau}{2}} \\
 & \left[e^{-iH_e \tau} e^{-iH_{s-s} \frac{\tau}{2}} e^{-iH_o \tau} e^{-iH_{s-s} \frac{\tau}{2}} \right]^{\frac{t}{\tau}-1} e^{-iH_e \frac{\tau}{2}} + \mathcal{O}(\tau^2 t).
 \end{aligned} \tag{2.46}$$

The time evolution operator of a single site acts directly on the R matrices, which, together with our Taylor expansion of U , results in a scaling of $\mathcal{O}(d d_O)$ for a local update. This is negligible compared to the cost for a two site update.

Using the optimal basis implies choosing another two cutoffs. The number of optimal states cannot exceed the number of bare states, but it can be further constrained. Also a cutoff for the magnitude of the single-site reduced density matrix eigenvalues may be chosen. For the purpose of testing this method and compare it to other results we use the following cutoffs: all block density matrix eigenvalues with $\lambda^i < 10^{-15}$ and optimal modes with weight smaller than 10^{-13} are discarded. The local Hilbert space dimension of site j is increased if the probability to find the current maximal number of phonons on that site is $w^j > 10^{-7}$. The dimensions D , d and d_O usually converge at some point and we do not use an additional restriction to the maximal number of kept states. For time steps $\tau = 5 \cdot 10^{-4}$ these cutoffs provide accurate results, but they can be adapted to achieve better performance. Especially the bond dimension is usually larger than needed and can be reasonably restricted without losing noteworthy precision if one has some intuition about the entanglement in the system.

The TEBD-LBO yields a better scaling than the original TEBD algorithm if $d_O \ll d$ and $D \gg 1$. In this case we gain an overall factor of D , i.e. we reduce the scaling from $\mathcal{O}(D^3 d^3)$ to $\mathcal{O}(D^2 d^3)$ as can be seen in table 2.1. As a first example Fig. 2.2 shows

2. Time-evolving block-decimation with local basis optimization

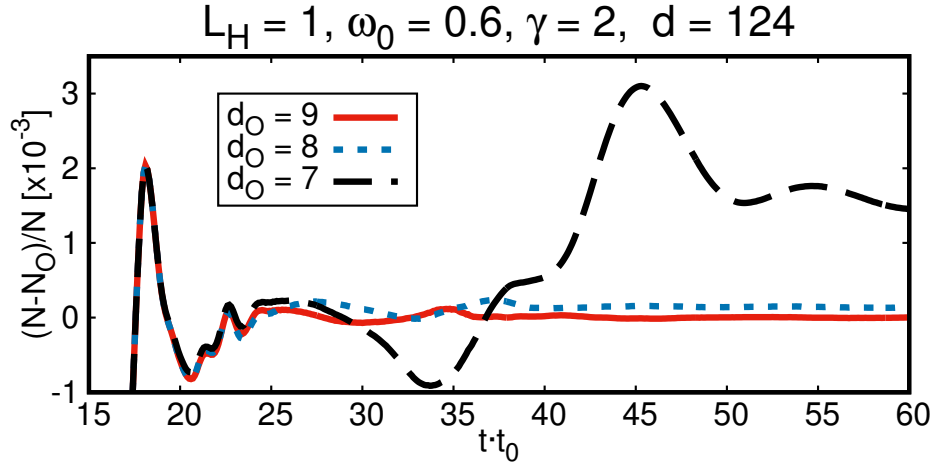


FIG. 2.2.: The relative error in the phonon number of TEBD-LBO with various optimal basis sizes and bare basis TEBD as reference for a large tight-binding lattice with one site coupled to Holstein phonons. The large errors for $t < 20$ arise from the fact that the total phonon number there is still smaller than the accuracy of the algorithm. For the red and blue curve we find no significant deviation from the bare basis results, although d_0 is an order of magnitude smaller than d .

that for the kind of system studied in Ch. 4 the difference in size between the optimal basis and the bare basis can be an order of magnitude, while both simulations show the same precision.

3. Relaxation of a highly excited electron in the Holstein model

The first application for the TEBD-LBO method is the relaxation of a highly excited electron by interaction with phonons in the one-dimensional Holstein model. The interaction of electrons and lattice vibrations (phonons) is a complex issue, which is studied for many decades. One interesting aspect is the polaron formation, that was first mentioned by Landau [39], where the presence of a valence electron causes a displacement of the neighboring ionic crystal particles from their equilibrium position, which induces a potential that binds the electron [40]. These phonon excitations will then follow the electron (if it escapes the potential) as it moves through the crystal and together they form a quasi-particle called the polaron. While keeping the polaron formation in mind, our main focus lies on the distinct dynamics of the electron and phonon degrees of freedom, respectively.

This investigation was a joint project with Florian Dorfner, Lev Vidmar and Fabian Heidrich-Meisner from the Ludwig-Maximilians-Universität München and some of the presented results were published in Ref. [27]. For our studies we use the Holstein model, where tight-binding electrons are linearly coupled to phonons with frequency ω_0 . The Holstein Hamiltonian [41] for open boundary conditions in second quantization reads

$$\begin{aligned} H &= H_{\text{kin}} + H_{\text{ph}} + H_{\text{coup}}, \\ &= -t_0 \sum_{j=1}^{L-1} (c_j^\dagger c_{j+1} + c_{j+1}^\dagger c_j) + \hbar\omega_0 \sum_{j=1}^L b_j^\dagger b_j - \gamma \sum_{j=1}^L (b_j^\dagger + b_j) n_j, \end{aligned} \quad (3.1)$$

where $c_j^\dagger(b_j^\dagger)$ and $c_j(b_j)$ are the creation and annihilation operators for spinless electrons (phonons) on lattice site j , respectively, and $n_j = c_j^\dagger c_j$ is the electron number operator. The hopping integral t_0 serves as the energy unit throughout this thesis and we use natural units, i.e. we set $\hbar = 1$, so that the phonon frequency ω_0 has also the dimension of an energy. The lattice sites are assumed to be equidistant with lattice constant $a = 1$. The strength of the interaction between electrons and phonons is given by the coupling constant γ , but in some cases it is more appropriate to use $g = \frac{\gamma}{\omega_0}$ or $\varepsilon_b = \frac{\gamma^2}{\omega_0}$ as the model parameter (see Sec. 3.1).

The electronic term H_{kin} describes a tight-binding model, which can be diagonalized analytically with a discrete Fourier transform for PBC's. Also for OBC's we get the result $H_{\text{kin}} = -2t_0 \sum_{n=1}^L \cos(k_n) d_{k_n}^\dagger d_{k_n}$ with $k_n = \frac{n\pi}{L+1}$, $n \in \{1, 2, \dots, L\}$ with a similar transformation [42] (see Sec. B). Thus the kinetic energy of an electron always lies in the band $-2t_0 < E_{\text{kin}} < 2t_0$. The single-particle eigenstate of H_{kin} with the highest eigenenergy is a convenient choice as the initial state of a time evolution which we

3. Relaxation of a highly excited electron in the Holstein model

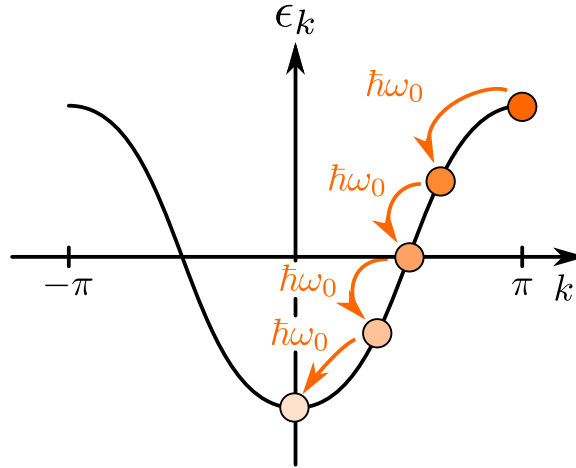


FIG. 3.1.: Sketch of the decay of a highly excited electron, caused by the interaction with phonons. The electron kinetic energy starts at the top of the tight-binding band and is then reduced every time a phonon gets excited. From Ref. [27].

use throughout this chapter if not otherwise specified. Therefore, we have

$$|\psi(t=0)\rangle = d_{k_L}^\dagger |\emptyset\rangle_e \otimes |\emptyset\rangle_p = \sqrt{\frac{2}{L+1}} \sum_{j=1}^L \sin\left(\frac{L}{L+1}\pi j\right) c_j^\dagger |\emptyset\rangle_e \otimes |\emptyset\rangle_p \quad (3.2)$$

with the maximal electronic kinetic energy $E_{\text{kin}}(t=0) = \langle \psi(t=0) | H_{\text{kin}} | \psi(t=0) \rangle = -2t_0 \cos\left(\frac{L}{L+1}\pi\right)$ and phonon vacuum $|\emptyset\rangle_p$. This state can be initialized with the scheme presented in Sec. 2.1 and is well suited for studying the energy transfer from a highly excited electron to phonons and possibly resulting relaxations [27]. A sketch of this process is shown in Fig. 3.1. Adding more electrons to the system would also yield interesting new results, but for the purpose of studying electron-phonon interaction one electron is sufficient. For an appropriate choice of the Hamiltonian parameters, also the local Hilbert space dimension can be large enough to have $d \gg d_0$, where the advantages of the TEBD-LBO method are apparent.

The Holstein model is very complex and the behaviour of the system can change greatly for different parameter regimes. Therefore, limiting cases are studied in the next sections and analytical results are given if possible to compare with the numerical outcomes. In Sec. 3.4 we study the crossover of the different parameter regimes. One example of this can be seen in Fig. 3.2, where the TEBD is checked against another numerical method, namely the diagonalization in a limited functional space (LFS) [43]. The perfect agreement of both methods can be considered as a strong argument for the accuracy of both methods even for long time simulations. This allows us to use TEBD results obtained with the bare basis as a reference for comparisons with TEBD-LBO results. However, the main results of [27] were obtained with the LFS method, as the local basis optimization was not fully operational at that time. The LFS is a very efficient method for these systems because it builds up the number

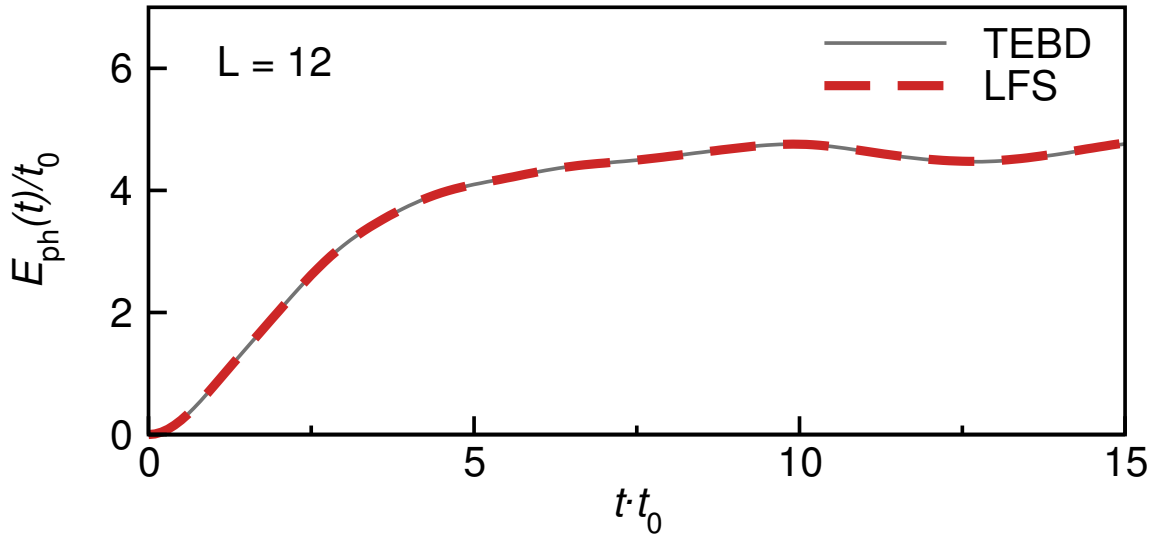


FIG. 3.2.: The phonon energy for $\gamma = \omega_0 = t_0$ calculated with the LFS method and TEBD without local basis optimization. Even for long times both algorithms show good agreement. From Ref. [27].

of states to the needed extent, depending on the Hamiltonian parameters, during the time evolution while maintaining the advantages of an ED method. The TEBD-LBO results presented in Sec. 3.4 are in good agreement with the LFS studies of Ref. [27] and show how to adapt them to open boundary conditions. Finally, in the last section of this chapter the weights of the optimal modes for ground states and time evolved states are analyzed.

3.1. Single-site system

The special case of a Holstein Hamiltonian for a lattice with just one site is exactly solvable by diagonalization, which brings the Hamiltonian into the form of a harmonic oscillator. For one lattice site there is no hopping term and the Hamiltonian is simply

$$H = \omega_0 b^\dagger b - \gamma(b^\dagger + b), \quad (3.3)$$

assuming one electron on the site. By introducing the operators

$$a = b - \frac{\gamma}{\omega_0}, \quad a^\dagger = b^\dagger - \frac{\gamma}{\omega_0} \quad (3.4)$$

we can rewrite the Hamiltonian as

$$H = \omega_0 a^\dagger a - \varepsilon_b, \quad (3.5)$$

with $\varepsilon_b = \frac{\gamma^2}{\omega_0}$. Thus the eigenenergies are $E_n = n\omega_0 - \varepsilon_b$, for $n \in \{0, 1, 2, \dots\}$. The ground state is defined by $a|0\rangle_a = 0$, where we use the subscript to distinguish the

3. Relaxation of a highly excited electron in the Holstein model

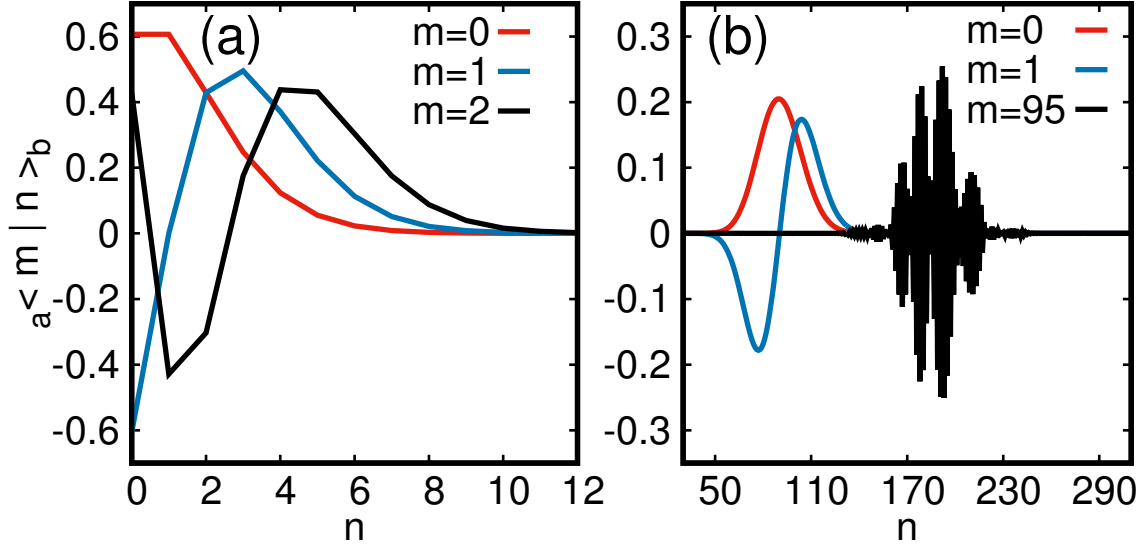


FIG. 3.3.: (a) The ground state and two lowest lying excited states for $\omega_0 = 10$ and $\gamma = 10$. (b) The ground state, first and ninety-fifth excited state for $\omega_0 = 0.2$ and $\gamma = 1.9$.

two different bases for the phonon system. The phonon number states are defined by $b^\dagger b |n\rangle_b = n |n\rangle_b$, whereas the Hamiltonian eigenstates fulfill $a^\dagger a |n\rangle_a = n |n\rangle_a$ for $n \in \{0, 1, 2, \dots\}$. To express the Hamiltonian ground state in the phonon number basis we insert the definitions (3.4) into the defining equation, which reads

$$a |0\rangle_a = (b - g) |0\rangle_a = 0, \quad (3.6)$$

with $g = \frac{\gamma}{\omega_0}$. This means the ground state of the Hamiltonian is the eigenstate of the phonon annihilation operator with eigenvalue g . Hence,

$$|0\rangle_a = e^{-\frac{g^2}{2}} e^{gb^\dagger} |0\rangle_b, \quad (3.7)$$

which is known as a coherent state. The excited states can be calculated by repeatedly acting with $(b^\dagger - g)$ on the ground state (3.7). Figure 3.3 shows some examples of eigenstates expressed in the phonon number basis for the anti-adiabatic and adiabatic strong-coupling regime.

The initial state for our numerical simulations is the tensor product of a highly excited electronic state and the phonon vacuum. In the single-site system the time evolution of this state is given by

$$|\psi(t)\rangle = e^{-it(\omega_0 a^\dagger a - \varepsilon_b)} |0\rangle_b = e^{-\frac{g^2}{2} + i\varepsilon_b t} \sum_{n=0}^{\infty} \frac{(-g)^n e^{-i\omega_0 t n}}{\sqrt{n!}} |n\rangle_a, \quad (3.8)$$

where we have inverted Eq. (3.7) to write the phonon vacuum state in the Hamiltonian eigenbasis

$$|0\rangle_b = e^{-\frac{g^2}{2}} e^{-ga^\dagger} |0\rangle_a = e^{-\frac{g^2}{2}} \sum_{n=0}^{\infty} \frac{(-g)^n}{\sqrt{n!}} |n\rangle_a. \quad (3.9)$$

With Eq. (3.8) we can easily compute time dependent expectation values such as the phonon energy $E_{\text{ph}}(t) = \omega_0 \langle \psi(t) | b^\dagger b | \psi(t) \rangle$. The phonon number operator is

$$b^\dagger b = a^\dagger a + g(a^\dagger + a) + g^2 \quad (3.10)$$

and by using the orthonormality relation for the Hamiltonian eigenstates ${}_a \langle m | n \rangle_a = \delta_{mn}$ one obtains

$$\begin{aligned} E_{\text{ph}}(t) &= \omega_0 e^{-g^2} \sum_{n,m=0}^{\infty} \frac{(-g)^{n+m} e^{-i\omega_0 t(n-m)}}{\sqrt{n!m!}} {}_a \langle m | a^\dagger a + g(a^\dagger + a) + g^2 | n \rangle_a \\ &= \gamma e^{-g^2} \left[\sum_{n=1}^{\infty} \frac{g^{-1} g^{2n}}{(n-1)!} + \sum_{n=0}^{\infty} \frac{(-g)^{2n+1} e^{i\omega_0 t}}{n!} + \sum_{n=1}^{\infty} \frac{(-g)^{2n-1} e^{-i\omega_0 t}}{(n-1)!} \right] + \varepsilon_b \quad (3.11) \\ &= \gamma e^{-g^2} \left[g e^{g^2} + (-g) e^{g^2} e^{-i\omega_0 t} + (-g) e^{g^2} e^{i\omega_0 t} \right] + \varepsilon_b \\ &= 2\varepsilon_b [1 - \cos(\omega_0 t)]. \end{aligned}$$

For other initial states $|\psi(0)\rangle = |n\rangle_b$ the phonon energy is just increased by $n\omega_0$. The results in this section can also be used as a zero order expansion for the anti-adiabatic limit $t_0 \ll \omega_0$. When there is no electron hopping, the system behaves like L uncoupled sites, each with a constant expectation value of the electron number operator.

3.2. Short-time dynamics

The dynamics for arbitrary chain lengths L are much more involved than for a single site. Nevertheless, we can estimate time-dependent expectation values for arbitrary L for short times $t\eta \ll 1$, where η is the largest of t_0, ω_0, γ , which are all of the same order of magnitude in the numerically most challenging cases. The expectation value $\langle \psi(t) | X | \psi(t) \rangle$ of the operator X can be expanded into a power series in t . We use the Baker-Campbell-Hausdorff formula in the Heisenberg picture to obtain

$$\begin{aligned} \langle \psi(t) | X | \psi(t) \rangle &= \langle e^{iHt} X e^{-iHt} \rangle = \left\langle \sum_{n=0}^{\infty} \frac{1}{n!} [iHt, X]_n \right\rangle \\ &= \langle X \rangle + it \langle [H, X] \rangle - \frac{t^2}{2} \langle [H, [H, X]] \rangle + \mathcal{O}(t^3), \end{aligned} \quad (3.12)$$

where $\langle \dots \rangle$ denotes the expectation value in the initial state. We study the energy transfer from the electron to the phononic degrees of freedom and, thus, we compute

3. Relaxation of a highly excited electron in the Holstein model

the expectation values (3.12) for X being H_{kin} , H_{ph} and H_{coup} , respectively. Starting with the kinetic energy, we compute the first order commutator

$$[H, H_{\text{kin}}] = [H_{\text{coup}}, H_{\text{kin}}] = \gamma \sum_{j=0}^{L-2} (b_j^\dagger + b_j - b_{j+1}^\dagger - b_{j+1})(c_j^\dagger c_{j+1} - \text{h.c.}). \quad (3.13)$$

This term has obviously a vanishing expectation value for an initial state that contains no phonons. Furthermore, we can neglect H_{kin} and H_{ph} for the second order commutator for the same reason, as both terms conserve the phonon number. Thus, only

$$[H_{\text{coup}}, [H_{\text{coup}}, H_{\text{kin}}]] = -\gamma^2 \sum_{j=0}^{L-2} (b_j^\dagger + b_j - b_{j+1}^\dagger - b_{j+1})^2 (c_j^\dagger c_{j+1} + \text{h.c.}) \quad (3.14)$$

yields a non-vanishing contribution to the expectation value. We conclude

$$\begin{aligned} E_{\text{kin}}(t) &= \langle H_{\text{kin}} \rangle - \frac{t^2}{2} \langle [H_{\text{coup}}, [H_{\text{coup}}, H_{\text{kin}}]] \rangle + \mathcal{O}(t^3) \\ &= E_{\text{kin}}(0) [1 - \gamma^2 t^2] + \mathcal{O}(t^3) \end{aligned} \quad (3.15)$$

as the short-time approximation for the kinetic energy. This means that at the beginning of the interaction the electron transfers energy to the phononic degrees of freedom if the kinetic energy is positive. For $E_{\text{kin}}(0) < 0$ the electron gains energy, although there are no phonons that could be absorbed, which means that the coupling energy has to fall off rapidly to compensate for the increases in both the kinetic and phonon energy. Right in the middle of the tight-binding band the kinetic energy vanishes and so does the leading term of its time derivative.

We repeat the above procedure for $X = H_{\text{ph}}$, where again the first order commutator

$$[H, H_{\text{ph}}] = [H_{\text{coup}}, H_{\text{ph}}] = -\gamma \omega_0 \sum_{j=0}^{L-1} c_j^\dagger c_j (b_j - b_j^\dagger) \quad (3.16)$$

and all second order terms except

$$[H_{\text{coup}}, [H_{\text{coup}}, H_{\text{ph}}]] = -2\gamma^2 \omega_0 \sum_{j=0}^{L-1} c_j^\dagger c_j \quad (3.17)$$

have vanishing expectation values and, thus, the phonon energy is

$$E_{\text{ph}}(t) = \omega_0 \gamma^2 t^2 + \mathcal{O}(t^3) \quad (3.18)$$

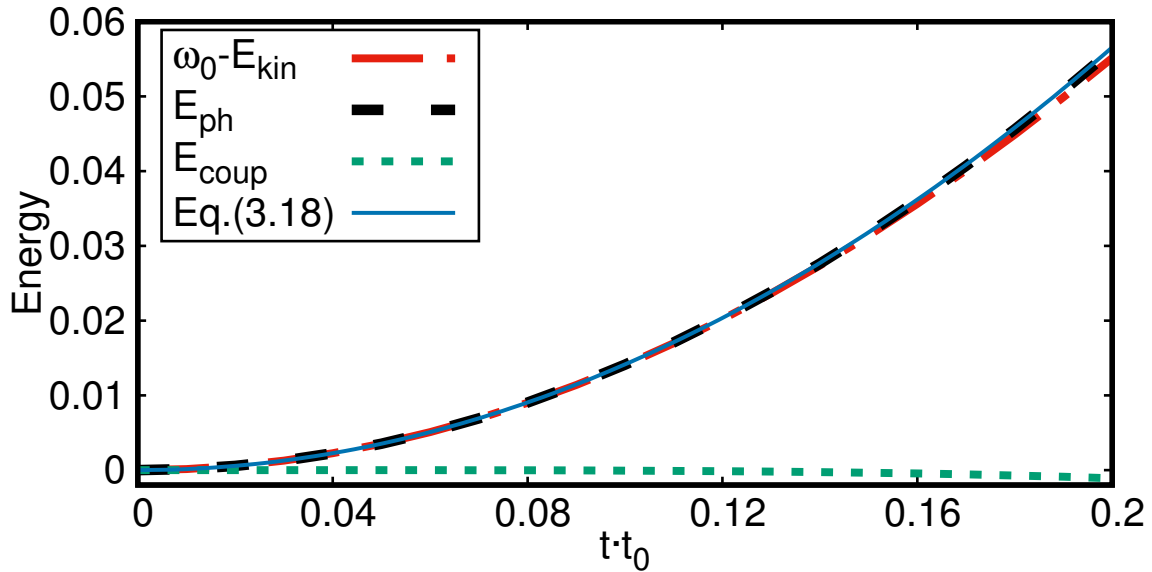


FIG. 3.4.: The energies on a small time scale calculated with TEBD-LBO compared to the analytic results of perturbation theory. On a chain of length $L = 7$ with $t_0 = \gamma = 1$ the electron is initially in an eigenstate with $E_{\text{kin}}(0) = \omega_0 = \sqrt{2}$.

with our choice of $|\psi(0)\rangle$. The coupling energy is completely determined by commutators, that we have already used above and can thus be written as

$$\begin{aligned} E_{\text{coup}}(t) &= -\frac{t^2}{2} \left\langle \left[H_{\text{coup}}, [H_{\text{kin}}, H_{\text{coup}}] \right] + \left[H_{\text{coup}}, [H_{\text{ph}}, H_{\text{coup}}] \right] \right\rangle \\ &= \left(E_{\text{kin}}(0) - \omega_0 \right) \gamma^2 t^2 + \mathcal{O}(t^3) \end{aligned} \quad (3.19)$$

without further calculations. Like the kinetic energy, this function can be either positive or negative depending on the phonon frequency ω_0 and the initial conditions. Also for $E_{\text{kin}}(0) = \omega_0$ the coupling energy is constantly zero in leading order, which corresponds to a direct energy transfer from the electron to the phonon system¹. This can be seen in Fig. 3.4, where the increase of $E_{\text{ph}}(t)$ and decrease of $E_{\text{kin}}(t)$ are orders of magnitude larger than the growth of the coupling energy.

The total energy $E(t) = E_{\text{kin}}(t) + E_{\text{ph}}(t) + E_{\text{coup}}(t) = E_{\text{kin}}(0)$ is conserved and the second order approximation of (3.11) coincides with (3.18), which means that these results are also consistent with the exact formula for the single-site system.

3.3. Perturbation theory

For limiting cases, where one parameter $\eta \in \{t_0, \omega_0, \gamma\}$ of the Holstein Hamiltonian is much smaller than the other two, we can use perturbation theory to get analytical

¹Since the phonon frequency ω_0 is always positive, $E_{\text{kin}}(0) = \omega_0$ can only hold for $E_{\text{kin}} > 0$, where the electronic energy decreases at the beginning of the interaction.

3. Relaxation of a highly excited electron in the Holstein model

results for the different energies in the system. The general scheme obtained in this section is applied to the case of the kinetic energy in the anti-adiabatic limit. The Hamiltonian may be written as $H = H_0 + \eta H_1$. If η is small enough it is convenient to expand the time evolution operator

$$U(t) = e^{-i(H_0 + \eta H_1)t} = U_0(t) + \eta U_1(t) + \eta^2 U_2(t) + \mathcal{O}(\eta^3) \quad (3.20)$$

in powers of η and determine U_0, U_1 and U_2 by taking the limit of infinitely many small time slices

$$\begin{aligned} e^{-i(H_0 + \eta H_1)t} &= \lim_{\tau \rightarrow 0} \prod_{m=1}^{t/\tau} e^{-i(H_0 + \eta H_1)\tau} = \lim_{\tau \rightarrow 0} \prod_{m=1}^{t/\tau} [1 - i(H_0 + \eta H_1)\tau] \\ &= \lim_{\tau \rightarrow 0} \prod_{m=1}^{t/\tau} [e^{-iH_0\tau} - i\eta H_1\tau]. \end{aligned} \quad (3.21)$$

Inserting Eq. (3.21) into the definition (3.20) and equating the coefficients, we can identify

$$U_0(t) = e^{-iH_0t}, \quad (3.22)$$

$$U_1(t) = -i \int_0^t dt_1 e^{-iH_0(t-t_1)} H_1 e^{-iH_0t_1}, \quad (3.23)$$

$$U_2(t) = - \int_0^t dt_1 \int_0^{t-t_1} dt_2 e^{-iH_0(t-t_1-t_2)} H_1 e^{-iH_0t_1} H_1 e^{-iH_0t_2}, \quad (3.24)$$

which yields the leading orders in η of the time evolution. The time-dependent expectation value $X(t)$ of an operator X is given by

$$\begin{aligned} X(t) &= \langle U_0^\dagger X U_0 \rangle + \eta \langle U_1^\dagger X U_0 + U_0^\dagger X U_1 \rangle \\ &\quad + \eta^2 \langle U_1^\dagger X U_1 + U_2^\dagger X U_0 + U_0^\dagger X U_2 \rangle + \mathcal{O}(\eta^3), \end{aligned} \quad (3.25)$$

where we have omitted the t for the time evolution operators and $\langle \dots \rangle$ is again the expectation value in the initial state. Of course X can also depend on η , as can be seen in the following example.

In the case of finite $t_0 \ll \omega_0, \gamma$ we can use the zeroth-order term of (3.25) to get the first-order result for the time evolution of the kinetic energy. Our initial state is again the tensor product of the phonon vacuum and an electronic eigenstate with eigenvalue $-2t_0 \cos(K)$. Thus the kinetic energy is

$$E_{\text{kin}}(t) = \langle \psi(0) | e^{iH_0t} H_{\text{kin}} e^{-iH_0t} | \psi(0) \rangle, \quad (3.26)$$

where $H_0 = H_{\text{ph}} + H_{\text{coup}}$ and the time evolution of the phononic degrees of freedom is given by Eq. (3.8). The term $e^{-iH_0t} | \psi(0) \rangle$ is a superposition of states with one completely localized electron and the single-site phonon state on the same site. The

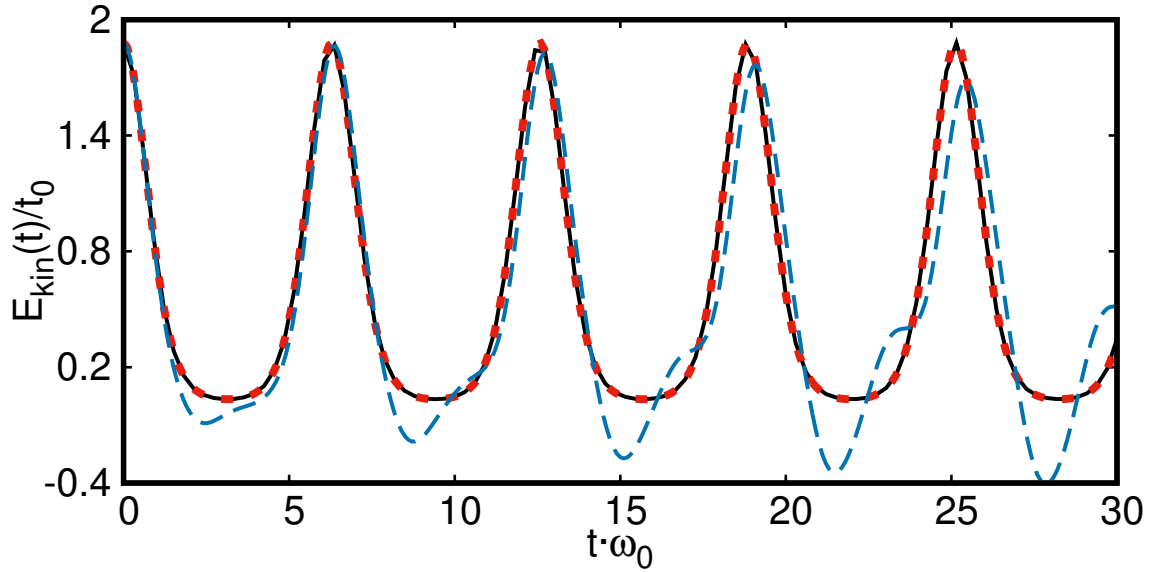


FIG. 3.5.: The kinetic energy calculated with TEBD-LBO compared to Eq. (3.29) (black solid). Both simulations were carried out with $L = 8$ and $\omega_0 = \gamma = 1$. While there is perfect agreement for $t_0 = 0.001$ (red dotted), we see only qualitatively the same behaviour for $t_0 = 0.05$ (blue dashed).

single electron hopping terms in H_{kin} separate the localized electrons from the time evolved phonon states. Therefore, the kinetic energy is given by

$$E_{\text{kin}}(t) = -2t_0 \cos(K) \left| {}_b\langle 0 | e^{-it(\omega_0 a^\dagger a - \varepsilon_b)} | 0 \rangle_b \right|^2, \quad (3.27)$$

where $-2t_0 \cos(K) = \langle \psi(0) | H_{\text{kin}} | \psi(0) \rangle$ is the initial kinetic energy. To evaluate the scalar product we have to write (3.8) in the boson number basis. By inserting (3.4) and (3.9) we get

$$\begin{aligned} e^{-it(\omega_0 a^\dagger a - \varepsilon_b)} | 0 \rangle_b &= e^{-\frac{1}{2}g^2 + it\varepsilon_b} e^{-g(t)a^\dagger} | 0 \rangle_a \\ &= e^{-\frac{g^2}{2} + it\varepsilon_b} e^{-g(t)(b^\dagger - g)} e^{-\frac{g^2}{2}} e^{gb^\dagger} | 0 \rangle_b \\ &= e^{-g[g-g(t)] + it\varepsilon_b} e^{[g-g(t)]b^\dagger} | 0 \rangle_b, \end{aligned} \quad (3.28)$$

with $g(t) = ge^{-i\omega_0 t}$. In this form the vacuum part of the state is easily identified and the kinetic energy can be concluded to

$$E_{\text{kin}}(t) = -2t_0 \cos(K) e^{-2g^2[1 - \cos(\omega_0 t)]}. \quad (3.29)$$

Figure 3.5 shows the good agreement of this formula with the TEBD results. Even for large times (in terms of the phonon frequency) the analytic first order approximation is very accurate if the hopping integral t_0 is three orders of magnitude smaller than the other energy scales. As can also be seen in Fig. 3.5, the validity of (3.29) is

3. Relaxation of a highly excited electron in the Holstein model

really restricted to this limit and $E_{\text{kin}}(t)$ is more involved in general. Other solutions of (3.25) can be obtained for periodic boundary conditions using momentum space, as done in [27].

3.4. Relaxation dynamics

Away from the limiting cases we observe smooth transitions between the different regimes. While in the anti-adiabatic regime the electron can only transfer a part of its energy for a finite time to phonons before reabsorbing it, the energy transfer becomes permanent in the adiabatic regime. Also from weak to strong coupling we find different energy transfers between the electron and phonon sector. In the crossover regimes the dynamics are composed of the individual cases.

To analyze the influence of the adiabaticity ratio $\frac{\omega_0}{t_0}$ it is convenient to choose intermediate e-p coupling, so that the dynamics are noticeably influenced by the e-p interaction but not dominated by strong coupling effects. Figure 3.6 shows how the time evolution of the electron kinetic energy changes with decreasing $\frac{\omega_0}{t_0}$ smoothly from oscillation dominated to relaxation dominated for different coupling strengths γ and chain lengths L . The reason for this crossover is that in the anti-adiabatic case the electronic excess energy is insufficient to create a phonon excitation, because $\omega_0 > 4t_0 \cos(k_L)$ and, therefore, the dynamics are dominated by the single-site e-p interaction, while in the adiabatic case phonons can be created permanently. The

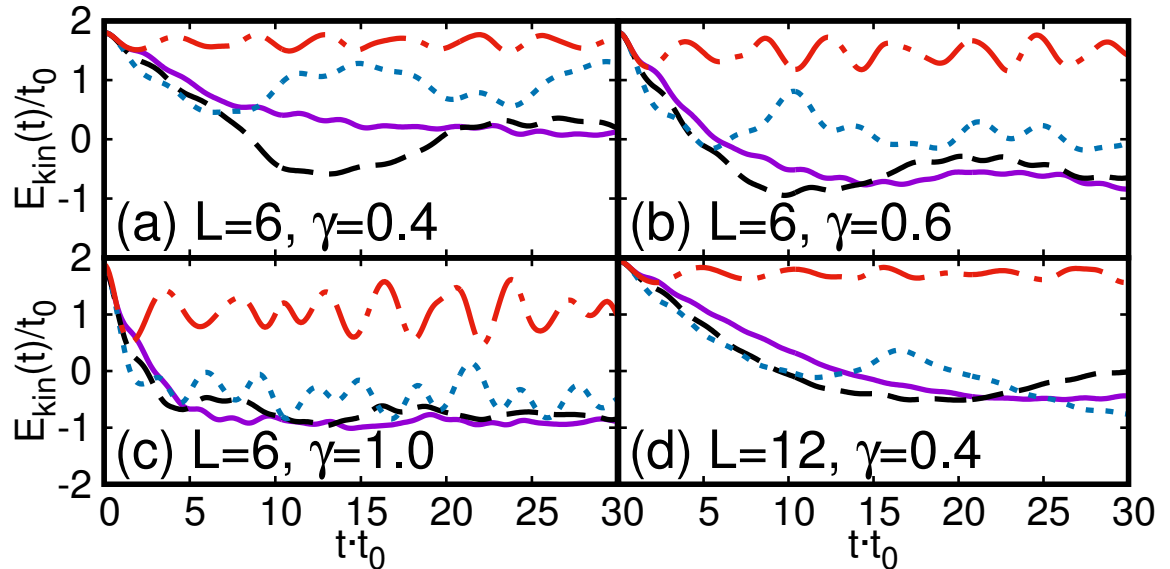


FIG. 3.6.: The electron kinetic energy as a function of time calculated with TEBD-LBO is shown for different chain lengths and coupling strengths. The phonon frequencies are $\omega_0 = 1.0$ (purple solid), $\omega_0 = 1.5$ (black dashed), $\omega_0 = 2.0$ (blue dotted), $\omega_0 = 5.0$ (red dashed-dotted).

time $t = \tau_{\text{rel}}$ of the first local minimum of the kinetic energy can be viewed as the relaxation time. During this period energy is transferred from the electron to the phononic degrees of freedom, while afterwards there is no net energy transfer averaged over long times. This is called the steady state regime. The relaxation time increases for decreasing $\frac{\omega_0}{t_0}$, which is partly due to the greater loss of kinetic energy and as Fig. 3.6 implies, also because the kinetic energy falls off more rapidly in the anti-adiabatic case. Furthermore the relaxation time increases with the number lattice sites (compare Fig. 3.6(a) and (d)), but decreases with the coupling strength (compare Fig. 3.6(a), (b) and (c)).

A similar crossover can be found for the phonon energy. In Fig. 3.7 the time evolution of $\frac{E_{\text{ph}}}{\gamma}$ is shown for the same system parameters as the kinetic energy in Fig. 3.6. For given ω_0 the maximal phonon energy is mainly determined by the coupling strength γ , which is why all curves in Fig. 3.7 that correspond to the same phonon frequency and system length L have similar height. The time evolution mirrors that of the kinetic energy qualitatively, but the oscillation amplitudes in the steady state regime are larger, because there is still an exchange between phonon and coupling energy. However in the adiabatic regime these amplitudes are small compared to the mean phonon energy of the steady state. In [27] it was shown that for stronger coupling the phonon and coupling energy oscillate with a higher amplitude in the stationary regime, but in Fig. 3.7(c) one can see that some amplitudes are smaller, in relation to the mean value, than for weaker coupling. These results are, however, not contradicting, because what is studied here is not the strong coupling

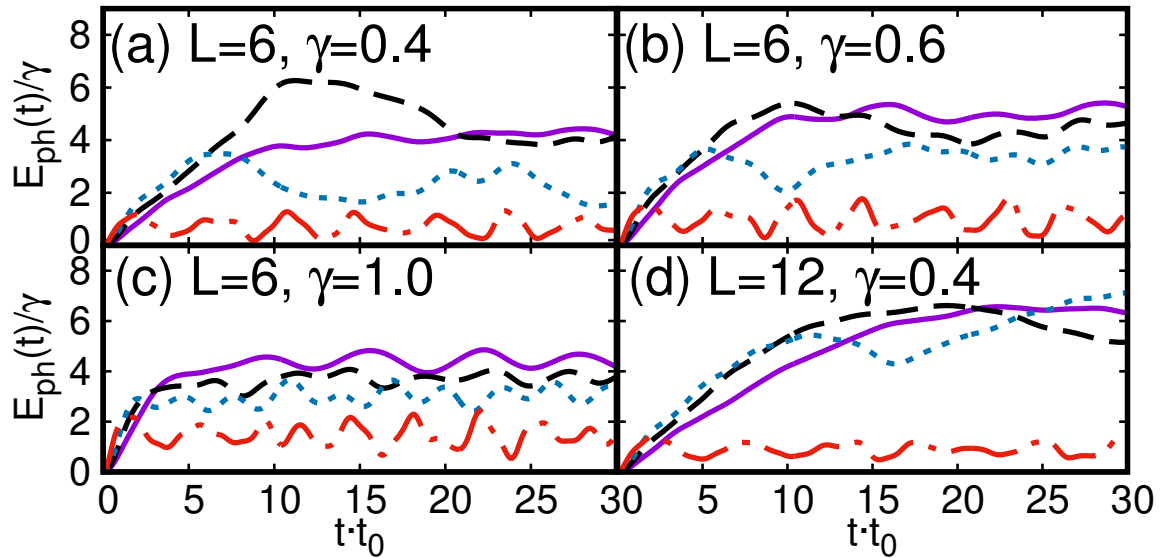


FIG. 3.7.: The phonon energy divided by the respective coupling γ as a function of time calculated with TEBD-LBO is shown for the same system parameters as in Fig. 3.6. The phonon frequencies are $\omega_0 = 1.0$ (purple solid), $\omega_0 = 1.5$ (black dashed), $\omega_0 = 2.0$ (blue dotted), $\omega_0 = 5.0$ (red dashed-dotted).

3. Relaxation of a highly excited electron in the Holstein model

regime in the sense of $\lambda > 1$. The largest γ appearing in Fig. 3.7 is $\gamma = 1.0$, which corresponds to $\lambda = 0.5$, i.e. the weakest coupling considered in the crossover study in [27]. The results of Fig. 3.6 and Fig. 3.7 show that weak e-p coupling can also lead to larger oscillation amplitudes in the steady state regime, when the adiabaticity ratio $\frac{\omega_0}{t_0}$ is too large for a full relaxation ($\omega_0 > t_0$ in our case).

The time unit is \hbar/t_0 , which depends on the material. To compare the relaxation time scale to time-resolved spectroscopy experiments we can assume $t_0 \approx 0.3$ eV as used in Ref. [44] as a typical value for cuprates. This leads to $\hbar/t_0 \approx 2.2$ fs and relaxation times $15 \text{ fs} < \tau_{\text{rel}} < 45 \text{ fs}$, which is comparable to measured time scales of relaxation experiments [44, 45, 46].

3.5. Optimal modes

The TEBD-LBO algorithm outperforms the TEBD with bare basis only if $d_0 \ll d$, but this is not true in general. For many of the above calculations we find relations like $d \approx 2d_0$. As a matter of fact the optimal basis is not as effective for time evolution algorithms as it is for ground state methods. The reason is that the entanglement entropy, which is usually small for ground states and also for our initial states, can grow rapidly with time, depending on the parameters. Figure 3.8 compares the weights of the optimal modes for time evolved states and ground states for the same set of parameters. Although the weights are decaying exponentially in all cases (at least for a great part of the spectrum), the decay is much slower for the time evolved state. This means a much larger number of optimal modes is needed for a good

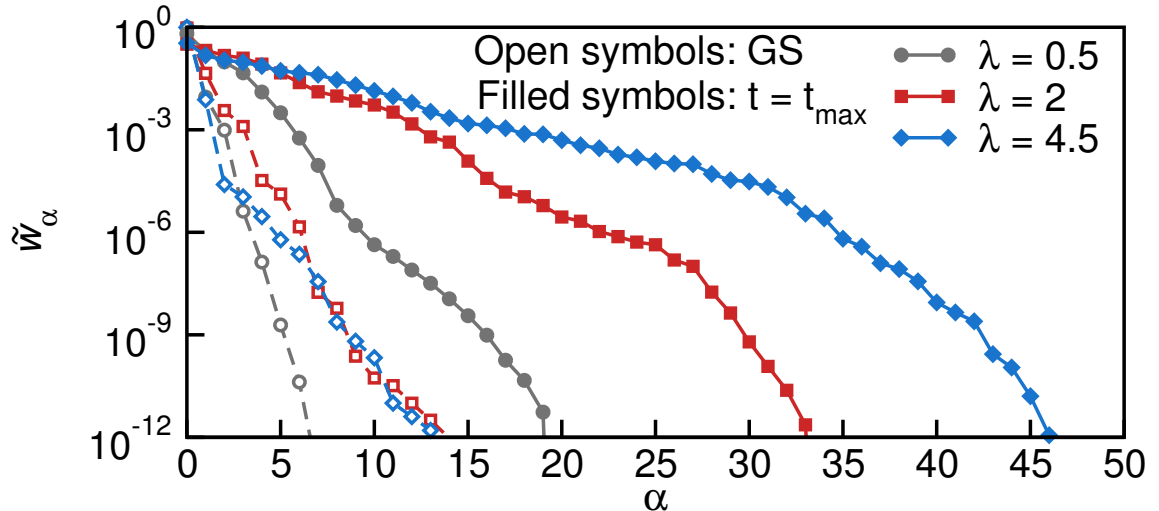


FIG. 3.8.: Comparison of the weights \tilde{w}_α , where α numbers the optimal states, of ground state calculations and time evolution. These results were obtained by Florian Dorfner with LFS for $\omega_0 = t_0$ and $L = 12$ for $\lambda = 0.5$ and $L = 8$ for $\lambda = 2, 4.5$. The weights from the time evolution are taken where the phonon energy has its first local maximum in the stationary regime. From Ref. [27].

approximation of the state. This effect is not unexpected and should not be taken as an argument against the TEBD-LBO but rather as a guideline to find systems where the optimal basis is much more efficient than the bare basis. An interesting example is discussed in the next chapter and a general discussion of the performance is given in Ch. 5.

The optimal modes can not only be used to speed up numerical simulations, but also to gain insight into the physics of the system. In the next chapter the results from Sec. 3.1 can be used to explain transmission resonances of an electronic wave packet which gets scattered by an e-p coupled structure.

4. Scattering of an electronic wave packet by a one-dimensional electron-phonon-coupled structure

In this chapter we investigate how an electronic wave packet with Gaussian shape is scattered by an impurity with electron-phonon (e-p) interaction within the Holstein model. Most of these results were published in Ref. [28] and Ref. [33]. In contrast to the last chapter we now consider the case of a tripartite one-dimensional lattice. A small e-p coupled structure of L_H sites in the middle of the lattice with two non-interacting tight-binding leads of length $L_{TB} \gg L_H$ attached at both sides. The Hamiltonian for the whole lattice reads

$$H = -t_0 \sum_{j=1}^{L-1} (c_j^\dagger c_{j+1} + c_{j+1}^\dagger c_j) + \sum_{j=L_{TB}+1}^{L_{TB}+L_H} [\hbar\omega_0 b_j^\dagger b_j - \gamma (b_j^\dagger + b_j) n_j], \quad (4.1)$$

with $L = L_H + 2L_{TB}$ and otherwise the same notation as in the last chapter. The length of L_H varies between a single-site (impurity) and up to 100 sites (wire). Unlike in previous studies [47, 48] we do not insert the electronic wave packet directly into the e-p coupled structure. Instead it is inserted in the left lead in the form of a Gaussian distribution with momentum towards the e-p coupled structure. Depending on the system parameters the wave packet can be scattered into several smaller, transmitted or reflected, wave packets with various velocities. One example of this setup and resulting electron density distributions for later times are shown in Fig.4.1. The initial state

$$|\psi(t=0)\rangle = \sum_{j=1}^L \psi_j c_j^\dagger |\emptyset\rangle_e \otimes |\emptyset\rangle_p, \quad (4.2)$$

is the tensor product of the phonon vacuum and the electronic wave function

$$\psi_j = \sqrt{\frac{a}{\sigma\sqrt{2\pi}}} e^{-\frac{a^2(j-j_0)^2}{4\sigma^2} + iKja}, \quad (4.3)$$

which is a Gaussian wave packet with width σ , mean value j_0 and momentum K . The variance $\sigma^2 = 25a^2$, which is much larger than the lattice constant a , provides a stable wave packet even for long simulations. The initial center of the electronic wave packet is always at $j_0 = L_{TB} - 10\frac{\sigma}{a}$, which is in the left lead with a sufficient distance to the e-p coupled structure. The momentum is chosen as $K = \frac{\pi}{2a}$, such that the initial velocity $v \approx 2\frac{t_0 a}{\hbar} \sin(Ka)$ takes its maximal value $v_{\max} \approx 2\frac{a}{\hbar/t_0}$. The total energy is

$$E = E_{\text{kin}}(t) + E_{\text{ph}}(t) + E_{\text{coup}}(t) = E_{\text{kin}}(0) = -2t_0 \cos(Ka) \approx 0, \quad (4.4)$$

4. Scattering of an electronic wave packet by a one-dimensional electron-phonon-coupled structure

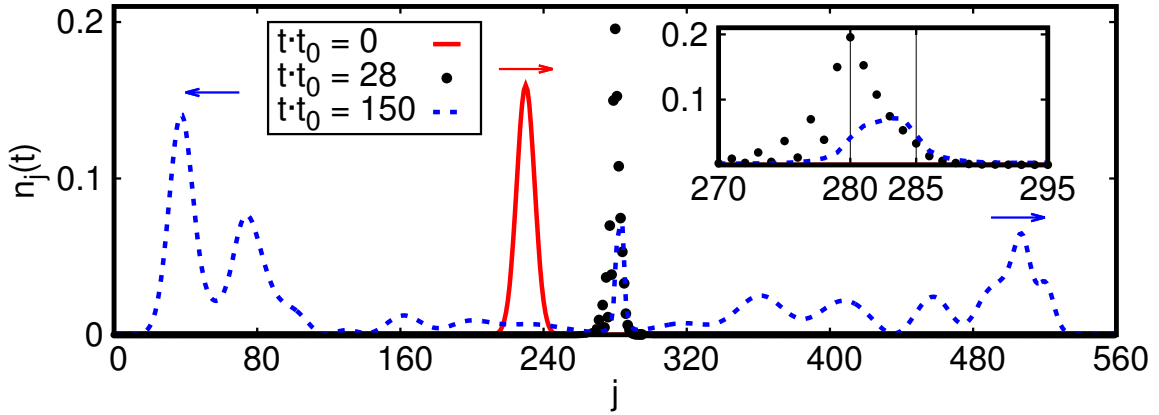


FIG. 4.1.: The electronic density distribution calculated with TEBD-LBO for a 6-site e-p coupled wire with phonon frequency $\omega_0 = 2.25t_0/\hbar$ and electron-phonon coupling $\gamma = t_0$ at three instances of time: before (red solid line), during (black dots), and after (blue dashed line) the main scattering processes. The index $1 \leq j \leq L = 560$ numbers the lattice sites. The red solid and blue dashed curves are multiplied by factors 2 and 10, respectively. The inset shows an enlarged view of the region around the e-p coupled wire. Thin vertical lines show the position of the first and last e-p coupled sites. From Ref. [28].

which corresponds to the middle of the electronic tight-binding band $-2t_0 \leq E \leq 2t_0$. All of these initial values were used for all numerical simulations presented in this chapter. They provide a fast moving and stable initial wave packet.

For the simulations in this chapter we have used up to $d = 2 * 386$ bare boson states and $d_O = 21$ optimal states, while using a cutoff of 10^{-13} for the eigenvalues of the single-site reduced matrices, which guarantees precise results at the cost of sometimes unnecessarily large optimal bases. For the case of one e-p coupled impurity site, there is always only one optimal boson state for the occupied impurity, because the tight-binding leads are in the vacuum state. Also the bond dimension fulfills $D \approx d_O$ after the electron has left the impurity. For simulations with more than one e-p coupled site bond dimensions up to $D = 84$ were reached with a cutoff of 10^{-15} for the eigenvalues of the bipartite reduced density matrices. The bond dimension of the initial state 4.2 is $D = 2$. We know from the last chapter that the ratio $g = \gamma/(\hbar\omega_0)$ and the length of the chain L_H ¹ are the crucial parameters for the computational time of a simulation. While they naturally determine the number d of bare boson states and the number of sites with large local Hilbert space, respectively, they both also influence the amount of bipartite entanglement in the system and thus the bond dimension D . Therefore, we are limited to a few e-p coupled sites ($L_H \leq 6$) for general couplings or the weak-coupling regime for long e-p coupled structures. The total number of sites $180 \leq L \leq 580$ and the maximal time $60\hbar/t_0 \leq t_{\max} \leq 150\hbar/t_0$ are chosen such that the electronic density on the e-p coupled structure is negligibly

¹Note that the length L_{TB} of the tight-binding leads is irrelevant for the computational time of the simulation, because the updates for non-interacting sites take an amount of time negligible compared to the time for interacting sites.

small at $t = t_{\max}$ and neither the reflected nor the transmitted waves are influenced by the outer edges of the tight-binding leads. The required memory is below 2 Gb, and therefore negligible, in all simulations presented in this chapter but the CPU time is a real limiting factor as it goes up to 150 hours for a single simulation in the most demanding regime.

We investigate time dependent expectation values such as the phonon energy $E_{\text{ph}}(t)$ and the electronic density distribution $n_j(t) = \langle \psi(t) | n_j | \psi(t) \rangle$ as well as asymptotic expectation values like the transmission coefficient and dissipated energy, i.e. energy that is permanently transferred from the electron to the phonon system. The parameters which vary throughout the next sections are (i) the length of the e-p coupled structure L_H . We provide an extensive analysis of the special case of a single impurity, including an analytically solvable scattering theory that correctly reproduces all asymptotic expectation values. Additionally, results for wire lengths up to $L_H = 100$ are discussed. (ii) The phonon frequency ω_0 varies from the adiabatic ($\hbar\omega_0 \ll t_0$) to the anti-adiabatic ($\hbar\omega_0 \gg t_0$) regime. In the latter case, the phonon system reacts instantaneously to the presence of the electron. For small enough frequencies permanent energy transfer from the electron to the phonon system, dissipation, can occur. With the chosen parameters the frequency has to fulfill $\hbar\omega_0 \lesssim 2t_0$, so that the initial electronic kinetic energy is greater than the energy of one phonon. (iii) The e-p coupling γ is the last system parameter to investigate. We look at the asymptotic expectation values as functions of γ for specific L_H and ω_0 . We find resonance conditions with sharp peaks in the anti-adiabatic regime, which blur with decreasing phonon frequency and vanish in the adiabatic limit.

In the remainder of this chapter we use the energy scale $t_0 = 1$, lattice spacing $a = 1$ and $\hbar = 1$. Therefore, the time unit is again $\frac{\hbar}{t_0} = 1$, but we write $t \cdot t_0$ at the time axes in the the figures as a reminder. We give a detailed description of the scattering theory for a single e-p coupled site in Sec. 4.1 and the method to generalize this theory to incident Gaussian wave packets is presented in Sec. 4.2. The results of the numerical simulations are discussed in Sec. 4.3 for the transmission and reflection coefficients, in Sec. 4.4 for the dissipated energy, and in Sec. 4.5 for the transient self-trapping of the electron on the e-p coupled structure.

4.1. Scattering theory

In the case of a single-site impurity it is possible to gain analytical results by the use of scattering theory. From the stationary scattering states we obtain the asymptotic expectation values, which should coincide with our TEBD results if the following conditions hold: (i) $L_{\text{TB}} - j_0, j_0 \gg \sigma$. The initial position of the wave packet should be sufficiently far away from the e-p coupled structure and the outer edge of the left tight-binding lead. (ii) $\sigma > \pi/K$. The width has to be large enough to provide a wave packet that resembles a Gaussian distribution (in real space) with negligible dispersion. (iii) $n_j(t_{\max}) \ll 1, \forall j \in \{L_{\text{TB}} + 1, \dots, L_{\text{TB}} + L_H\}$. The probability that the electron is still on the e-p coupled structure has to vanish before the final expectation

4. Scattering of an electronic wave packet by a one-dimensional electron-phonon-coupled structure

values are measured.

We want to solve the time-independent Schrödinger equation for the Hamiltonian (4.1) with $L_H = 1$. We shift the lattice site index such that the e-p coupled impurity corresponds to $j = 0$ and $j \in \{-L/2, \dots, L/2\}$. The stationary scattering state can be written as

$$|\psi\rangle_S = \sum_{j,n} \psi(j,n) |j\rangle_e \otimes |n\rangle_p, \quad (4.5)$$

with $n = 0, 1, \dots, \infty$ being the (bare) phonon mode index. Inserting (4.5) into the time-independent Schrödinger equation $E|\psi\rangle = H|\psi\rangle$ we obtain

$$\text{for } |j| \geq 1: \quad E\psi(j,n) = n\omega_0\psi(j,n) - t_0\psi(j-1,n) - t_0\psi(j+1,n) \quad (4.6)$$

and

$$\text{for } j = 0: \quad E\psi(0,n) = n\omega_0\psi(0,n) - t_0\psi(-1,n) - t_0\psi(1,n) \\ - \gamma\sqrt{n}\psi(0,n-1) - \gamma\sqrt{n+1}\psi(0,n+1). \quad (4.7)$$

For an incident plane wave coming from the left with wave number $\pi > K > 0$ and no initial phonon excitations the stationary scattering state can be written as

$$\psi(j,n) = \begin{cases} Ae^{iKj}\delta_{n0} + B_n e^{-ik_n j}, & j \leq 0 \\ C_n e^{ik_n j}, & j \geq 0, \end{cases} \quad (4.8)$$

with $k_0 = K$. The amplitudes B_n and C_n correspond to the reflected and transmitted plane waves for a given phonon number n . Energy conservation implies

$$E = -2t_0 \cos(K) = n\omega_0 - 2t_0 \cos(k_n), \quad (4.9)$$

which can be inverted to obtain the wave numbers

$$k_n = \begin{cases} \arccos\left(\frac{n\omega_0 - E}{2t_0}\right), & n < n_B \\ i \operatorname{arccosh}\left(\frac{n\omega_0 - E}{2t_0}\right), & n \geq n_B, \end{cases} \quad (4.10)$$

where n_B is defined as the smallest number n for which $n\omega_0 > 2t_0[1 - \cos(K)]$. Outgoing scattering states exist only for $n_B > n \geq 0$ while states with $n \geq n_B$ are bound around the impurity. Using the uniqueness of the wave function at $j = 0$ we get the conditions

$$\begin{aligned} A + B_0 &= C_0 \\ B_n &= C_n, \quad \forall n \geq 1. \end{aligned} \quad (4.11)$$

This means that the amplitudes for reflected and transmitted plane waves are equal for a given number of phonon excitations $n \geq 1$. This result is also supported by the

TEBD-LBO simulations for the Gaussian wave packet. Using (4.8) in (4.7) we obtain

$$E(A + B_0) = -t_0(Ae^{-ik_0} + B_0e^{ik_0}) - t_0C_0e^{ik_0} - \gamma C_1, \quad \text{for } n = 0 \quad (4.12)$$

$$\begin{aligned} E C_1 &= n\omega_0 C_n - t_0 C_n e^{ik_n} \\ &\quad - t_0 B_n e^{ik_n} - \gamma\sqrt{n}C_{n-1} - \gamma\sqrt{n+1}C_{n+1}, \quad \text{for } n \geq 1 \end{aligned} \quad (4.13)$$

where we can substitute E and B_n with (4.9) and (4.11), respectively, to get an infinite system of recursive linear equations

$$0 = 2it_0(C_0 - A)\sin(k_0) + \gamma C_1 \quad (4.14)$$

$$0 = 2it_0 C_n \sin(k_n) + \gamma\sqrt{n}C_{n-1} + \gamma\sqrt{n+1}C_{n+1}, \quad (4.15)$$

which can be solved recursively using a computer algebra system, e.g. *Mathematica*. The normalization of the quantum state requires $C_n \rightarrow 0$ for $n \rightarrow \infty$, which we implement by choosing a cutoff n_c with an exponentially small value for C_{n_c} and $C_n = 0$ for all $n > n_c$. If n_c is large enough, the solution neither depends on n_c nor the choice of C_{n_c} . With this we can calculate stationary properties like the transmission coefficient

$$T(K) = \sum_{n=0}^{n_B-1} \frac{v_n}{v_0} \left| \frac{C_n}{A} \right|^2 = \sum_{n=0}^{n_B-1} \frac{\sin(k_n)}{\sin(k_0)} \left| \frac{C_n}{A} \right|^2, \quad (4.16)$$

where $v_n = 2t_0 \sin(k_n)$ is the velocity of a wave packet with wave number k_n , which corresponds to an electron that has excited n phonons permanently, and $K = k_0$ is the incident wave number.

In the anti-adiabatic limit $\omega_0 \gg t_0$ the large phonon energy implies $n_B = 1$, hence the transmission coefficient is just $T(K) = \left| \frac{C_0}{A} \right|^2$. In this case an analytical solution for the transmission coefficient can be found for an electronic energy

$$E = E_m = -\varepsilon_b + m\omega_0, \quad (4.17)$$

that coincides with an eigenenergy of the single-site Holstein model. In the anti-adiabatic limit equation (4.10) can be rearranged to get

$$2t_0 \sin(k_0) = \sqrt{4t_0 - E_m^2} \quad (4.18)$$

$$2it_0 \sin(k_n) = -\sqrt{(E_m - n\omega_0)^2 - 4t_0^2} \approx -n\omega_0 + E_m, \quad \forall n \geq 1. \quad (4.19)$$

With this the equation system (4.14) and (4.15) reduces to

$$0 = i\sqrt{4t_0^2 - E_m^2}(C_0 - A) + \gamma C_1 \quad (4.20)$$

$$0 = (E_m - n\omega_0)C_n + \gamma\sqrt{n}C_{n-1} + \gamma\sqrt{n+1}C_{n+1}, \quad \forall n \geq 1, \quad (4.21)$$

where we identify Eq. (4.21) as the eigenvalue equation of the shifted harmonic oscillator in Sec. 3.1 with the difference that $n \geq 1$. If we follow this analogy and

4. Scattering of an electronic wave packet by a one-dimensional electron-phonon-coupled structure

assume this equation also to hold for $n = 0$, i.e. $0 = E_m C_0 + \gamma C_1$, and insert this into Eq. (4.20), we get

$$0 = i\sqrt{4t_0^2 - E_m^2} \left(\frac{C_0}{A} - 1 \right) - E_m \frac{C_0}{A} \Leftrightarrow \frac{C_0}{A} = \frac{1}{1 - \frac{E_m}{i\sqrt{4t_0^2 - E_m^2}}}, \quad (4.22)$$

which implies

$$T(K) = \left| \frac{C_0}{A} \right|^2 = \frac{4t_0^2 - E_m^2}{4t_0^2}. \quad (4.23)$$

This corresponds to a high transmission rate, because our incident wave packet is centered around $E = 0$. The energy E_m is also the eigenenergy of the e-p coupled site occupied by an electron and disconnected from the leads. For this reason we call (4.17) the resonance condition.

4.2. Wave packet averaging

The results of the last section, such as equation (4.16), are valid for a plane wave with a sharp wave number K . The initial state of our numerical simulations is an electronic wave packet with a Gaussian distribution of finite width in Fourier space. With a discrete Fourier transform of (4.3) we get

$$\mathcal{F}[\psi](k) = \sqrt{\sigma \sqrt{\frac{2}{\pi}}} e^{-\sigma^2(k-K)^2 - i j_0(k-K)}, \quad (4.24)$$

where the prefactor is chosen so that $\mathcal{F}[\psi](k - K)$ is normalized if we treat k as a continuous variable. This is justified by the fact that we consider the limit of infinitely long tight-binding leads $L \rightarrow \infty$. The distribution (4.24) provides the weights to properly average results like (4.16) for comparison with our TEBD-LBO simulations. Although we consider it as a continuous variable we cannot integrate over k , since $T(k)$ has to be calculated through the costly solution of the equation system for every k . Therefore, we approximate the integral by a Riemann sum

$$T^{\text{av}}(K) = \Delta k \sum_m |\mathcal{F}[\psi](m \Delta k)|^2 T(m \Delta k), \quad (4.25)$$

with intervals of length $\Delta k = \frac{\pi}{2} \cdot 10^{-2}$. The number and size of steps are chosen such that

$$\Delta k \sum_{m=-30}^{30} |\mathcal{F}[\psi](m \Delta k)|^2 = 1 - \mathcal{O}(10^{-6}), \quad (4.26)$$

which is sufficient for a very good agreement with TEBD results for different parameter regimes, as can be seen in the next sections.

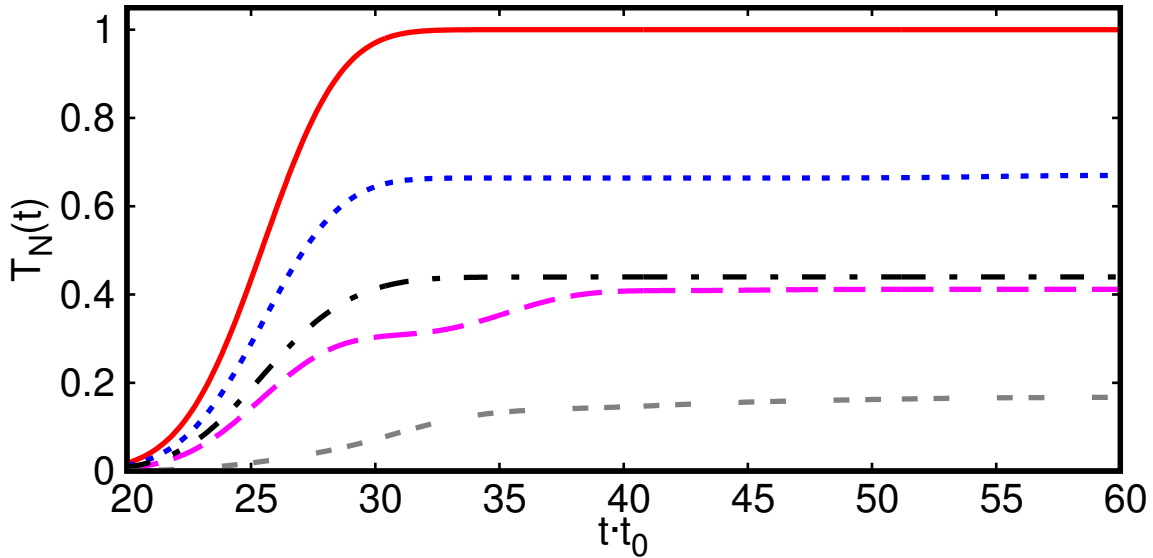


FIG. 4.2.: Time evolution of the numerical transmission coefficient (4.27) calculated with TEBD-LBO for various cases: free particle (red solid line), e-p coupled impurity ($L_H = 1$) in the adiabatic strong-coupling regime with $\omega_0 = 0.2$ and $\gamma = 1.9$ (blue dotted line) as well as with $\omega_0 = 0.6$ and $\gamma = 3.9$ (purple dashed line), and e-p coupled structure in the intermediate regime ($\omega_0 = 1.6$ and $\gamma = 1.85$) with one site (black dashed-dotted line) and three sites (grey double-dashed line), respectively. The center of the wave packet reaches the first e-p coupled site at time $t \approx (L_{TB} - j_0)/v \approx 25$ in all cases. From Ref. [28].

4.3. Transmission

One expectation value that we can determine both within the scattering theory and in the TEBD-LBO simulations is the transmission probability of the electron. In this section we discuss our results for this quantity for all parameter regimes. For our TEBD-LBO simulations of Gaussian wave packets we define the transmission coefficient as the asymptotic value of the total electronic density in the right lead

$$T_N(t) = \sum_{j > L_{TB} + L_H} n_j(t). \quad (4.27)$$

Figure 4.2 shows how $T_N(t)$ converges in different parameter regimes. The expectation values at the maximal time $t = t_{\max}$, when the simulation ends, e.g. $t_{\max} = 60$ in Fig 4.2, are taken as the asymptotic results. At the maximal time, if it is well chosen, the probability to find the electron on an e-p coupled site is negligible small, hence the electronic densities both on the left and the right lead have converged. Therefore, we define the transmission coefficient for a TEBD-LBO simulation of a Gaussian wave packet as the value $T = T_N(t_{\max})$ at the maximal time t_{\max} . The wave packet starts $L_{TB} - j_0 = 50$ sites left of the e-p coupled structure with a velocity $v = v_{\max} = 2$ so that we do not expect any noticeable interaction or transmission before $t = (L_{TB} - j_0 - 4\sigma)/v \approx 15$. In the case of a free wave packet ($\gamma = 0$) $T_N(t)$

4. Scattering of an electronic wave packet by a one-dimensional electron-phonon-coupled structure

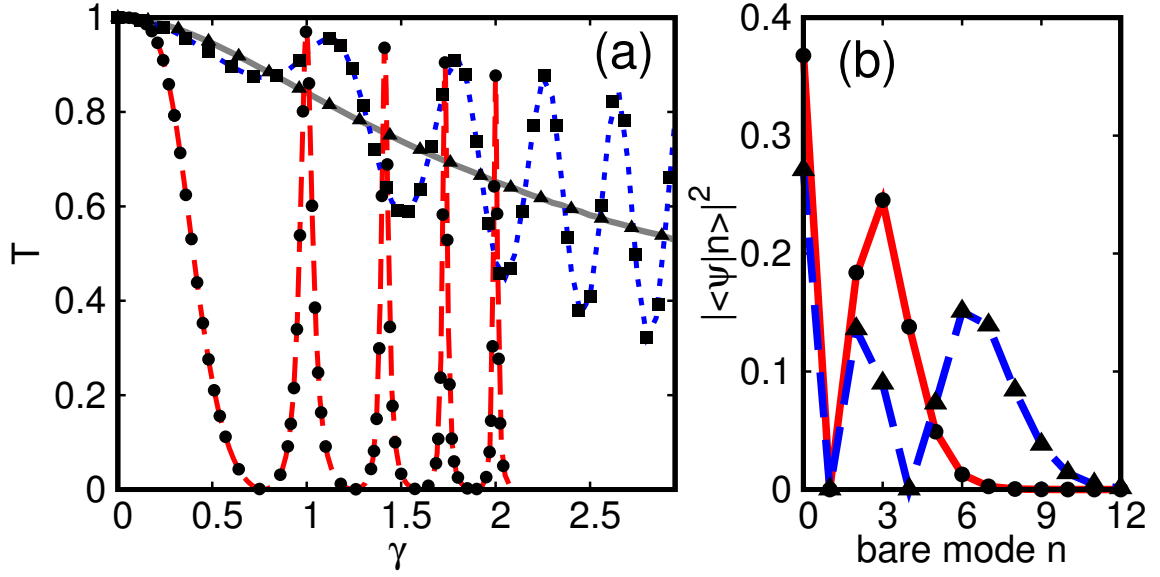


FIG. 4.3.: (a) Transmission coefficients calculated using TEBD-LBO (lines) and with scattering theory and wave packet averaging (symbols) for an e-p coupled impurity ($L_H = 1$). Results are plotted as a function of the electron-phonon coupling γ for the adiabatic regime $\omega_0 = 0.4$ (grey solid line and triangles), the intermediate regime $\omega_0 = 1.35$ (blue dotted line and squares), and the anti-adiabatic regime $\omega_0 = 10$ (red dashed line and dots). For $\omega_0 = 10$, γ is divided by a factor 10. (b) Components $|\langle \psi | n \rangle|^2$ of the occupied-site optimal mode $|\psi\rangle$ in the bare boson basis $|n\rangle$ calculated with TEBD-LBO for $\omega_0 = 10$ and $\gamma = \omega_0$ (red solid line) as well as $\gamma = \sqrt{2}\omega_0$ (blue dashed line). Also shown are the first (circles) and second (triangles) excited states of the single-site Holstein model occupied by one electron. From Ref. [28].

converges at $t = (L_{\text{TB}} - j_0 + 4\sigma)/v \approx 35$ for a single e-p coupled impurity site. For longer e-p coupled structures this time is extended by $t_+ = L_H/v$ but for interacting systems we can only estimate the maximal time needed with the help of empirical knowledge.

In Fig.4.3(a) we compare the transmission coefficients from the TEBD-LBO simulations with those obtained using the scattering theory and wave packet averaging for an e-p coupled impurity. The results are in perfect agreement in all parameter regimes, which verifies again the accuracy of our TEBD-LBO method and also shows that the transmission coefficients (4.25) and (4.27) are well defined. We see sharp maxima and minima of the transmission coefficient as a function of the e-p coupling strength γ in the anti-adiabatic regime in Fig. 4.3(a). Their positions agree with the resonance condition (4.17), i.e. $\gamma = \sqrt{m}\omega_0$ with $m = 0, 1, \dots, \infty$, because $E = 0$ is the average energy of the incident electron in our simulations.

In agreement with our considerations for the anti-adiabatic limit, we find that the optimal mode for the occupied impurity is practically constant during the simulation of the scattering process in this regime. As we have argued, only one eigenvalue of the single-site reduced density matrix has a finite weight for the impurity occupied by the

electron. In the case of transmission resonances the optimal mode for the occupied impurity coincides with an eigenstate of the single-site Holstein model. We know from Sec. 3.1 that the eigenenergies of the single-site Holstein model are $E_m = m\omega_0 - \varepsilon_b$ and Fig. 4.3(b) shows that the respective eigenstates are indeed the ones with energy $E_m = 0$. For the first and second peak, at $\gamma = \omega_0$ and $\gamma = \sqrt{2}\omega_0$, respectively, the quasi-stationary modes are essentially the first and second excited state of the single-site Holstein model with the same phonon frequency and e-p coupling strength. We can formulate this as a general result for a single e-p coupled impurity site in the anti-adiabatic regime: for the transmission resonance at $\gamma = \sqrt{m}\omega_0$ the optimal mode for the occupied impurity coincides with the eigenstate $|m\rangle_a$ of the single-site Holstein model with $H|m\rangle_a = E_m|m\rangle_a$ and $E_m = m\omega_0 - \gamma^2/\omega_0 = 0 = E_{\text{kin}}(t=0)$.

The high transmission rate at these couplings can be explained as follows. During the passage of the electron, the impurity changes between the no-electron eigenstate and the one-electron eigenstate with the same energy and in the anti-adiabatic regime the phonon degrees of freedom react almost instantaneously to the presence of the electron. This causes a resonant tunneling as indicated at the end of Sec. 4.1. This is also true for larger structures $L_H > 1$.

For smaller phonon frequencies, we find smaller oscillations of the transmission coefficient as a function of the e-p coupling strength, with vanishing amplitude in the adiabatic limit, as shown in Fig.4.3(a). As the phonons do no longer react instantaneously to the presence of the electron, the optimal mode for the occupied impurity is no longer (quasi-)stationary, but evolves in time, although it may still approach an eigenstate of the single-site Holstein model for a finite period. Furthermore, dissipation is possible for smaller phonon frequencies and Eq. (4.11) implies that a scattered electron, that has transferred a part of its energy to the phonon system, is transmitted and reflected with equal probability.

Figure. 4.4(a) shows the transmission coefficient in the anti-adiabatic regime for different lengths of the e-p coupled structure. We find the same resonances for all values of L_H . Around the peak at $\omega_0 = \gamma = 10$ the transmission coefficients in the figure are slightly too small, because the probability that the electron is still trapped on the e-p coupled structure at $t = t_{\text{max}}$ is increasing with L_H . Nevertheless, this error is smaller than $2 \cdot 10^{-2}$. The self-trapping time of the electron for such multi-site e-p coupled structures is investigated in Sec. 4.5. The transmission coefficient is decreasing with increasing wire lengths L_H , as one would expect², for a great part of the shown e-p couplings γ , but, interestingly, in the weak coupling regime $\gamma < \frac{\omega_0}{2}$ this is not the case. We cannot explain why the transmission coefficient can have a maximum for some $L_H > 1$ for some couplings.

The optimal modes are more involved for $L_H > 1$ than for a single impurity site. The single-site reduced density matrix has more than one eigenstate with a finite weight for an occupied e-p coupled site, since the remaining lattice is not necessarily in the vacuum state. Hence, even in the anti-adiabatic limit the phonon state can vary

²The fraction of the electronic wave packet that is transmitted through the first site of the e-p coupled wire can be reflected by the next one and so forth.

4. Scattering of an electronic wave packet by a one-dimensional electron-phonon-coupled structure

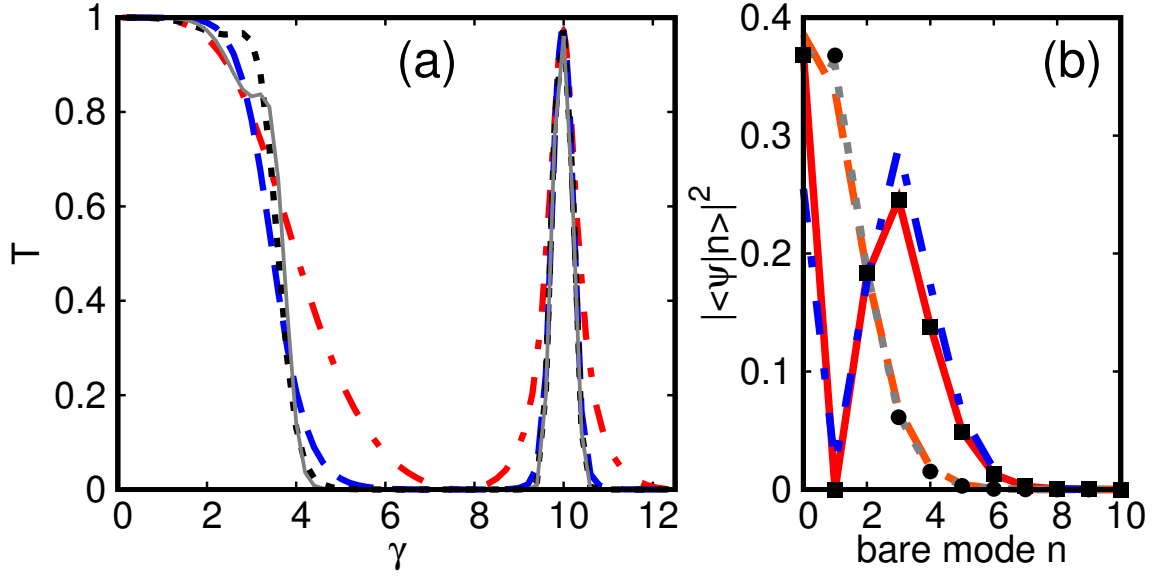


FIG. 4.4.: (a) Transmission coefficients calculated with TEBD-LBO in the anti-adiabatic regime ($\omega_0 = 10$) as a function of the electron-phonon coupling γ for several e-p coupled wire lengths: $L_H = 1$ (red dashed-dotted line), $L_H = 2$ (blue dashed line), $L_H = 3$ (black dotted line) and $L_H = 4$ (grey solid line). (b) Components $|\langle \psi | n \rangle|^2$ of the two most important optimal modes $|\psi\rangle$ for a site occupied by an electron in the bare boson basis $|n\rangle$ calculated with TEBD-LBO for $L_H = 2$ and $\omega_0 = \gamma = 10$ at two points in time: First (red solid line) and second (orange dashed line) optimal modes at $t = 25$ and first (gray dotted line) and second (blue dashed-dotted line) optimal modes at $t = 75$. Also shown are the ground state (circles) and first excited state (squares) of the single-site Holstein model occupied by one electron. From Ref. [28].

significantly with time, because the relative weights of the optimal modes may change. This can be seen in Fig. 4.4(b) where we show the most important phonon states for a two-site e-p coupled structure with $\omega_0 = \gamma = 10$. Around $t \approx 25$, where the center of the electronic wave packet arrives at the e-p coupled structure, the optimal modes with the highest weights are the first excited state of the single-site Holstein model for an occupied site and the phonon vacuum for an empty site, respectively. This is analogous to the case of a single impurity. There is, however, a difference arising from the emergence of the additional optimal modes. With a small but finite probability the electron gets trapped on the e-p coupled structure for a large time $t > 150$. In this long period, when the scattering process is mostly completed, both e-p coupled sites are in another phonon state. The highest weight for an occupied e-p coupled site has the ground state of the single-site Holstein model, while for an empty site the bare mode with one phonon has the second highest weight³. These two states together fulfill the condition $E_{\text{GS}} + E_1 = 0$. Therefore, we can explain why the transmission resonances have the same positions in the anti-adiabatic regime and which optimal

³The optimal mode with the highest weight for an empty site is the phonon vacuum, because at this time the electron is with a high probability far away from the e-p coupled structure.

modes are the most relevant. However, we cannot predict the time evolution of their weights or the transmission maxima and minima outside the anti-adiabatic regime.

Although we see in Fig. 4.4(a) that the transmission does not decrease systematically with increasing wire length L_H in every regime, we can expect this behaviour in the weak-coupling adiabatic regime, where the phonon system reacts very slowly to the presence of the electron. Assuming that the phonon state does not deviate significantly from the vacuum state during the scattering, the transmission coefficient for an e-p coupled structure with $L_H > 1$ can be calculated as a series of independent single-site scattering processes. The reflection coefficient for an e-p coupled impurity $R(L_H = 1) = 1 - T(L_H = 1)$ can be obtained either with a TEBD-LBO simulation or with scattering theory. Hence, we express the reflection coefficient $R(L_H)$ for an e-p coupled wire of length L_H in terms of $R(1)$. As a first step we deduce the formula for $L_H = 2$. The electron can be either reflected directly by the first e-p coupled site or it is transmitted in and out of the structure through the first e-p coupled site with an odd number of reflections in the intervening time

$$R(2) = R(1) + T(1)^2 \sum_{n=0}^{\infty} R(1)^{2n+1} = R(1) + T(1)^2 R(1) \sum_{n=0}^{\infty} [R(1)^2]^n. \quad (4.28)$$

Since $|R(1)^2| < 1$ for all parameters, the geometric series converges. The reflection coefficient for $L_H = 2$ is then

$$R(2) = R(1) + \frac{[1 - R(1)]^2 R(1)}{1 - R(1)^2} = \frac{2R(1)}{1 + R(1)}, \quad (4.29)$$

where we have used $T(1) = 1 - R(1)$. The same can be done for an e-p coupled structure with $L_H = 3$ by considering the first two sites as one big site with reflection given by (4.29) and by iteration it is possible to determine $R(L_H)$ for arbitrary wire length L_H . The closed formula

$$R(L_H) = \frac{L_H R(1)}{1 + (L_H - 1)R(1)} \quad (4.30)$$

can be proven by induction. As the induction basis one can use either $L_H = 1$, which is trivial, or $L_H = 2$, what was already proven in (4.29). To conclude the proof we have to show that (4.30) holds for $L_H + 1$ assuming that it holds for L_H . Considering that the $2n + 1$ reflections within the structure are composed of n reflections on the

4. Scattering of an electronic wave packet by a one-dimensional electron-phonon-coupled structure

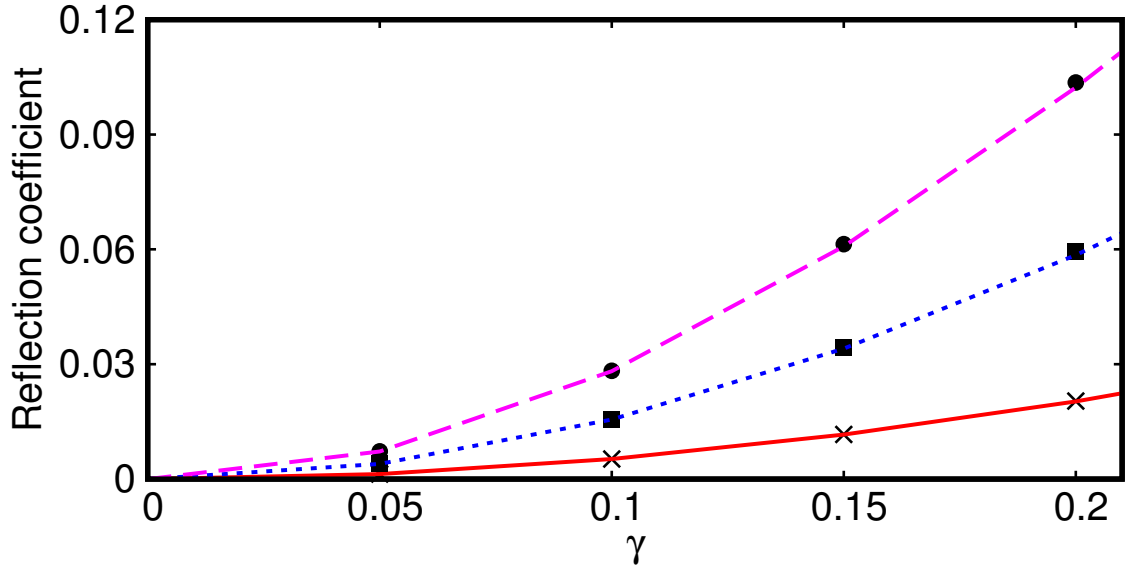


FIG. 4.5.: Reflection coefficient $R(L_H)$ calculated with TEBD-LBO as a function of the electron-phonon coupling γ in the weak-coupling adiabatic regime ($\omega_0 = 0.6$) for e-p coupled wires of length $L_H = 2$ (crosses), $L_H = 6$ (squares), and $L_H = 11$ (circles). The lines show the predictions of scattering theory for an e-p coupled impurity combined with Eq. (4.30) for $R(2)$ (red solid line), $R(6)$ (blue dotted line), and $R(11)$ (purple dashed line). From Ref. [28].

composite big site on the left and $n + 1$ reflections on the right site, we get

$$\begin{aligned}
 R(L_H + 1) &= R(L_H) + [1 - R(L_H)]^2 R(1) \sum_{n=0}^{\infty} [R(1) R(L_H)]^n \\
 &= \frac{R(1) + R(L_H) [1 - 2R(1)]}{1 - R(1) R(L_H)} \\
 &= \frac{R(1) [1 + (L_H - 1)R(1)] + [1 - 2R(1)] L_H R(1)}{1 + (L_H - 1)R(1) - L_H R(1)^2} \\
 &= \frac{(L_H + 1)R(1)}{1 + L_H R(1)}. \quad \square
 \end{aligned} \tag{4.31}$$

Figure 4.5 shows good agreement of (4.30) and TEBD-LBO simulations for wire lengths up to $L_H = 11$. During the derivation of (4.30) we have used that the single-site reflection is constant, but (4.25) holds only for the vacuum as the initial phonon state. Therefore, we clearly need weak coupling and a slow reaction of the phonon system to the presence of the electron, so that the phonon states of the e-p coupled sites do not change significantly during the scattering process.

In the case of large e-p coupled structures $L_H \gg 1$ the transmission coefficient

$$T(L_H) = 1 - R(L_H) = \frac{1 - R(1)}{1 + (L_H - 1)R(1)} = \frac{T(1)}{L_H[1 - T(1)] + T(1)} \quad (4.32)$$

is inversely proportional to the length of the e-p coupled wire. In particular (4.32) is strictly monotonically decreasing with increasing L_H for all $0 < T(1) < 1$ and $L_H \geq 0$ and, therefore, the surprising maxima of the transmission coefficient for e-p coupled structure lengths $L_H > 1$ for some couplings in Fig. 4.4(a) cannot be explain with the above considerations. This illustrates that weak-coupling is not sufficient for (4.30) because we have $g \approx \frac{3}{10}$ in the relevant part of Fig. 4.4(a) whereas $g \lesssim \frac{1}{3}$ in Fig. 4.5.

Outside the adiabatic weak-coupling or anti-adiabatic regime the TEBD-LBO simulations become very costly for multi-side e-p coupled structures. Both the bond dimension D and number of optimal modes d_O are larger for, otherwise, equal system parameters. Due to the existence of more than one site with large local Hilbert space the block entanglement, and therefore D , can be much higher. In particular D is no longer upper bounded by d_O . The number of optimal modes required for an e-p coupled site is larger solely from the fact that the remaining lattice is not necessarily in the vacuum state as it was in the impurity case. Additionally, the electron can be trapped on the e-p coupled structure for a much longer (see Sec. 4.5). For these reasons the discussion of the transmission coefficient is restricted to $L_H = 1$, weak-coupling or the anti-adiabatic regime. Although not enough for a comprehensive study, we have some results for $L_H > 1$ that suggest a behaviour of the transmission as a function of γ , which is similar to that in the impurity case, in all parameter regimes.

4.4. Dissipation

The total energy (4.4) is a constant of motion, which is given by the initial electronic excess energy. After the scattering process the electron is again far away from the e-p coupled structure (see Sec. 4.5), so that the e-p interaction energy vanishes and no energy can be transferred from the electron to the phononic degrees of freedom or vice versa. We define the dissipated energy E_D as the loss of kinetic energy or equivalently as the gain of phonon energy at $t = t_{\max}$. The time evolution of the phonon energy

$$E_{\text{ph}}(t) = \omega_0 \sum_j \langle \psi(t) | b_j^\dagger b_j | \psi(t) \rangle \quad (4.33)$$

is illustrated in Fig. 4.6. We see that the time when (4.33) converges depends strongly on the system parameters, but this is obviously the same time that the total electronic density on the right lead (4.27) converges and, therefore, our simulation time is chosen sufficiently large. For a single e-p coupled impurity site the phonon energy has a maximal value that increases monotonically with the coupling strength γ for a given frequency ω_0 . The dissipated energy, however, has no such monotonic behavior. As

4. Scattering of an electronic wave packet by a one-dimensional electron-phonon-coupled structure

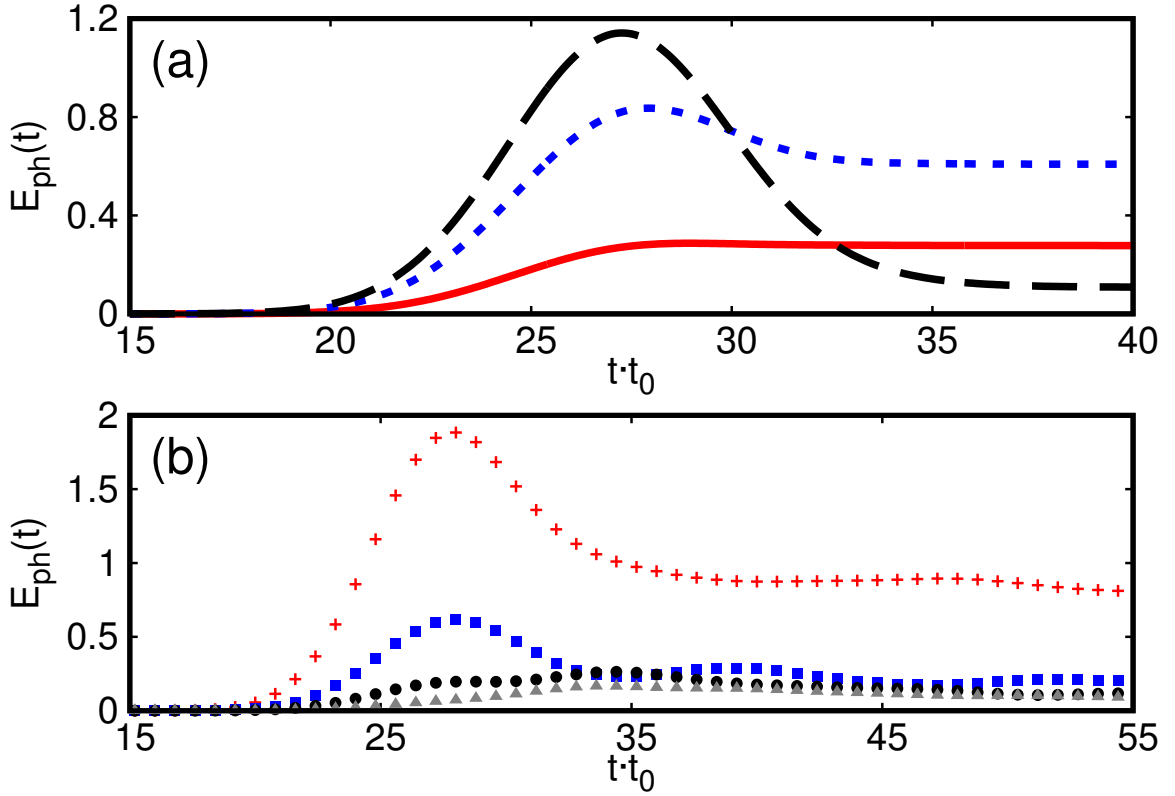


FIG. 4.6.: Phonon energy calculated with TEBD-LBO as a function of time. (a) For an e-p coupled impurity with $\omega_0 = 1.35$ and three electron-phonon couplings $\gamma = 0.8$ (red solid line), $\gamma = 1.45$ (blue dotted line), and $\gamma = 1.8$ (black dashed line). (b) For a four-site e-p coupled structure in the intermediate regime ($\omega_0 = 1.6$, $\gamma = 1.85$) the phonon energies are shown separately for the first (red crosses), second (blue squares), third (black bullets), and fourth (gray triangles) site. From Ref. [28].

can be seen in Fig. 4.6(a) the phonon energy may retain its maximal value or drops down to a, possibly, much lower value.

For e-p coupled structures with $L_H > 1$ the phonon energy can evolve completely differently on every site, as shown in Fig. 4.6(b). Due to the reflections inside the e-p coupled structure the phonon energy $E_{\text{ph}}(t)$ can have several local maxima. In this example the phonon energy is much higher on the first site compared to the rest of the wire, because a part of the electron is already reflected at the first site and the part of the electronic wave packet, which is transmitted through the first site, has already transferred some of its energy to the phonon system. Therefore, it is less likely to observe a permanent energy transfer on the other e-p coupled sites. The total amount of dissipated energy is upper bounded by the initial excess energy of the electron, which means $E_D < 2$ in our TEBD-LBO simulations. Each phonon has an excitation energy ω_0 , hence there is no dissipation for phonon frequencies $\omega_0 \gtrsim 2$. In these cases phonons can be excited transiently, but they are reabsorbed before the electronic wave packet leaves the e-p coupled structure. We see in Fig. 4.6 that the percentage of phonons, which are only transiently excited, varies greatly for systems

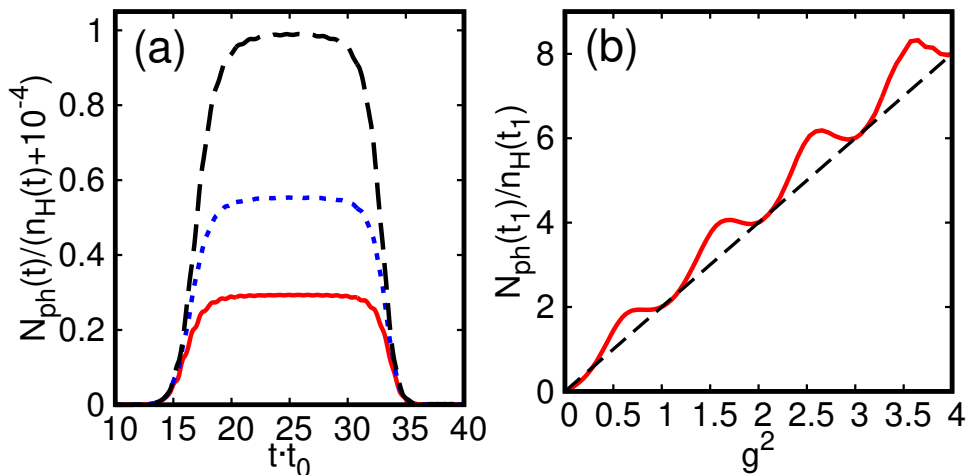


FIG. 4.7.: The phonon energy divided by the electronic density on the impurity n_H for a wave packet with $L_H = 1$ and $\omega_0 = 10$. (a) The normalized phonon number with a small offset for the electron density as a function of time for $\gamma = 4.3$ (red solid line), $\gamma = 5.3$ (blue dotted line) and $\gamma = 6.3$ (black dashed line). (b) The normalized phonon number at $t_1 = 25$, i.e. in the middle of the scattering process, as a function of g^2 (red solid line) compared to the mean phonon number $2g^2$ (black dashed line) for the single-site Holstein model.

with dissipation.

There are two effects that mainly determine the time evolution of the phonon energy during the scattering process. The phononic degrees of freedom of an occupied site evolve in time according to (3.11) as for the single-site Holstein model, which is thoroughly discussed in Sec. 3.1. These results were obtained for a site with $n = \langle c^\dagger c \rangle = 1$, but during a scattering process the amount of occupation of an e-p coupled site changes and this also directly affects the phonon energy. This can be illustrated in the case of phonon frequencies ω_0 that are large compared to the hopping integral t_0 , where the phonon state of an e-p coupled impurity is nearly constant during the passage of an electronic wave packet. In Fig. 4.7(a) we divide the phonon number by the electronic density on the impurity and find a smeared step function for this normalized phonon number as a function of time. We have added the small value 10^{-4} to the electronic density to avoid freakish behavior caused by the division of two values smaller than the numerical error. Figure 4.7(b) shows that the height of the steps, i.e. the constant value the normalized phonon number attains during the scattering process, is increasing as a function of g^2 with an oscillation with increasing amplitude. The mean phonon number $2g^2$ of the single-site Holstein model with one electron serves as an approximate lower boundary, where the normalized phonon number attains this value when the resonance condition $g^2 = m$, $m \in \mathbb{N}$ is fulfilled. This effect shows how the dynamics of the electron influence the phononic degrees of freedom.

One effect of the inverse kind can only be seen in the adiabatic regime, where the

4. Scattering of an electronic wave packet by a one-dimensional electron-phonon-coupled structure

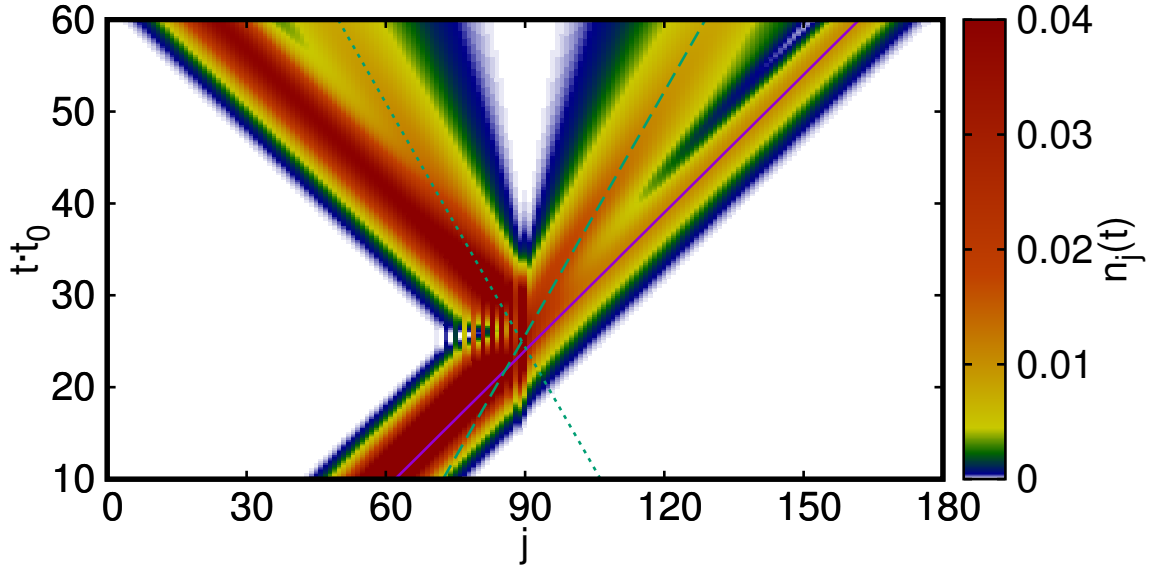


FIG. 4.8.: TEBD-LBO results for the electronic density $n_j(t)$ as a function of lattice site j and time for an e-p coupled impurity ($L_H = 1$) at $j = 90$ with e-p coupling $\gamma = 2.5$ and phonon frequency $\omega_0 = 1.65$. The thin lines illustrate the theoretically calculated velocities $v_0 = 2 \sin(k_0)$ (purple solid) and $v_1 = \pm 2 \sin(k_1)$ (green dashed and dotted).

energy of one phonon is smaller than the electronic excess energy, which means that dissipation is possible. When phonons are excited permanently in a scattering event the velocities of the corresponding partial wave packets are reduced. Figure 4.8 shows how the electronic density evolves in time with a clear splitting into transmitted and reflected part at the e-p coupled structure. Both partial wave packets get further divided into a part with the same absolute velocity as the initial wave packet and another part with velocity $v_1 = \pm 2 \sin(k_1)$, which is in accordance with the picture of an inelastic scattering process, where one phonon with frequency ω_0 remains excited on the e-p coupled structure. Energy conservation (4.9) implies that the asymptotic electron kinetic energy is given by $\lim_{t \rightarrow \infty} E_{\text{kin}}(t) = -2 \cos(k_n)$ for $n < n_B$ permanently excited phonons. This leads to group velocities $v_n = \pm 2 \sin(k_n)$ for the corresponding partial wave packets. The results illustrated in Fig. 4.8 also support the implication of Eq. (4.11) that in case of energy dissipation the electron gets transmitted and reflected with equal probability. How much energy gets dissipated for a certain set of parameters is, however, a sophisticated issue.

To understand this non-monotonic behavior of the dissipated energy, we examine the case of a single-site e-p coupled impurity. Figure 4.9 shows the dissipated energy as a function of the e-p coupling γ for different frequencies. We see similar oscillations with vanishing amplitude in the adiabatic limit as for the transmission coefficient. Within the scattering theory we have computed the coefficients C_n of the electronic state, where n states the number of phononic excitations. We have argued that only a finite number of these coefficients contributes to the transmission and reflection, while the rest corresponds to bound states, which would violate energy conservation

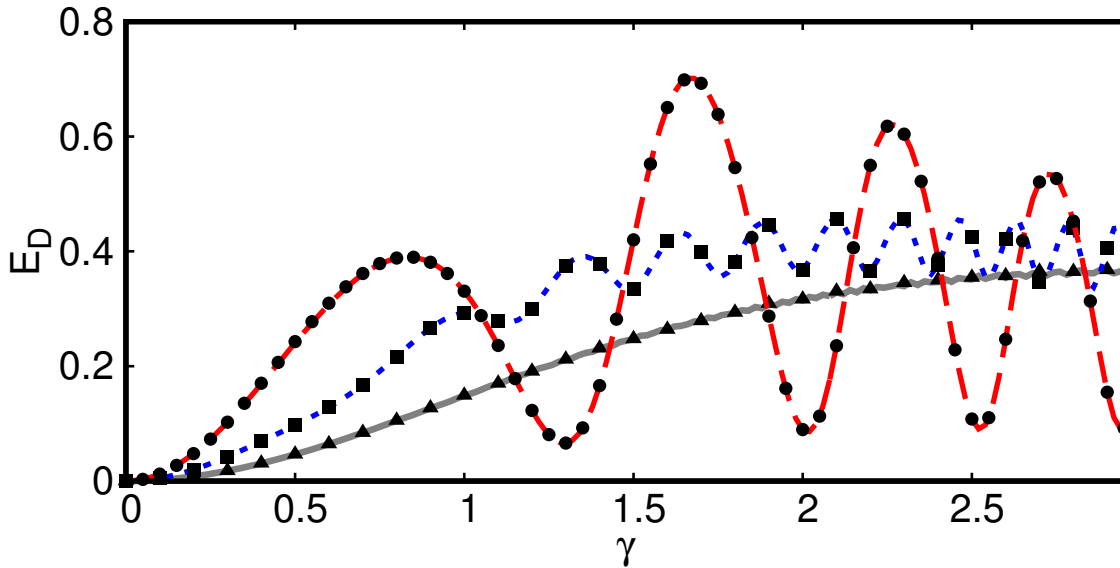


FIG. 4.9.: Dissipated energies calculated using *TEBD-LBO* (symbols) and with scattering theory and wave packet averaging (lines) for an e-p coupled impurity ($L_H = 1$). Results are plotted as a function of the electron-phonon coupling γ for the adiabatic regime $\omega_0 = 0.4$ (grey solid line and triangles), the intermediate regime $\omega_0 = 0.9$ (blue dotted line and squares), and close to the limit of the non-dissipative regime $\omega_0 = 1.5$ (red dashed line and dots). From Ref. [28].

if the electron were far away from the impurity. The good agreement of scattering theory results and *TEBD-LBO* simulations of Gaussian wave packets in all parameter regimes indicates that each term $\frac{v_n}{v_0} \left| \frac{C_n}{A} \right|^2$ of the stationary scattering state (4.16) really corresponds to the probability to find a transmitted electron with n permanently excited phonons for an incident plane wave. Consequently, the dissipated energy can be written as

$$E_D(K) = 2\omega_0 \sum_{n=1}^{n_B-1} n \frac{v_n}{v_0} \left| \frac{C_n}{A} \right|^2 = 2\omega_0 \sum_{n=1}^{n_B-1} n \frac{\sin(k_n)}{\sin(k_0)} \left| \frac{C_n}{A} \right|^2, \quad (4.34)$$

where the factor 2 originates from the condition $B_n = C_n$ for $n > 0$. To compare (4.34) with our *TEBD-LBO* data we have to follow the procedure of Sec. 4.2 and average over the Gaussian distribution as in (4.25). The perfect agreement of both approaches in Fig. 4.9 confirms that the dissipated energy can indeed be determined with the scattering theory. In the anti-adiabatic regime $E_D = 0$ holds, which can also be seen in (4.34) because $n_B = 1$ in this case and, hence, the sum has no summands.

The overall behaviour of the dissipated energy in Fig. 4.9 is very similar to that of the transmission coefficient in Fig. 4.3(a). Although the oscillation frequencies do not coincide in general, we find that the dissipated energy $E_D(K)$ is proportional to the reflection coefficient $R(K) = 1 - T(K)$ in the special case of $1 < \omega_0 < 2$. For

4. Scattering of an electronic wave packet by a one-dimensional electron-phonon-coupled structure

these phonon frequencies $n_B = 2$ and thus

$$\begin{aligned} R(K) &= \left| \frac{C_0 - A}{A} \right|^2 + \frac{\sin(k_1)}{\sin(k_0)} \left| \frac{C_1}{A} \right|^2 = \left| \frac{-\gamma C_1}{2i \sin(k_0) A} \right|^2 + \frac{\sin(k_1)}{\sin(k_0)} \left| \frac{C_1}{A} \right|^2 \\ &= \left(1 + \frac{\gamma^2}{4 \sin(k_0) \sin(k_1)} \right) \frac{\sin(k_1)}{\sin(k_0)} \left| \frac{C_1}{A} \right|^2, \end{aligned} \quad (4.35)$$

where condition (4.11) and equation (4.14) are used to write the reflection first in terms of the C_n and finally to eliminate C_0 . The dissipated energy is given by

$$E_D(K) = 2\omega_0 \frac{\sin(k_1)}{\sin(k_0)} \left| \frac{C_1}{A} \right|^2, \quad (4.36)$$

which can be inserted into (4.35) to obtain

$$E_D(K) = \frac{2\omega_0 R(K)}{1 + \frac{\gamma^2}{4 \sin(k_0) \sin(k_1)}}. \quad (4.37)$$

Such a simple relation can only be found for this special case.

As for the transmission coefficient the study of longer e-p coupled structures is not as extensive as for the impurity case, but if we restrict to the weak-coupling regime, where the local Hilbert space dimension and bond dimension are comparatively small, we can go to very large e-p coupled structures. In Fig. 4.10(a) and (b) results are shown for $L_H = 100$ in the anti-adiabatic and adiabatic regime, respectively. In the anti-adiabatic case the shape of the Gaussian wave packet is nearly conserved during the process and the phonons follow the electron as for the polaron problem, mentioned at the beginning of Ch. 3. When viewing the electron and phonon cloud as a polaron, the reduced velocity on the e-p coupled structure, compared to an electron on a tight-binding lead, can be explained with an increase of the effective mass. For the adiabatic regime we find the phonons trailing the electron with finite densities of both particle types remaining on the e-p coupled structure for $t > 100$. The greater part of the electronic density is transmitted and still resembles a Gaussian wave packet at the end of the simulation and the velocity has not changed during the scattering process. Further, we find only single phonon excitations on the e-p coupled sites with smaller probability for sites more to the right.

As for the transmission coefficient we have some results for multi-site e-p coupled structures with larger coupling strengths that indicate a behavior of the dissipated energy similar to the one shown in Fig. 4.9. Also for $\omega_0 < 1$ the dissipated energy and reflection coefficient seem to be related, but not as simple as shown above for $1 < \omega_0 < 2$, where both quantities are proportional. In addition, the transmission coefficient and dissipated energy have been studied for different initial wave numbers k_0 within the scope of a bachelor thesis [49] by Kyle Poland. The results show that both quantities can vary significantly with the wave number. New resonances become apparent in this study, but a more thorough investigation is needed to understand

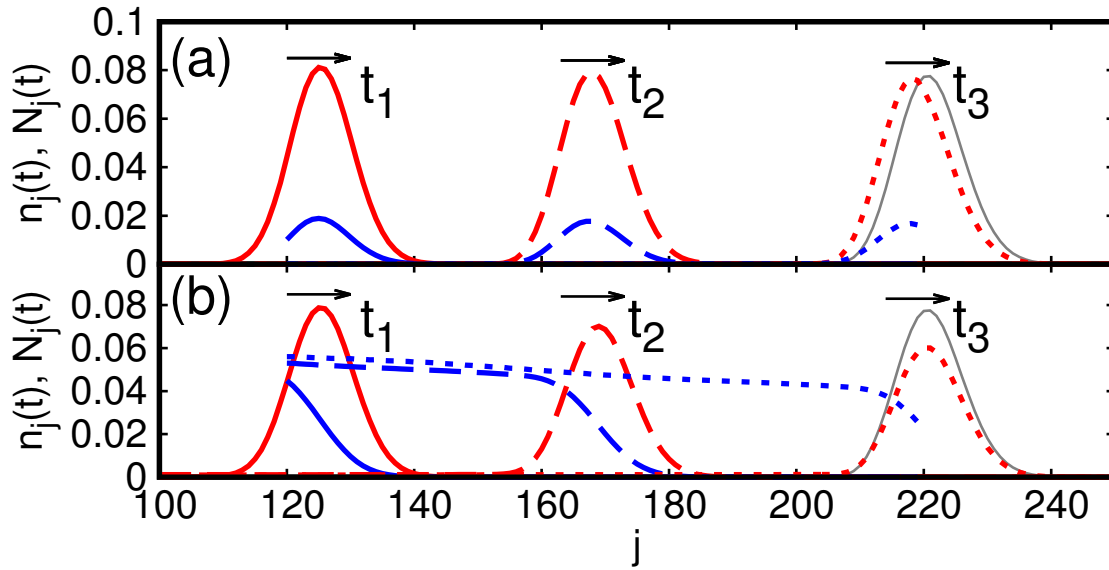


FIG. 4.10.: The electron (n_j , red) and phonon (N_j , blue) densities calculated with TEBD-LBO are compared for times $t_1 = 28$ (solid), $t_2 = 50$ (dashed) and $t_3 = 76$ (dotted). The gray line shows the electron density of a free wave packet at $t = t_3$. The e-p coupled structure has length $L_H = 100$ and begins at $j = 120$. All phonon densities are multiplied by a factor 10. (a) The anti-adiabatic weak-coupling regime is shown with $\omega_0 = 2.9$ and $\gamma = 0.25$. (b) The adiabatic weak-coupling regime is shown with $\omega_0 = 0.2$ and $\gamma = 0.1$. The electron density at $t_3 = 76$ is finite on all e-p coupled sites.

their physical meaning. These results were obtained for a single e-p coupled site and agreement with the scattering theory was found for wave numbers not too far away from $\pi/2$. Interestingly, the agreement was much better for the transmission coefficient than for the dissipated energy.

4.5. Transient self-trapping

In the previous sections we have seen that the interaction of the electronic wave packet with the phononic degrees of freedom can lead to a transient self-trapping on the e-p coupled structure. For example the quantities $T_N(t)$ and $E_{\text{ph}}(t)$ may converge at clearly distinct times for different system parameters. For long e-p coupled structures it takes naturally more time, compared to a single-site e-p coupled impurity, for the electronic wave packet to pass through. This additional time is given by $\Delta t \approx (L_H - 1)/v$. This effect is not related to a localization of the electron and, therefore, does not describe a self-trapping, but it has to be kept in mind, e.g. when comparing the lengths of the plateaus in Fig. 4.2. We have identified two different mechanisms that can cause a transient self-trapping of the electron on the e-p coupled structure.

In Fig. 4.11(a) the electronic density $n_j(t)$ on a single-site e-p coupled impurity is compared with the phonon energy $E_{\text{ph}}(t)$ in the system. We see that a great part of

4. Scattering of an electronic wave packet by a one-dimensional electron-phonon-coupled structure

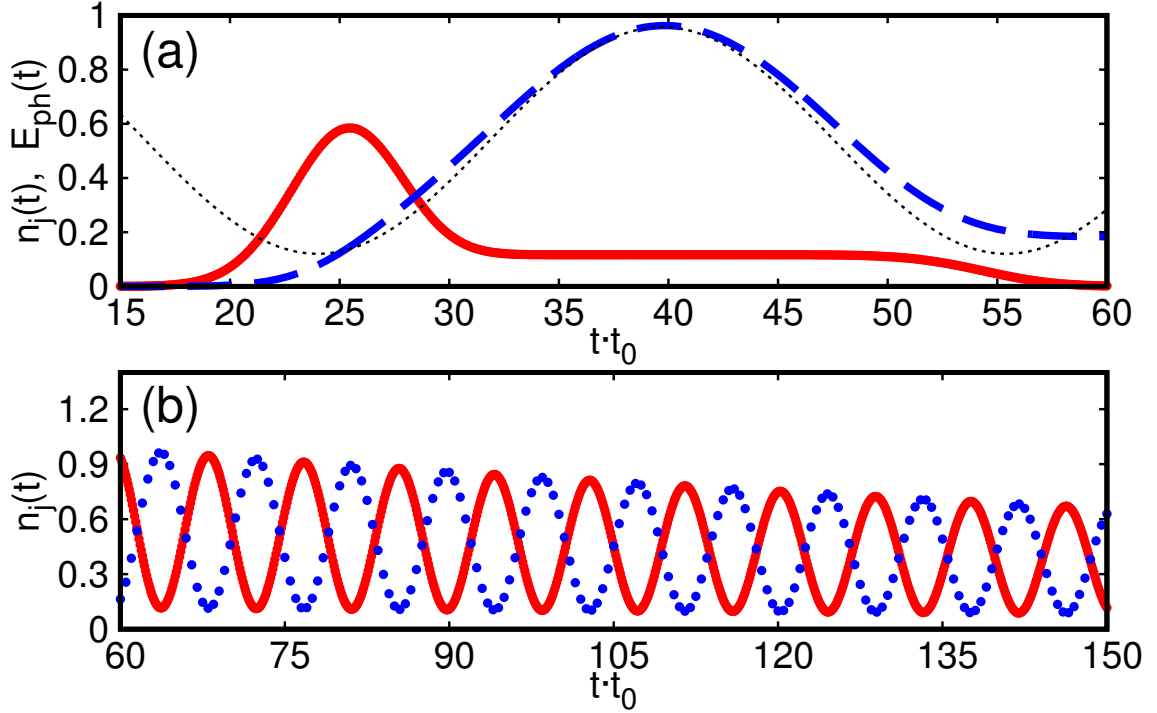


FIG. 4.11.: (a) Electronic density on the e-p coupled impurity (red solid line) and phonon energy (blue dashed line) calculated with TEBD-LBO as a function of time for $L_H = 1$, $\omega_0 = 0.20$, and $\gamma = 1.90$. The electron density is multiplied by a factor 10. The black dotted line shows Eq. (4.38) with $t_{\text{off}} = 24$, $E_{\text{off}} = 0.12$, and a constant average density $n_j(t = 40) = 0.0116$. (b) Electronic densities (multiplied by a factor 100) calculated with TEBD-LBO as a function of time on the left (red line) and right (blue dots) sites of a two-site e-p coupled structure with $\omega_0 = \gamma = 10$. From Ref. [28].

the electronic density is transmitted through, or reflected by, the impurity on a time scale $\Delta t \approx 15$, which is comparable to the time that it takes a wave packet (with width $\sigma = 5$ and velocity $v = 2$) to pass a site without interaction. However, a small fraction remains on the e-p coupled impurity for a long time. This can be understood by examining the phononic degrees of freedom. We notice that the self-trapping time scale $\Delta t \approx 30$ is similar to the period of the phonon oscillations $t = \frac{2\pi}{\omega_0} = 10\pi$. In the single-site Holstein model the time evolution of the phonon energy is given by Eq. (3.11) and we can generalize this equation to match it to the results of the TEBD-LBO simulation for a Gaussian wave packet. In Sec. 3.1 we assumed that there is always one electron on the site, but clearly this is not the case with the tight-binding leads attached to the e-p coupled site. With the electronic density $n_j(t)$ on the e-p coupled impurity we get

$$E_{\text{ph}}(t) = 2n_j(t)\varepsilon_b \left[1 - \cos(\omega_0(t - t_{\text{off}})) \right] + E_{\text{off}}, \quad (4.38)$$

where t_{off} and E_{off} are offsets for the time and energy, respectively. As can be seen in Fig. 4.11(a) we can reproduce the TEBD-LBO results qualitatively with fitted

parameters $n_j(t)$, t_{off} and E_{off} . Therefore, we can assume that the phononic degrees of freedom evolve in the same way as for the single-site Holstein model. In the adiabatic strong-coupling regime we find a negligible small occupation of the lower bare states $|n\rangle$, with $n < n_B$, for a great part of the period. During that time only the bound states have a finite weight and the electron cannot leave the impurity without violating energy conservation.

In Sec. 4.3 we have argued that a small fraction of the electronic wave packet can be trapped on an e-p coupled structure with $L_H = 2$ for a time $t > 150$. This long trapping has to be caused by another mechanism, because the one discussed above is negligible in the anti-adiabatic regime, where the period of the phononic degrees of freedom is small compared to the time scale of the passage of the electron through a small non-interacting wire. This is supported by the results of the TEBD-LBO simulations, where we see no transient self-trapping of the electron for the same system parameters, $\gamma = \omega_0 = 10$, but with $L_H = 1$.

As the resonance condition (4.17) is fulfilled, the transmission is very high, both for the impurity and the two-site e-p coupled structure. Figure 4.11(b) shows the electronic density on both sites of the e-p coupled structure after the scattering process is mainly completed, i.e. 99% of the wave packet has been transmitted or reflected. The small part that is trapped oscillates between both sites with constant frequency and damped amplitude. The constant period corresponds to a velocity $v \approx \frac{1}{4}$, which is only about one-eighth of its initial velocity. In every period $t \approx 8$ a fraction of the electronic density leaks out into the tight-binding leads, resulting in a shrinking of the total density on the e-p coupled structure by 30% on a time scale $\Delta t \approx 90$. This is a much larger time scale than any other that we have discovered in this scattering problem.

We know from Sec. 4.3 that, during the trapping period, the e-p coupled structure is mainly in a state where the occupied site is in the ground state of the single-site Holstein model, while the empty site is in the first excited bare phonon state. In the anti-adiabatic regime no phonons can be permanently excited and thus the electron cannot leak into the adjacent tight-binding lead, but is bound to the unoccupied e-p coupled site. This process can be seen as a multiple reflection at the e-p coupled structure edges, but it should not be confused with the series of independent single-site scattering events that could be applied in the adiabatic weak-coupling regime.

The fact that a part of the electronic wave packet is transmitted or reflected immediately, while the rest is transiently self-trapped and gets, possibly gradually, released into the tight-binding leads, admits different definitions for the trapping time. So far we only studied the time when the last partial wave packets leave the e-p coupled structure, but one could also ask for the minimal time delay, i.e. the additional time that the electron needs at any rate for tunneling through the e-p coupled structure. It is tempting to define this delay by the distance between the maxima in the electronic density distribution of a non-interacting wave packet and the rightmost partial wave packet after the transmission. The time for the comparison has to be chosen such that both wave packets are far away from the e-p coupled structure and the interacting electron must not have dissipated some of its energy, which would result in a

4. Scattering of an electronic wave packet by a one-dimensional electron-phonon-coupled structure

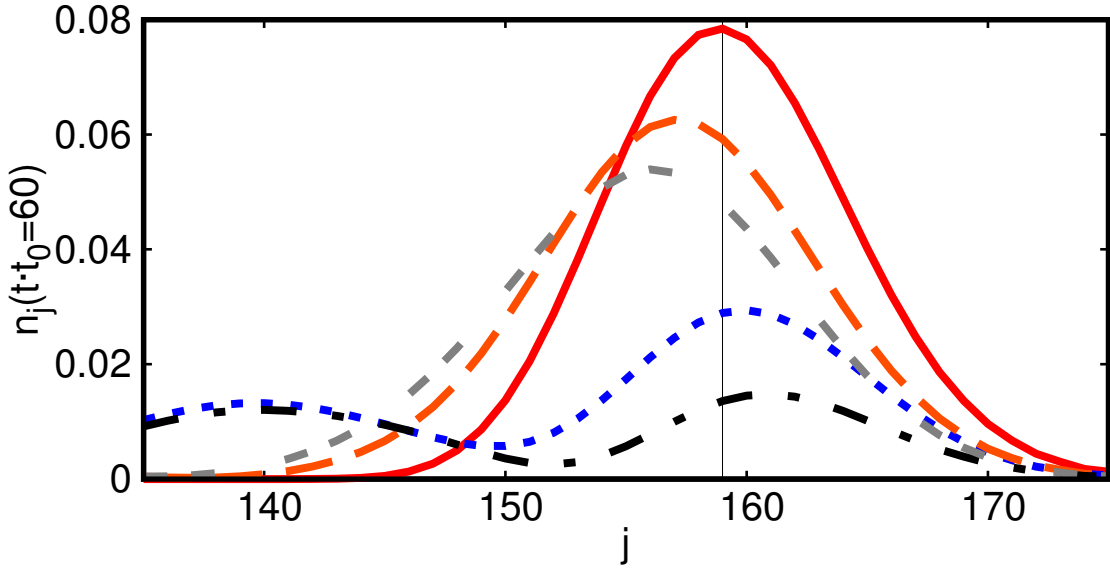


FIG. 4.12.: The rightmost part of the electronic density distributions $n_j(t)$ calculated with TEBD-LBO at $t = 60$ as a function of the lattice site index j for $L_H = 1$, $\omega_0 = 1.35$ and several electron-phonon couplings corresponding to transmission minima at $\gamma = 1.5$ (blue dotted line) and at $\gamma = 2.45$ (black dashed-dotted line) as well as to transmission maxima at $\gamma = 1.80$ (orange dashed line) and at $\gamma = 2.65$ (grey double-dashed line). The vertical black line shows the position of the maximum of the free Gaussian wave packet (red line). From Ref. [28].

lower velocity and, hence, in an increasing time delay. However, we see in Fig. 4.12 that this definition can lead to a negative time delay. This is related to the Hartman effect [50], which seemed to allow for tunneling times of particles through a potential barrier that are shorter than the time that it takes the particle to travel a distance equal to the barrier width.

It was proven for positive, compactly supported, and bounded potentials that the probability for a particle to reach a certain point before a certain time is always reduced by the presence of a potential barrier [51]. Although the scattering is caused by the interaction with dynamical degrees of freedom, Fig. 4.12 supports this result. A transmitted partial wave packet may be centered around a point more to the right compared to a free wave packet, but the reflection compensates for that and so for every lattice site behind the e-p coupled structure the probability of finding the electron on its right-hand side is reduced by the interaction.

We have observed self-trapping on time scales $\Delta t > 150$ but permanent trapping has never appeared in this setting. There are, however, two different parameter regimes, where this could happen. First, the results of Sec. 3.4 indicate that for a long e-p coupled structure in the adiabatic regime the electron might transfer all of its energy to the phonon system, which could result in an immobile trapped electron. Second, the above mentioned resonance case in the anti-adiabatic regime already provides the longest self-trapping time that we have observed so far and for larger e-p coupled

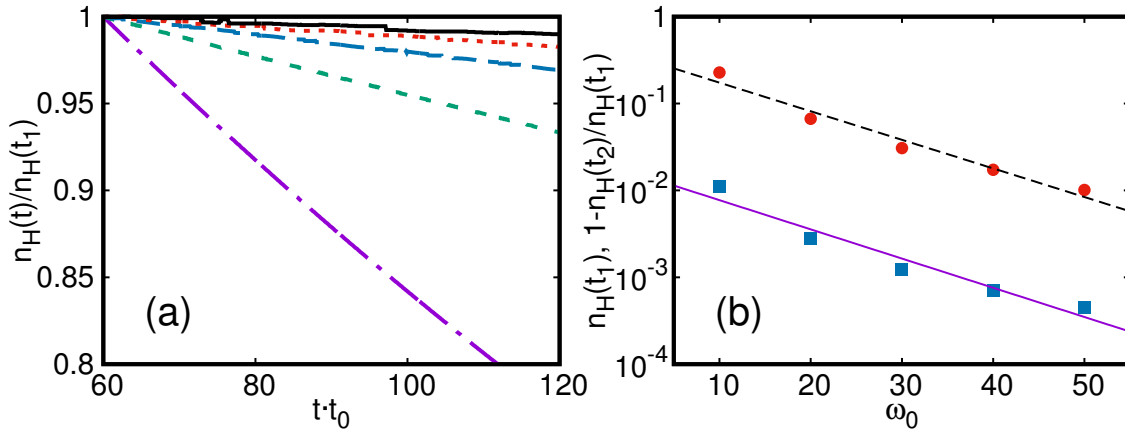


FIG. 4.13.: Analysis of the electron density on an e-p coupled structure with $L_H = 2$ at the resonance condition $\omega_0 = \gamma$. (a) Electron density normalized with the respective value at $t_1 = 60$ as a function of time for $\gamma = 10$ (purple dashed-dotted), $\gamma = 20$ (green short dashed), $\gamma = 30$ (blue long dashed), $\gamma = 40$ (red dotted) and $\gamma = 50$ (black solid). (b) The total electron density at $t_1 = 60$ (blue squares) and the relative loss in the time interval $[t_1 = 60, t_2 = 120]$ (red bullets) as a function of ω_0 , with exponential fits done with gnuplot.

structures, higher phonon frequency or stronger coupling the effect might be strong enough to bind a small fraction of the electron permanently. Unfortunately, these regimes are hard to access with our method at this time, with the exception of the small e-p coupled structure $L_H = 2$ at the resonance condition (4.17) with $m = 1$, which can be studied for larger phonon frequencies $\omega_0 > 10$. Figure 4.13(a) shows how the part of the electron density that is still trapped on the e-p coupled structure at $t = 60$ decreases with time. For larger frequencies ω_0 the electron is trapped for a longer time. To see if this leads to permanent trapping in the limit of infinite phonon frequency Fig. 4.13(b) compares the electron density left on the e-p coupled structure at $t = 60$ and the relative loss $\frac{n_H(t=60) - n_H(t=120)}{n_H(t=60)}$ on a logarithmic scale. The lines show exponential fits for both curves. For permanent trapping of a finite amount of density to appear, the red bullets would have to fall off faster than the blue squares. Instead both exponential fits have nearly the same slope, which corresponds to a permanent trapping only in the case of $n_H(t) = 0, \forall t \geq 60$. Additionally, both curves deviate from their fits in a way that indicates convergence to a finite value, meaning that a small part of the electron always gets trapped, but never permanently.

Studying this effect for the resonance condition (4.17) with $\gamma = \sqrt{m}\omega_0$, $m > 1$ or $L_H > 2$ naturally requires a higher numerical effort due to larger local Hilbert spaces and bond dimensions, but also increasing ω_0 while keeping $\frac{\gamma}{\omega_0} = 1$ yields some difficulties. The large Hamiltonian parameters necessitate a smaller time step τ in order to keep the error on the same order of magnitude, leading to a longer time for the simulation. A smaller time step also requires to adjust the chosen cutoffs in the algorithm, i.e. to keep smaller eigenvalues of the block- and single-site reduced density matrices, because the weight of newly appearing states decreases with smaller time steps. The last obstacle to mention is that the trapped density on the e-p coupled

4. Scattering of an electronic wave packet by a one-dimensional electron-phonon-coupled structure

structure is already below 10^{-3} for $\omega_0 = 50$ and the precision of the algorithm may not suffice to treat much smaller densities reliably.

5. Summary, conclusion and outlook

In this thesis we have presented a new method to efficiently simulate one-dimensional electron-phonon systems with weak to strong coupling. The time-evolving block-decimation algorithm was modified with a local basis optimization that replaces the phonon number states by the eigenstates of the single-site reduced density matrices of each lattice site, whose number can be reduced more efficiently. When the number of optimal states is much smaller than the number of bare states the theoretical scaling drops from $\mathcal{O}(D^3 d^3)$ to $\mathcal{O}(D^2 d^3)$. The method was applied to two different setups within the Holstein model, namely the relaxation of a highly excited electron by interaction with phonons and the scattering of an electronic wave packet by an EPC structure. For most calculations the algorithm was tuned for precision rather than performance. Nevertheless, a comparison with the TEBD without local basis optimization can be made.

5.1. Physical results

In Ch. 3 we have given analytical results for a Holstein chain for some limiting cases like the single-site system, short simulation times and the anti-adiabatic limit. These were used for showing the precision of the algorithm as well as for preparing the analysis of the crossover regimes. Here smooth transitions between the different regimes were found. In the anti-adiabatic limit $\omega_0 \gg t_0$ the lattice sites become nearly uncoupled and, thus, the dynamics are governed by phonon oscillations as for the single-site system, which is equivalent to a shifted harmonic oscillator and can be solved analytically. For $\omega_0 \approx t_0$ the electron transfers a great part of its excess energy to the phonons and approaches a steady state, where all three energy terms might still fluctuate, but averaged over large times no energy transfer between the electron and phonons is observed. The magnitude of the fluctuations in the steady state regime depends on the e-p coupling strength, but also on the phonon frequency as even the phonon energy approaches a nearly constant value in the adiabatic case. The relaxation time scale is in good agreement with experimental results for similar systems, where the e-p interaction is the leading mechanism for relaxation. In the steady state regime the states differ greatly from the slightly entangled initial state and, hence, the optimal modes decay much slower for such a time evolved state than for the ground state of the same system, but still the decay is roughly exponentially, which indicates the possible advantage of using our method.

In Ch. 4 long tight-binding leads were attached to both ends of a small Holstein chain and an electronic wave packet was injected into the left lead with momentum towards the EPC structure. Most of the results are for a single-site impurity, where the scattering theory yields exact results to compare with, but for example the transmission resonances in the anti-adiabatic limit were shown to be independent of the structure length L_H . The transmission coefficient as a function of the e-p coupling

5. Summary, conclusion and outlook

γ was thoroughly investigated for $L_H = 1$. Distinct resonances and blockades were found for large phonon frequency ω_0 while in the adiabatic regime a monotonically decreasing curve was observed. In the weak-coupling adiabatic limit the transmission coefficient for a multi-site EPC structure can be obtained by assuming multiple independent single-site scattering events. This leads to $T \sim 1/L_H$ for long wires, which is in accordance to classical results if we imply that the electrical conductance G of a quantum conductor is determined by its scattering properties. For example the Landauer formula [52] $G = (e^2/\pi\hbar)T$ relates the conductance and the transmission, which in our case leads to an electrical resistance $1/G \sim L_H$. Our results therefore yield a macroscopic limit coinciding with confirmed classical results.

During the passage of the electron phonons can be created transiently or permanently, depending on the adiabaticity ratio ω_0/t_0 . On large e-p coupled structures ($L_H = 100$) in the anti-adiabatic weak-coupling regime the electron is nearly perfectly transmitted, but is slowed down by the transiently excited phonons that follow it, which is in accordance with polaron theory. In the adiabatic weak-coupling regime, where dissipation is possible, the electron leaves a trail of phonons, with a small density on each site, behind. For an electron that has dissipated a part of its energy we find equal probabilities for transmission and reflection and a reduced absolute velocity due to energy conservation. The dissipated energy oscillates as a function of the e-p coupling, which is covered by the scattering theory, but a precise relation to the similar behavior of the transmission coefficient could only be found for single-site impurities with $t_0 < \omega_0 < 2t_0$, where $E_D \sim 1 - T$. This result can also be combined with the Landauer formula and would then directly relate the conductance and dissipated energy.

The electron may pass the e-p coupled structure without noticeable time delay, but it can also be trapped for large times. We have found two different mechanisms, that can cause long trapping times. The first one can be observed even for $L_H = 1$ and is solely conditioned by strong coupling. When only the higher phonon number states with $n > 2t_0/\omega_0$ have a finite weight, the electron cannot leave the e-p coupled structure until the full oscillation of the phononic degrees of freedom is completed. Hence the trapping time $\Delta t \approx \frac{2\pi}{\omega_0}$ is similar to a period of the phonon oscillations. The second mechanism can be observed for $L_H \geq 2$ at the transmission resonance in the anti-adiabatic regime. The small part of the electron, that is not transmitted immediately, gets trapped for a long time. The excess energy of the electron matches not only one eigenenergy of the single-site Holstein model with the same parameters, which leads to the resonant tunneling, but also a lower eigenenergy plus a phonon excitation (or more) on a neighboring empty site. The electron is then bound by the potential induced by this phonon. In this case the self-trapping time scale can easily exceed $\Delta t > 150$ but a permanent trapping was not observed.

5.2. TEBD-LBO performance

We have tested our method in two different setups and various parameter regimes. The required memory is no limiting factor for the use of this algorithm as it was less than 2 Gb for all presented calculations using a single core and less than 10 GB for parallelized simulations. In the Trotter-Suzuki decomposition (2.23) each exponential function gets further decomposed into the product $e^{-iH_{e(o)}\tau} = \prod_j e^{-iH_{2j(+1),2j+1(2)}\tau}$ of commuting terms, which means that all of these local updates can be computed in parallel. This is true for every TEBD implementation and is not effected by the local basis optimization. The calculations presented in this thesis were done without parallelization, except for a few of the latest results and some of them were carried out on the cluster system at the Leibniz University of Hannover.

In Ch. 4 we have argued that the length of the tight-binding leads is irrelevant for the computational time of a simulation that also includes interacting sites. A free wave packet simulation, when the coupling is turned off (or equivalently $L_H = 0$), with $L = 180$ and $t = 60$ is done in 8 min. The bond dimension and local Hilbert space dimension are kept at $D = 2$ and $d = 2$, respectively. For other systems with the same total chain length L and simulation time t the computational time could be much higher. For example for $L_H = 4$ and $\omega_0 = \gamma = 10$ the simulation took about 74 h with $D = 51$ and $d = 26$. Here the notion of D as the bond dimension of the MPS is a bit misleading, because there is only one bond of this size while for the other bonds $D_j \leq 26$ holds. In fact we find $D_j = 2, \forall j \notin \{87, \dots, 96\}$, where the EPC structure is on sites $90 \leq j \leq 93$. Such a distribution can be expected, because there is no dissipation for these parameters. If the electron is on either side of a bond not connected to the EPC structure, the other side then is an empty lattice. Next to the EPC structure the bond dimension might exceed $D = 2$, due to the occurrence of states, where the electron has left the EPC structure but is still bound to it. Another factor can be numerical artifacts arising from the small cutoff of 10^{-15} that we use for the eigenstates of the block density matrices. A restriction to larger eigenvalues has proven to be inadequate to speed up the simulations with a controlled error. Especially for the wave packet simulations, where the electron density is exponentially small on many sites, it is crucial not to project out too much too early. The maximal bond dimension can be restricted more efficiently, because this does not affect the early states. However, this does not solve the problem of the aforementioned artifacts.

To complete the discussion we analyze a simulation with $L = L_H = 4$, $\omega_0 = 1.5$, $\gamma = 5$ and $t_0 = 1.0$, which is within the strong-coupling regime. Figure 5.1 shows the relevant information to compare the performances of the TEBD on the one side and TEBD-LBO on the other side. In both cases we have $d = 166$ for the inner sites and $d = 162$ for the outer sites, so we can conclude a total Hilbert space dimension of $\dim(\mathcal{H}) = 4 \cdot 83^2 \cdot 81^2 \approx 1.8 \cdot 10^8$, which is not the largest of the presented studies, but this system has features, that make it a good candidate for a comparison. The bond dimension $D = 30$ is high enough to see the different scalings of the algorithms. Further, this 4-site system simulates long homogeneous chains with equal local Hilbert

5. Summary, conclusion and outlook

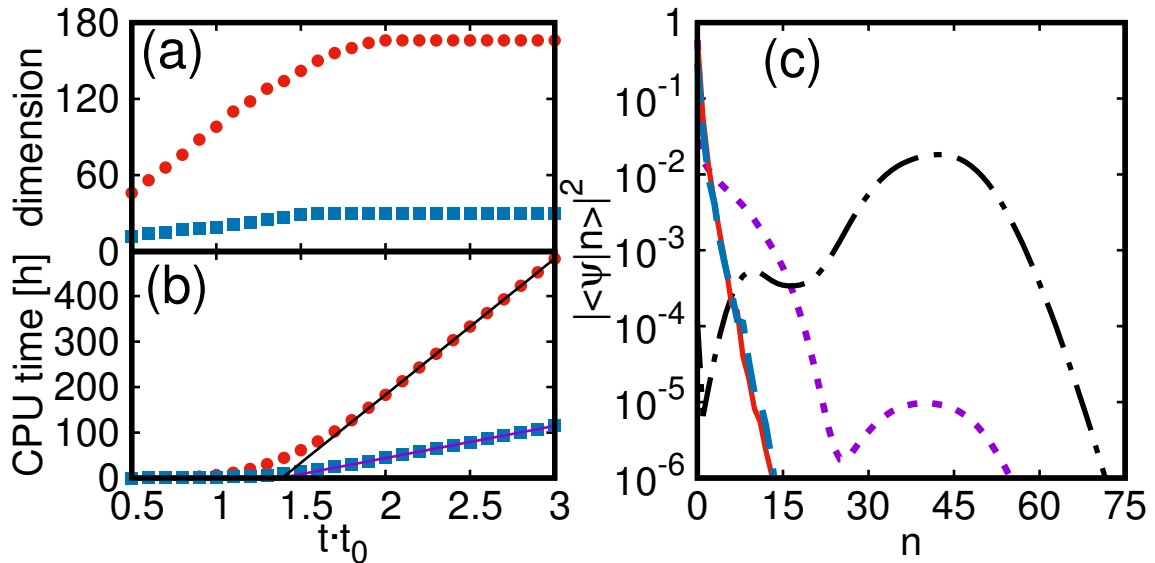


FIG. 5.1.: Comparison of TEBD and TEBD-LBO for $L = L_H = 4$, $t_0 = 1$, $\omega_0 = 1.5$ and $\gamma = 5$. (a) The local Hilbert space (red bullets) and optimal basis dimension (blue squares) in the middle of the chain are shown. (b) The CPU time of the simulations for TEBD (red bullets) and TEBD-LBO (blue squares) with linear fits for $t \geq 2$ (solid lines, black and purple, respectively). (c) The weights of the bare modes for an unoccupied (purple dotted) and occupied (black dashed-dotted) site and optimal modes for an unoccupied (red solid) and occupied (blue dashed) site. The values are taken for site $j = 2$ at time $t = 2.5$.

space dimension and bond dimension on every site and bond, respectively. This is because the simulation time is mainly given by the time for the update of the bond in the middle, which can be seen as follows. The most time consuming parts of both algorithms are at least linear in both D_{j-1} and D_{j+1} for an update of sites j and $j+1$ and, thus, any update including one of the edge sites is faster by at least a factor of 30.¹ The number of optimal modes has the same cutoff as the bond dimension, i.e. $d_0 \leq 30$. That means $d \approx 5.5 d_0$, which is enough to outperform the original TEBD in this case. A further reduction of d_0 would have been possible without significant loss of precision, but only at the price of a decreasing bond dimension at the outer bonds, which would have corrupted the fair comparison. The cutoffs are chosen as 10^{-15} for the eigenvalues of the block density matrices, 10^{-7} for the weight of the highest bare mode and 10^{-13} for the eigenvalues of the single-site reduced density matrices. Figure 5.1(c) shows that even for a time evolved state the weights of the optimal modes fall off far more rapidly than the weights of the bare modes. This verifies the efficiency of the MPS representation in the optimal basis and Fig. 5.1(b) illustrates how the computational time of the TEBD is affected by its use. A reduction of the scaling by a factor of D is not achieved, which is expected because of a higher total number of steps in a two-site update and different numerical prefactors in the most time consuming steps. To compare both computational times we look at the period

¹The bond dimension at the edges is always $D(0) = D(L) = 1$.

when all dimensions have reached their maximum. As can be seen in Fig. 5.1(a) the local dimensions do not change for $t > 2$ and all bond dimensions have also converged at this point. The computational time is then a linear function of the simulation time t and the linear fits obtained with *gnuplot* have gradients $g_1 = 299.4$ and $g_2 = 70.8$ for the TEBD and TEBD-LBO simulation, respectively. Thus, in this example, the algorithm is faster by a factor of $\frac{g_1}{g_2} \approx 4.2$ when the local basis optimization is used. To estimate the additional error introduced by the LBO we take the relative error in one of the main expectation values with the TEBD results as the reference and find $\left| \frac{E_{\text{ph}}^{\text{bare}}(t) - E_{\text{ph}}^{\text{opt}}(t)}{E_{\text{ph}}^{\text{bare}}(t)} \right| < 10^{-5}$, which shows that the deviation is acceptable. As we have argued, the 4-site system is a good approximation for homogeneous chains and the TEBD-LBO can be expected to perform similarly for larger systems.

5.3. Outlook

The advantages of the local basis optimization are most obvious in the more challenging parameter regimes. Therefore, a further optimization of the code is a central goal for the near future. The TEBD could be improved by finding proper rules for the choice of the cutoffs to minimize the computational time for a given accuracy and also by an increased utilization of the parallelization. Other planned developments are extensions of the Hamiltonian and the initial conditions. This includes the investigation of dispersive phonons, other e-p couplings like the Su-Schrieffer-Heeger or Edwards model and different electron fillings. So far we have used only a few different initial states, so it would be interesting to start our simulations also with states that are already highly entangled and exhibit phonon excitations. These states may also be obtained by other programs, that are optimized for finding ground states.

The system we are currently studying is related to the efficiency of solar cells. We investigate a heterojunction problem, where an electron is confined on a small Holstein chain, this time with an additional electronic potential and one tight-binding lead attached to it. The main question is under what conditions the electron leaks out into the lead or stays confined on the small e-p coupled structure. This is a joint project with Master student Christian Bick.

There are many possible applications that we intend to investigate in the near future and that would benefit from the use of the optimal basis. In the field of time-resolved spectroscopy the polaron-exciton problem is a natural extension of the issue of Ch. 3. Another idea is to use the extended one-dimensional Holstein-Hubbard model to study photo-generated phase transitions. Also, a further investigation of transport problems is planned. Apart from adding more electrons and dispersive phonons to further develop the study of wave packets scattered by an e-p coupled structure, one could also apply the TEBD-LBO to spin-phonon systems to study magnon dynamics.

Appendices

A. Orthonormalization of the initial state

The MPS defined in Sec.2.1 that we use as the initial state in all simulations has the canonical form. We check this for the outer vectors and the inner matrices separately. First we have

$$\sum_{k_1=1}^2 (\Gamma^{1,k_1} \lambda^1) (\Gamma^{1,k_1} \lambda^1)^\dagger =$$

$$\left(\sqrt{1-P(1)}, 0 \right) \begin{pmatrix} \sqrt{1-P(1)} \\ 0 \end{pmatrix} + \left(0, \sqrt{P(1)} \frac{\psi(1)}{|\psi(1)|} \right) \begin{pmatrix} 0 \\ \sqrt{P(1)} \frac{\psi(1)^*}{|\psi(1)|} \end{pmatrix} = 1 \quad (\text{A.1})$$

and

$$\sum_{k_1=1}^2 (\Gamma^{1,k_1})^\dagger (\Gamma^{1,k_1}) =$$

$$\begin{pmatrix} 1 \\ 0 \end{pmatrix} \begin{pmatrix} 1, 0 \end{pmatrix} + \begin{pmatrix} 0 \\ \frac{\psi(1)^*}{|\psi(1)|} \end{pmatrix} \begin{pmatrix} 0, \frac{\psi(1)}{|\psi(1)|} \end{pmatrix} = \begin{pmatrix} 1 & 0 \\ 0 & 1 \end{pmatrix} \quad (\text{A.2})$$

for the left vectors and

$$\sum_{k_L=1}^2 (\lambda^{L-1} \Gamma^{L,k_L})^\dagger (\lambda^{L-1} \Gamma^{L,k_L}) =$$

$$\left(0, \sqrt{P(L-1)} \right) \begin{pmatrix} 0 \\ \sqrt{P(L-1)} \end{pmatrix}$$

$$+ \left(\sqrt{1-P(L-1)} \frac{\psi(L)}{|\psi(L)|}, 0 \right) \begin{pmatrix} \sqrt{1-P(L-1)} \frac{\psi(L)^*}{|\psi(L)|} \\ 0 \end{pmatrix} = 1 \quad (\text{A.3})$$

and

$$\sum_{k_L=1}^2 (\Gamma^{L,k_L}) (\Gamma^{L,k_L})^\dagger =$$

$$\begin{pmatrix} 0 \\ 1 \end{pmatrix} \begin{pmatrix} 0, 1 \end{pmatrix} + \begin{pmatrix} \frac{\psi(L)^*}{|\psi(L)|} \\ 0 \end{pmatrix} \begin{pmatrix} \frac{\psi(L)}{|\psi(L)|}, 0 \end{pmatrix} = \begin{pmatrix} 1 & 0 \\ 0 & 1 \end{pmatrix} \quad (\text{A.4})$$

A. Orthonormalization of the initial state

for the right vectors. Finally, we recall the definition $P(j) = \sum_{l=1}^j |\psi(l)|^2$ to obtain

$$\begin{aligned}
& \sum_{k_j=1}^2 (\Gamma^{j,k_j} \lambda^j) (\Gamma^{j,k_j} \lambda^j)^\dagger = \\
& \begin{pmatrix} \frac{\sqrt{1-P(j)}}{\sqrt{1-P(j-1)}} & 0 \\ 0 & 1 \end{pmatrix} \begin{pmatrix} \frac{\sqrt{1-P(j)}}{\sqrt{1-P(j-1)}} & 0 \\ 0 & 1 \end{pmatrix} + \begin{pmatrix} 0 & \frac{\psi(j)}{\sqrt{1-P(j-1)}} \\ 0 & 0 \end{pmatrix} \begin{pmatrix} 0 & 0 \\ \frac{\psi(j)^*}{\sqrt{1-P(j-1)}} & 0 \end{pmatrix} = \quad (\text{A.5}) \\
& \begin{pmatrix} \frac{1-P(j)+|\psi(j)|^2}{1-P(j-1)} & 0 \\ 0 & 1 \end{pmatrix} = \begin{pmatrix} 1 & 0 \\ 0 & 1 \end{pmatrix}
\end{aligned}$$

and

$$\begin{aligned}
& \sum_{k_j=1}^2 (\lambda^{j-1} \Gamma^{j,k_j})^\dagger (\lambda^{j-1} \Gamma^{j,k_j}) = \\
& \begin{pmatrix} 1 & 0 \\ 0 & \frac{\sqrt{P(j-1)}}{\sqrt{P(j)}} \end{pmatrix} \begin{pmatrix} 1 & 0 \\ 0 & \frac{\sqrt{P(j-1)}}{\sqrt{P(j)}} \end{pmatrix} + \begin{pmatrix} 0 & 0 \\ \frac{\psi(j)^*}{\sqrt{P(j)}} & 0 \end{pmatrix} \begin{pmatrix} 0 & \frac{\psi(j)}{\sqrt{P(j)}} \\ 0 & 0 \end{pmatrix} = \quad (\text{A.6}) \\
& \begin{pmatrix} 1 & 0 \\ 0 & \frac{P(j-1)+|\psi(j)|^2}{P(j)} \end{pmatrix} = \begin{pmatrix} 1 & 0 \\ 0 & 1 \end{pmatrix}
\end{aligned}$$

for the inner matrices.

B. Diagonalization of the tight-binding Hamiltonian for open boundary conditions

We have used a transformation that diagonalizes the tight-binding Hamiltonian, which is not a Fourier-transform, because we consider open boundary conditions. In position space the Hamiltonian reads¹

$$H_{\text{kin}} = - \sum_{j=1}^{L-1} (c_j^\dagger c_{j+1} + c_{j+1}^\dagger c_j). \quad (\text{B.1})$$

We can substitute the creation and annihilation operators by $c_j^{(\dagger)} = \sqrt{\frac{2}{L+1}} \sum_{n=1}^L \sin(jk_n) d_{k_n}^{(\dagger)}$ with $k_n = \frac{n\pi}{L+1}$, $n \in \{1, 2, \dots, L\}$ to obtain the components

$$H_{nm} = 2 \sum_{j=1}^{L-1} \left[\sin(jk_n) \sin((j+1)k_m) + \sin((j+1)k_n) \sin(jk_m) \right], \quad (\text{B.2})$$

in k -space, such that $H_{\text{kin}} = -\frac{1}{L+1} \sum_{n,m=1}^L H_{nm} d_{k_n}^\dagger d_{k_m}$. To evaluate the sum (B.2) we work with the theorems for the addition and multiplication of sine and cosine instead of exponential functions. We also note that the range of the sum can be extended to $j \in \{1, \dots, L\}$ without changing the components H_{nm} because $\sin(k_n(L+1)) = \sin(n\pi) = 0$, $\forall n \in \mathbb{N}$. Furthermore we use the identity

$$\sum_{j=1}^L \cos\left(\frac{j}{L+1}n\pi\right) = \frac{-1}{2}(1 + (-1)^n) + \delta_{n0}(L+1). \quad (\text{B.3})$$

One finds

$$\begin{aligned} H_{nm} &= 2 \sum_{j=1}^L \left\{ \sin(jk_n) \left[\sin(jk_m) \cos(k_m) + \cos(jk_m) \sin(k_m) \right] \right. \\ &\quad \left. + \sin(jk_m) \left[\sin(jk_n) \cos(k_n) + \cos(jk_n) \sin(k_n) \right] \right\} \\ &= C_{nm} + S_{nm}^+ + S_{nm}^-, \end{aligned} \quad (\text{B.4})$$

¹The parameter t_0 is omitted in this section, as it does not affect the transformation.

B. Diagonalization of the tight-binding Hamiltonian for open boundary conditions

with

$$C_{nm} = \sum_{j=1}^L \left[\cos(k_m) + \cos(k_n) \right] \left(\cos(jk_{n-m}) - \cos(jk_{n+m}) \right) \quad (\text{B.5})$$

$$S_{nm}^+ = \sum_{j=1}^L \left[\sin(k_m) + \sin(k_n) \right] \sin(jk_{n+m}) \quad (\text{B.6})$$

$$S_{nm}^- = \sum_{j=1}^L \left[\sin(k_m) - \sin(k_n) \right] \sin(jk_{n-m}) \quad (\text{B.7})$$

and $k_{n\pm m} = k_n \pm k_m$. To determine C_{nm} we insert (B.3) into (B.5) and obtain

$$\begin{aligned} C_{nm} &= \left(\cos(k_m) + \cos(k_n) \right) \left[\frac{-1}{2} \left((-1)^{n-m} - (-1)^{n+m} \right) + \delta_{nm}(L+1) \right] \\ &= \left(\cos(k_m) + \cos(k_n) \right) \delta_{nm}(L+1), \end{aligned} \quad (\text{B.8})$$

where $\delta_{(n\pm m)0} = \delta_{n(\pm m)}$ and $\delta_{n(-m)} = 0$ were used. This already provides the desired transformation, so it remains to show that $S_{nm}^+ + S_{nm}^- = 0$, $\forall n, m \in \{1, \dots, L\}$. We may write

$$\begin{aligned} S_{nm}^\pm &= \pm 2 \sin\left(\frac{k_{n\pm m}}{2}\right) \cos\left(\frac{k_{n\mp m}}{2}\right) \sum_{j=1}^L \sin(jk_{n\pm m}) \\ &= \pm \frac{1}{2} \sum_{j=1}^L \left[\cos((j-1)k_n \pm jk_m) + \cos(jk_n \pm (j-1)k_m) \right. \\ &\quad \left. - \cos((j+1)k_n \pm jk_m) - \cos(jk_n \pm (j+1)k_m) \right], \end{aligned} \quad (\text{B.9})$$

so that it becomes obvious which terms in the sum cancel out. The remaining parts can be summed up to obtain

$$\begin{aligned} 2(S_{nm}^+ + S_{nm}^-) &= \cos((n-m)\pi + k_m) - \cos((n+m)\pi - k_m) \\ &\quad + \cos((n-m)\pi - k_n) - \cos((n+m)\pi - k_n), \end{aligned} \quad (\text{B.10})$$

where we can use the relation $\cos(n\pi + k) = (-1)^n \cos(k)$ to conclude

$$2(S_{nm}^+ + S_{nm}^-) = \left((-1)^{n-m} - (-1)^{n+m} \right) [\cos(k_m) + \cos(k_n)] = 0. \quad (\text{B.11})$$

Inserting (B.5) and (B.11) into (B.4) we find the Hamiltonian in k-space

$$H_{\text{kin}} = - \sum_{n,m=1}^L \left(\cos(k_n) + \cos(k_m) \right) \delta_{nm} d_{k_n}^\dagger d_{k_m} = -2 \sum_{n=1}^L \cos(k_n) d_{k_n}^\dagger d_{k_n}, \quad (\text{B.12})$$

which verifies that this transformation diagonalizes the tight-binding Hamiltonian for open boundary conditions.

Bibliography

- [1] G. Hager, A. Weisse, G. Wellein, E. Jeckelmann, and H. Fehske, The spin-Peierls chain revisited, *Journal of Magnetism and Magnetic Materials* **310**, 1380 (2007).
- [2] M. Hase, I. Terasaki, and K. Uchinokura, Observation of the spin-Peierls transition in linear Cu^{2+} (spin-1/2) chains in an inorganic compound CuGeO_3 , *Phys. Rev. Lett.* **70**, 3651 (1993).
- [3] K. S. Novoselov, A. K. Geim, S. V. Morozov, D. Jiang, M. I. Katsnelson, I. V. Grigorieva, S. V. Dubonos, and A. A. Firsov, Two-dimensional gas of massless Dirac fermions in graphene, *Nature* **438**, 197 (2005).
- [4] Y. Zhang, Y.-W. Tan, H. L. Stormer, and P. Kim, Experimental observation of the quantum Hall effect and Berry's phase in graphene, *Nature* **438**, 201 (2005).
- [5] M. Galperin, M. A. Ratner, and A. Nitzan, Molecular transport junctions: vibrational effects, *J. Phys.: Condens. Matter* **19**, 103201 (2007).
- [6] N. A. Zimbovskaya and M. R. Pederson, Electron transport through molecular junctions, *Phys. Rep.* **509**, 1 (2011).
- [7] E. A. Osorio, T. Bjørnholm, J.-M. Lehn, M. Ruben, and H. S. J. van der Zant, Single-molecule transport in three-terminal devices, *J. Phys.: Condens. Matter* **20**, 374121 (2008).
- [8] D. N. Basov, R. D. Averitt, D. van der Marel, M. Dressel, and K. Haule, Electrodynamics of correlated electron materials, *Rev. Mod. Phys.* **83**, 471 (2011).
- [9] J. Orenstein, Ultrafast spectroscopy of quantum materials, *Phys. Today* **65**, 44 (2012).
- [10] H. Matsueda, S. Sota, T. Tohyama, and S. Maekawa, Relaxation Dynamics of Photocarriers in One-Dimensional Mott Insulators Coupled to Phonons, *J. Phys. Soc. Jpn.* **81**, 013701 (2012).
- [11] K. Nasu, Itinerant type many-body theories for photo-induced structural phase transitions, *Rep. Prog. Phys.* **67**, 1607 (2004).
- [12] K. Yonemitsu and N. Maeshima, Coupling-dependent rate of energy transfer from photoexcited Mott insulators to lattice vibrations, *Phys. Rev. B* **79**, 125118 (2009).
- [13] T. Garel and H. Orland, Mean-Field Model for Protein Folding, *EPL (Europhysics Letters)* **6**, 307 (1988).

Bibliography

- [14] D. Zgid and G. K.-L. Chan, Dynamical mean-field theory from a quantum chemical perspective, *The Journal of Chemical Physics* **134**, 094115 (2011).
- [15] M. Fannes, B. Nachtergaele, and R. F. Werner, Finitely correlated states on quantum spin chains, *Comm. Math. Phys.* **144**, 443 (1992).
- [16] S. Östlund and S. Rommer, Thermodynamic Limit of Density Matrix Renormalization, *Phys. Rev. Lett.* **75**, 3537 (1995).
- [17] S. R. White, Density matrix formulation for quantum renormalization groups, *Phys. Rev. Lett.* **69**, 2863 (1992).
- [18] U. Schollwöck, The density-matrix renormalization group in the age of matrix product states, *Ann. Phys.* **326**, 96 (2011).
- [19] G. Vidal, Efficient Classical Simulation of Slightly Entangled Quantum Computations, *Phys. Rev. Lett.* **91**, 147902 (2003).
- [20] G. Vidal, Efficient Simulation of One-Dimensional Quantum Many-Body Systems, *Phys. Rev. Lett.* **93**, 040502 (2004).
- [21] F. Verstraete, V. Murg, and J. I. Cirac, Matrix product states, projected entangled pair states, and variational renormalization group methods for quantum spin systems, *Advances in Physics* **57:2**, 143 (2008).
- [22] G. Vidal, Class of Quantum Many-Body States That Can Be Efficiently Simulated, *Phys. Rev. Lett.* **101**, 110501 (2008).
- [23] F. Verstraete and J. I. Cirac, Continuous Matrix Product States for Quantum Fields, *PRL* **104**, 190405 (2010).
- [24] D. Jennings, C. Brockt, J. Haegeman, T. J. Osborne, and F. Verstraete, Continuum tensor network field states, path integral representations and spatial symmetries, *New Journal of Physics* **17**, 063039 (2015).
- [25] C. Zhang, E. Jeckelmann, and S. R. White, Density Matrix Approach to Local Hilbert Space Reduction, *Phys. Rev. Lett.* **80**, 2661 (1998).
- [26] C. Guo, A. Weichselbaum, J. von Delft, and M. Vojta, Critical and strong-coupling phases in one- and two-bath spin-boson models, *Phys. Rev. Lett.* **108**, 160401 (2012).
- [27] F. Dorfner, L. Vidmar, C. Brockt, E. Jeckelmann, and F. Heidrich-Meisner, Real-time decay of a highly excited charge carrier in the one-dimensional Holstein model, *Phys. Rev. B* **91**, 104302 (2015).
- [28] C. Brockt and E. Jeckelmann, Scattering of an electronic wave packet by a one-dimensional electron-phonon-coupled structure, *Phys. Rev. B* **95**, 064309 (2017).

-
- [29] F. F. Assaad and H. G. Evertz, *World-line and Determinantal Quantum Monte Carlo Methods for Spins, Phonons and Electrons, Computational Many-Particle Physics*, volume 739 of Lecture Notes in Physics, chapter 10, pp. 277–356 (Springer Berlin Heidelberg, 2008).
- [30] A. Daley, C. Kollath, U. Schollwöck, and G. Vidal, Time-dependent density-matrix renormalization-group using adaptive effective hilbert spaces, *J. Stat. Mech.* P04005 (2004).
- [31] S. R. White and A. E. Feiguin, Real-time evolution using the density matrix renormalization group, *Phys. Rev. Lett.* **93**, 076401 (2004).
- [32] E. Jeckelmann and S. R. White, Density-matrix renormalization-group study of the polaron problem in the holstein model, *Phys. Rev. B* **57**, 6376 (1998).
- [33] C. Brockt, F. Dorfner, L. Vidmar, F. Heidrich-Meisner, and E. Jeckelmann, Matrix-product-state method with a dynamical local basis optimization for bosonic systems out of equilibrium, *Phys. Rev. B* **92**, 241106(R) (2015).
- [34] M. B. Hastings, An area law for one-dimensional quantum systems, *J. Stat. Mech.* P08024 (2007).
- [35] J. Eisert, M. Cramer, and M. B. Plenio, Colloquium, *Rev. Mod. Phys.* **82**, 277 (2010).
- [36] H. F. Trotter, On the Product of Semi-Groups of Operators, *Proc. Am. Math. Soc.* **10**, 545 (1959).
- [37] M. Suzuki, Relationship between d-Dimensional Quantal Spin Systems and (d+1)-Dimensional Ising Systems, *Progr. Theor. Phys.* **56**, 1454 (1976).
- [38] F. A. Y. N. Schröder and A. W. Chin, Simulating open quantum dynamics with time-dependent variational matrix product states: Towards microscopic correlation of environment dynamics and reduced system evolution, *Phys. Rev. B* **93**, 075105 (2016).
- [39] L. D. Landau, Über die Bewegung der Elektronen in Kristallgitter, *Phys. Z. Sowjetunion* **3**, 644 (1933).
- [40] A. S. Alexandrov and S. N. Mott, *Polarons & Bipolarons* (World Scientific, 1995).
- [41] T. Holstein, Studies of polaron motion: Part I. The molecular-crystal model, *Ann. Phys.* **8**, 325 (1959).
- [42] U. Busch and K. A. Penson, Tight-binding electrons on open chains: Density distribution and correlations, *Phys. Rev. B* **36**, 9271 (1987).
- [43] J. Bonča, S. A. Trugman, and I. Batistić, Holstein polaron, *Phys. Rev. B* **60**, 1633 (1999).

Bibliography

- [44] F. Novelli, G. De Filippis, V. Cataudella, M. Esposito, I. Vergara, F. Cilento, E. Sindici, A. Amaricci, C. Giannetti, D. Prabhakaran, S. Wall, A. Perucchi, S. Dal Conte, G. Cerullo, M. Capone, A. Mishchenko, M. Grüninger, N. Nagaosa, F. Parmigiani, and D. Fausti, Witnessing the formation and relaxation of dressed quasi-particles in a strongly correlated electron system, *Nat. Commun.* **5**, 5112 (2014).
- [45] C. Gadermaier, A. S. Alexandrov, V. V. Kabanov, P. Kusar, T. Mertelj, X. Yao, C. Manzoni, D. Brida, G. Cerullo, and D. Mihailovic, Electron-Phonon Coupling in High-Temperature Cuprate Superconductors Determined from Electron Relaxation Rates, *Phys. Rev. Lett.* **105**, 257001 (2010).
- [46] S. Dal Conte, L. Vidmar, D. Golež, M. Mierzejewski, G. Soavi, S. Peli, F. Banfi, G. Ferrini, R. Comin, B. M. Ludbrook, L. Chauviere, N. D. Zhigadlo, H. Eisaki, M. Greven, S. Lupi, A. Damascelli, D. Brida, M. Capone, J. Bonča, G. Cerullo, and C. Giannetti, Snapshots of the retarded interaction of charge carriers with ultrafast fluctuations in cuprates, *Nat. Phys.* **11**, 421 (2015).
- [47] L.-C. Ku and S. A. Trugman, Quantum dynamics of polaron formation, *Phys. Rev. B* **75**, 014307 (2007).
- [48] H. Fehske, G. Wellein, and A. R. Bishop, Spatiotemporal evolution of polaronic states in finite quantum systems, *Phys. Rev. B* **83**, 075104 (2011).
- [49] K. Poland, *Streuung eines Elektrons durch eine Quantenschwingung* (Bachelor thesis, Leibniz Universität Hannover, 2016).
- [50] T. E. Hartman, Tunneling of a Wave Packet, *Journal of Applied Physics* **33**, 3427 (1962).
- [51] J. Kiukas, A. Ruschhaupt, and R. F. Werner, Tunneling Times with Covariant Measurements, *Foundations of Physics* **39**, 829 (2009).
- [52] Y. Nazarov and Y. M. Blanter, *Quantum transport: Introduction to Nanoscience* (Cambridge University Press, Cambridge, 2009).

Wissenschaftlicher Werdegang

Ausbildung

2007-2013	Studium der Physik, Leibniz Universität Hannover Nebenfach: Mathematik
2013-2018	Ph.D. Student, Leibniz Universität Hannover
19.01.2018	Disputation

Veröffentlichungen

Real-time decay of a highly excited charge carrier in the one-dimensional Holstein model

*F. Dorfner, L. Vidmar, C. Brockt, E. Jeckelmann,
and F. Heidrich-Meisner*
Phys. Rev. B **91**, 104302 (2015)

Matrix-product-state method with a dynamical local basis optimization for bosonic systems out of equilibrium

*C. Brockt, F. Dorfner, L. Vidmar, F. Heidrich-Meisner,
and E. Jeckelmann*
Phys. Rev. B **92**, 241106(R) (2015)

Scattering of an electronic wave packet by a one-dimensional electron-phonon-coupled structure

C. Brockt and E. Jeckelmann
Phys. Rev. B **95** 064309 (2017)

Continuum tensor network field states, path integral representations and spatial symmetries

*D. Jennings, C. Brockt, J. Haegeman, T. J. Osborne
and F. Verstraete*
New J. Phys. **17**, 063039 (2015)